Real-time in vivo luminescence dosimetry in radiotherapy and mammography using Al2O3:C

Aznar, Marianne

Publication date:
2005

Document Version
Publisher's PDF, also known as Version of record

RISØ

Risø-PhD-12(EN)

Real-time *in vivo* luminescence dosimetry in radiotherapy and mammography using Al_2O_3:C

Marianne C Aznar

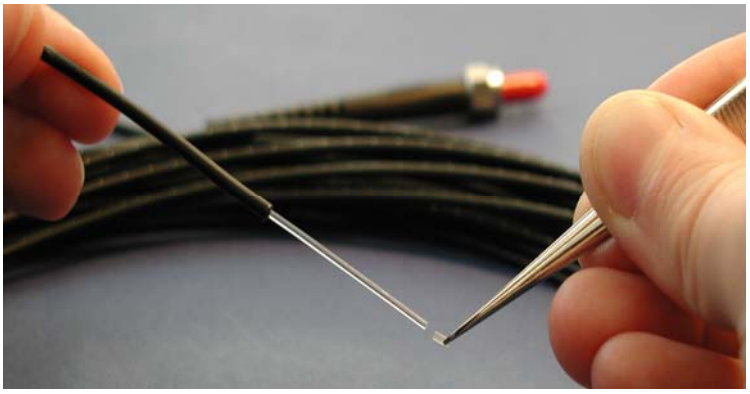

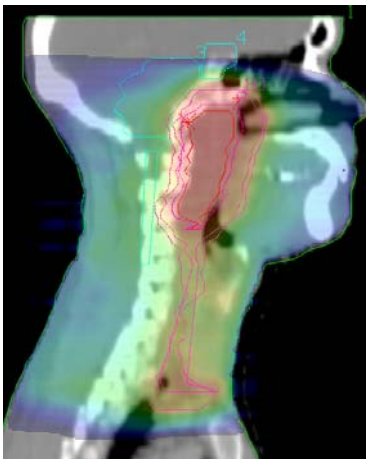

Risø National Laboratory
Roskilde
Denmark
July 2005

Risø-PhD Thesis

Author: Marianne C Aznar
Title: Real-time in vivo luminescence dosimetry in radiotherapy and mammography using Al_2O_3:C
Department: Radiation Research Department

This thesis is submitted in partial fulfillment of the requirements for the Ph.D. degree at the University of Copenhagen, Denmark

Abstract (max. 2000 char.):
New treatment and clinical imaging techniques have created a need for accurate and practical *in vivo* dosimeters in radiation medicine. This work describes the development of a new optical-fiber radiation dosimeter system, based on radioluminescence (RL) and optically stimulated luminescence (OSL) from carbon-doped aluminium oxide (Al_2O_3:C), for applications in radiotherapy and mammography. This system offers several features, such as a small detector, high sensitivity, real-time read-out, and the ability to measure both dose rate and absorbed dose. Measurement protocols and algorithms for the correction of responses were developed to enable a reliable absorbed dose assessment from the RL and OSL signals.
At radiotherapy energies, the variation of the signal with beam parameters was smaller than 1% (1 SD). Treatment-like experiments in phantoms, and *in vivo* measurements during complex patient treatments (such as intensity-modulated radiation therapy) indicate that the RL/OSL dosimetry system can reliably measure the absorbed dose within 2%. The real-time RL signal also enables an individual dose assessment from each field.
The RL/OSL dosimetry system was also used during mammography examinations. In such conditions, the reproducibility of the measurements showed to be around 3%. *In vivo* measurements on three patients showed that the presence of the RL/OSL probes did not degrade the diagnostic quality of the radiograph and that the system could be used to measure exit doses (i.e., absorbed doses on the inferior surface of the breast). A Monte carlo study proved that the energy dependence of the RL/OSL system at these low energies could be reduced by optimizing the design of the probes.
It is concluded that the new RL/OSL dosimetry system shows considerable potential for applications in both radiotherapy and mammography.

Risø-PhD-12(EN)
June 2005

ISSN 0106-2840
ISBN 87-550-3450-0

Contract no.:

Group's own reg. no.:

Sponsorship:
Risø National Laboratory, Denmark and Landauer Inc., Chicago, USA

Cover :
Top: optical fiber and aluminium oxide crystal
Bottom left: treatment planning in radiotherapy
Bottom right: aspect on the RL/OSL fibers on a mammogram.

Pages: 115
Tables: 13
References: 114

Risø National Laboratory
Information Service Department
P.O.Box 49
DK-4000 Roskilde
Denmark
Telephone +45 46774004
bibl@risoe.dk
Fax +45 46774013
www.risoe.dk

Real-time *in vivo* luminescence dosimetry in radiotherapy and mammography using Al_2O_3:C

Marianne Camille Aznar

Risø National Laboratory, Roskilde, Denmark
June 2005

Acknowledgements

First of among the many people who contributed to this exciting research project, I would like to express my deepest gratitude to Lars Bøtter-Jensen, my external supervisor at Risø National Laboratory. Lars offered unfailing support throughout the good and bad times, put me back on track when I was about to lose my focus, and was as concerned with my personal well-being as with the results of my research.

I am deeply grateful to Stig Steenstrup, my supervisor at the University of Copenhagen for his scientific insight and suggestions as well as for handling all administrative and course-work related issues.

The work presented in this thesis is the result of close interactions among members of the "Risø fiber group": I am deeply indebted to Claus Erik Andersen, whose dedication and input have been crucial to this work as well as my personal development as a scientist. Carl Johan Marckmann is responsible for improving the design of the RL/OSL probes and clearing up the mysteries of the "stem effect": this research project would have been missing a dimension without his contribution.

I would like to thank many people at Malmö University Hospital for their support. The help and guidance of Joakim Medin has been invaluable during this whole project, but especially during the Monte Carlo study. The experimental part of this project owes much to Sören Mattsson, Bengt Hemdal, Sven Å J Bäck, and Bob Smulders who all sacrificed many evenings.

I am deeply grateful to Flemming Kjær-Kristoffersen, Flemming Rosendal and Pia Haraldsson at Copenhagen University Hospital (Rigshospitalet) for their help during the radiation therapy experiments and *in vivo* measurements.

From Risø National Laboratory, I would like to thank Andrew Murray and Jens Morgenthaler Edmund for thought provoking discussions, as well Finn E Willumsen, Jørgen H Jakobsen, Henrik E Christiansen and Finn Jørgensen for their much appreciated technical help.

Many thanks to Kjeld J Oslen from Herlev University Hospital (Amtssygehuset i Herlev) for his careful reading this manuscript and very valuable suggestions.

Without the support of many special people in my life, I would have never managed to finish. I would like to express my deepest gratitude to Kristina J Thomsen, my dearest friend and office mate for her constant support and willingness to listen to my rants. Many thanks to my husband Wian de Jongh for his unfailing conviction that I would make it, and to our daughter Alice for giving me perspective.

Contents

Acknowledgements **i**

List of Figures **vii**

List of Tables **xiii**

1 *In vivo* dosimetry in radiation medicine **1**
1.1 Radiotherapy . . . 2
1.1.1 Conventional external therapy . . . 2
1.1.2 IMRT . . . 3
1.1.3 Required accuracy . . . 4
1.2 Diagnostic radiology and mammography . . . 5
1.2.1 International recommendations and regulations . . . 5
1.2.2 Dosimetry in mammography . . . 7
1.3 Current *in vivo* dosimetry techniques . . . 7
1.3.1 The standard: ionization chambers . . . 7
1.3.2 Thermoluminescence dosimeters . . . 8
1.3.3 Semiconductor diodes . . . 8
1.3.4 2D techniques . . . 9
1.4 Novel dosimetry techniques . . . 10
1.4.1 MOSFETs . . . 10
1.4.2 Diamond detectors . . . 10
1.4.3 Optical fiber dosimetry . . . 11
1.5 Practical issues: time and money . . . 12
1.6 This thesis . . . 13

2 Luminescence dosimetry with Al_2O_3:C **17**
2.1 Principles of luminescence . . . 17
2.1.1 Band gap theory . . . 17
2.1.2 Uses of Al_2O_3:C in non-medical dosimetry . . . 19
2.2 OSL from Al_2O_3:C . . . 19

2.3 RL from Al_2O_3:C . . . 22
2.4 Dosimetric considerations . . . 22
2.4.1 Interaction of radiation with matter . . . 22
2.4.2 Tissue equivalence . . . 26
2.4.3 Cavity theory: size matters . . . 28
2.5 Summary . . . 31

3 Instrumentation and methods 33
3.1 Overview of the system . . . 33
3.2 Optics and electronics . . . 34
3.3 The optical fibers . . . 36
3.3.1 PMMA fibers . . . 36
3.3.2 Signal coming from the light guide . . . 38
3.4 Crystals . . . 39
3.5 Analysis of the OSL signal . . . 40
3.6 Analysis of the RL signal . . . 41
3.6.1 Dose assessment from the RL signal . . . 42
3.6.2 Correcting for sensitization effects . . . 44
3.6.3 Getting rid of the stem-effect: time gating . . . 46
3.7 Summary . . . 47

4 Basic dosimetry parameters for radiotherapy 51
4.1 Additional equipment and set-up . . . 51
4.2 Reproducibility . . . 52
4.3 Linearity and dose rate response . . . 54
4.4 Energy dependence . . . 57
4.5 Angular dependence . . . 59
4.6 Crystal temperature . . . 60
4.7 Depth dose distributions . . . 60
4.8 Spatial resolution . . . 61
4.9 Sources of variability . . . 62
4.9.1 Mechanical sources . . . 63
4.9.2 Effects due to the crystal . . . 66
4.10 Conclusion . . . 67

5 Clinical applications in radiotherapy 69
5.1 Conventional radiotherapy simulation in an anthropomorphic phantom . . . 69
5.2 IMRT simulation in a solid water phantom . . . 72
5.2.1 RL results: stem effect and sensitivity changes . . . 73
5.2.2 OSL results . . . 73

5.3 *In vivo* IMRT 74
5.3.1 IMRT with TLDs at Rigshospitalet 74
5.3.2 Protocol for RL/OSL measurements in patients 75
5.3.3 Potential sources of uncertainty 76
5.3.4 Results from RL/OSL *in vivo* measurements 76
5.4 IMRT with improved RL analysis 77
5.5 Conclusion 79

6 Clinical applications in mammography 83
6.1 Dosimetry in mammography 83
6.1.1 Diagnostic equipment used in these experiments 83
6.1.2 Quantities measured 84
6.2 Basic dosimetry characteristics 85
6.2.1 Protocol 85
6.2.2 Reproducibility and linearity 87
6.2.3 Energy dependence 88
6.3 Quantities of clinical interest 90
6.3.1 Backscatter factors 90
6.3.2 Influence of phantom thickness 91
6.4 *In vivo* measurements 91
6.4.1 Conclusion from the *in vivo* experiments 93
6.5 Probe design and energy dependence: a Monte Carlo study . . 96
6.5.1 Spectral data 98
6.5.2 Results 99
6.5.3 Discussion 100
6.6 Conclusion 102

7 Conclusion 103

References 105

List of Figures

1.1 Characteristics of external radiation therapy and differences between conventional treatments and IMRT. In conventional treatments, few beams are used and a high dose is delivered to the tumor and to some healthy tissue. In IMRT, many small modulated beams are used, resulting in "tailored" dose delivery to the target volume. As a result, healthy tissue is spared. 3

1.2 Main characteristics of a mammography screening. The goal is to obtain a high quality (high contrast) image at an acceptable dose. 6

1.3 Several commonly used point dosimeters, their size and sensitive volume (SV) or sensitive area (SA). 13

2.1 Band gap theory: prompt luminescence or "RL" (a) and stimulated luminescence e.g. "OSL" (b). RC: recombination center. *: excited state of the recombination center. (1) OSL trap, (2) shallow trap, (3) deep trap. 20

2.2 Components of the RL signal for exposure at a constant dose rate. Top: the whole RL signal from Al_2O_3:C for an absorbed dose of 1 Gy, (a) transient, (b) slope due to sensitization, (c) afterglow. Bottom (e): after the end of the irradiation, some afterglow is observed due to the presence of shallow traps. . . 23

2.3 Characteristics of the major interaction processes: photoelectric effect, Compton scattering and pair production. 25

2.4 Predominance of interaction processes: photoelectric effect (κ), Compton scattering (σ), coherent scattering (σ_{coh}), pair production (π_n in a nuclear field, π_e in an electron field). Source: NIST (XCOM). 27

2.5 (a): Ratio of mass energy absorption coefficients of many dosimetric materials with respect to water, (b): detail at high energies. Source: NIST (XCOM). 28

2.6 Ratio of total stopping power to water for several dosimetric materials. Source: NIST (ESTAR). 28
2.7 Parameter "d" from Burlin cavity theory versus electron energy for several dosimeter sizes. Circles: 0.5 mm ø x 2 mm ℓ. Triangles: 1 mm ø x 2 mm ℓ. + : 0.3 mm ø x 1 mm ℓ. X : 0.1 mm ø x 0.5 mm ℓ. The solid line represents the response of a plastic scintillator (1 mm ø x 4 mm ℓ). 30

3.1 Schematic of the RL/OSL dosimetry system. 34
3.2 Photograph of the RL/OSL dosimetry system, showing a configuration where two measurement probes can be used simultaneously. 35
3.3 RL and OSL signals from Al_2O_3:C for an absorbed dose of 1 Gy. 36
3.4 User interface of the RL/OSL dosimetry system. 37
3.5 Photograph of the large RL/OSL fiber. Top: fiber 01, with shrinkflex wrapping. Bottom: fiber 43 using NOA 61 adhesive and an Araldite coating. 38
3.6 Signal from three different Al_2O_3:C fibers for an absorbed dose of approximately 2 Gy, delivered at 3 Gy/s: RL (top row) and OSL (bottom row). Fiber 43 exhibits the highest sensitivity, the most RL sensitization and the slowest OSL decay. 40
3.7 Reproducibility of the OSL response depending on the integration time. The OSL signal is integrated for durations ranging from 0s (using only the "initial" OSL reading) to 700 s, and the results are plotted as OSL response per dose unit (absorbed doses ranged from 0.7 to 4 Gy). The standard deviation of the results is given for each integration time. Integrating for 100 s gives the flattest response of the OSL signal per dose unit. . 41
3.8 Linearity of the OSL response depending on the integration time. The OSL signal is integrated for durations ranging from 0s (using only the "initial" OSL reading) to 700 s. The standard deviation of the residuals from the linear fit divided by the maximum response is given for each integration time. Integrating for 100 s or more results in the most linear OSL response versus absorbed dose. 42
3.9 Sensitivity changes of the RL signal in a 6 MV beam (absorbed dose = 1 Gy): the initial RL signal increases linearly with the dose rate (a) and the rate of sensitivity changes ("slope") increases with the square of the dose rate (b). 43

3.10 RL curves from exposure of the same Al_2O_3:C crystal to two sources: (a) 6 MV linac (dose rate =12 mGy/s), (b) Cobalt-60 source (dose rate = 2 mGy/s). The absorbed dose was 1 Gy in both cases. The difference in total RL counts is smaller than 0.2%. 44
3.11 RL at the start up of a Varian clinac 2100: the instability of the dose rate delivered by the linac at the beginning of the exposure is clearly demonstrated and prevents the use of the "RL initial" method. 45
3.12 An example of the RL sensitization correction algorithm for dose of 2 Gy, delivered at 3 Gy/min with 6 MV photons. (a) shows the raw RL signal during the irradiation and the fitted calibration curve. (b) and (c) show the estimated dose rate (from the corrected RL signal) and the accumulated dose, respectively. 46
3.13 Test of the sensitization correction algorithm. A depth dose distribution was acquired using only the RL signal, without resetting the crystal with laser light between measurements. RL data agree closely with reference data (obtained with diodes) and demonstrate the validity of the correction algorithm. . . . 47
3.14 Temporal gating for acquisition of the RL signal. 48

4.1 Set up for radiotherapy experiments. Parameters illustrated are the source-to-surface distance (SSD), field size (FS), and depth (d). 53
4.2 Reproducibility of the RL/OSL system in laboratory conditions: OSL (a) and RL (b) responses for 66 consecutive measurements. 54
4.3 Reproducibility of signals in a 18 MV clinical beam. Results from 8 consecutive measurements are presented, showing the RL signal, the first 4 seconds of the OSL signal, as well as the background signal obtained after 400 s of bleaching. 55
4.4 OSL signal versus absorbed dose: results are presented in log scale (a) and linear scale (b). 56
4.5 OSL signal versus dose rate in ^{60}Co and ^{137}Cs gamma sources 56
4.6 Dose rate response of the RL/OSL system in a 6 MV beam: (a) normalized OSL results; (b) Initial RL signal versus dose rate (here, pulse rate). 57
4.7 Energy dependence of the RL/OSL dosimeter in 6 MV (circles) and 18 MV (triangles) photon beams. (a) OSL results, (b) RL results. 58

4.8 Energy dependence between ^{60}Co (circles) and 6 MV (triangles). OSL results are presented and are normalized by ionization chamber readings. The solid and dotted lines represent the average values of OSL response for ^{60}Co and 6 MV, respectively. 58
4.9 RL/OSL responses versus the angle of incidence of the beam. Black circles: OSL, Grey crosses: RL. The fiber was positioned along a vertical, downward axis 59
4.10 OSL response of the probe at different temperatures: the variation in response can be minimized if a long integration time is used. 61
4.11 OSL response of the probe at different temperatures. The height of the initial signal varies with temperature, but the effect fades after a couple of seconds, suggesting a faster depletion of shallow traps at higher temperatures. 62
4.12 RL response of the probe at different temperatures. (a) total RL signal: no clear trend can be observed with increase in temperature; (b) detail of the afterglow: the decay rate increases with high temperatures. 62
4.13 Depth dose distributions for 6 and 18 MV photons. Solid line: diodes, hollow symbols: OSL, full symbols: RL. 63
4.14 Depth dose distributions for 6 and 22 MeV electrons. Solid line: diodes, open symbols: OSL, filled symbols: RL. The inserts on top of the graphs show the discrepancy between diode and luminescence data. 63
4.15 Lateral profile for 6 MV photons. Solid line: diodes, hollow symbols: OSL, full symbols: RL. 65
4.16 Position of fibers in a solid water phantom in presence of air cavities. 67

5.1 Position of the fiber in the anthropomorphic phantom during CT-scanning. 70
5.2 Treatments plans for the anthropomorphic phantom: the first plan consists of two opposed fields in the anterior-posterior direction; the second plan includes, in addition, a lateral field and wedges for dose homogeneity within the target volume. . . 70
5.3 RL signal for the IMRT treatment in a solid water phantom: (a) linear scale, (b) semi-log scale. 72

5.4 The RL signal can be used as a "fingerprint" of the fibers' respective positions. Here, the signals from fiber 48 and fiber 49 overlap, i.e. the two fibers were in the same measurement location. 74
5.5 Field 1 dose delivery versus time with probe A (fiber 43). Note the high reproducibility from treatment to treatment (IMRT-G1, G2, and G3). 79
5.6 Position of fibers 43 (probe A) and 37 (probe B) in the solid water phantom. 79
5.7 Field by field dose delivery versus time for probes A and B. The offset between the signals confirms that the fibers are a few mm apart. 80

6.1 Illustration of a mammography measurement set up, showing the principal components and the position of the fibers. 84
6.2 Typical RL and OSL signals in mammography for 40mAs (a) and 80 mAs (b). 86
6.3 Stem effect in mammography conditions. Black symbols represent the RL signal, and grey symbols show the signal coming from the light guide. 86
6.4 RL sensitivity changes. Even for a long (250 mAs) exposure, the increase in RL signal is not noticeable. 87
6.5 Reproducibility of the RL and OSL signals for an air kerma of 4.5 mGy for 13 measurements. (a): integrated OSL signal, (b) first 7 seconds of the OSL signal , (c) integrated RL signal and (d) visualization of the total RL signal. 88
6.6 Linearity of dose-response for several exposures at 29 kV (R-squared>0.999). Data are normalized to their value at a 250 mAs exposure, corresponding to an air kerma of 30 mGy. RL signal (crosses), OSL signal (circles). 89
6.7 Energy dependence of the RL/OSL signals. The data are divided by the ionization chamber readings, and normalized to read unity at 29 kV. RL: crosses, OSL: circles. 89
6.8 Measurements with one probe (fiber 49) at the entrance surface, the other (fiber 48) at the exit surface of a PMMA phantom. The ratios of $RL_{exit}/RL_{entrance}$ are presented for 23 kV (diamonds), 29 kV (triangles) and 35 kV (circles). 91
6.9 Impact of the RL/OSL fibers on a mammogram. 93
6.10 RL entrance and exit signals for one patient measurement. . . 96
6.11 Geometry of an RL/OSL probe used in EGSnrc simulations. . 97

6.12 Spectra used in EGSnrc. The energy fluence normalized to the area under the distribution, Φe, is plotted versus photon energy. Solid line with symbols: IPEM data, solid line: measured data, dotted line: modified measured data. 99

List of Tables

1.1 Summary of the characteristics of different in vivo point dosimeters: 0=no concern, X= mild concern, XX=major concern (based on (Van Dam and Marinello, 1994) and adapted for novel dosimeters) 16

3.1 Fibers and crystals used in this work 37

4.1 Sources of variability in dosimetric measurements with the RL/OSL optical fiber system 64

5.1 Results from the experiment using an anthropomorphic phantom. 71

5.2 RL/OSL results from the IMRT treatment in a solid water phantom with fibers 48 and 49. 73

5.3 Results of three *in vivo* measurements: OSL absorbed dose estimates versus predicted doses from the treatment planning system. Confidence intervals (95%) are given for the OSL estimates. 77

5.4 Dose estimates in mGy for three IMRT treatments in a solid water phantom: IMRT-G1, IMRT-G2, and IMRT-G3 and the corresponding reference values from the treatment planning system (TPS). To indicate the influence of set-up errors, we both report the TPS values for our best estimates of two probe locations (A and B) as well as the minimum and maximum of TPS values observed ±2 mm away (along the three principal axes). For example, the TPS value for probe A, field 1 is 86 mGy, but values from 80 to 90 were observed in the ±2 mm cube. 82

6.1 Reproducibility of the RL/OSL system (expressed as 1SD of 13 measurements at 29 kV for an air kerma of 4.5 mGy) . . . 88

6.2 Measurements of backscatter factors (BSF) from a PMMA phantom. Three exposures were performed in each set-up. . . 90
6.3 Patient image data and entrance surface air kerma (ESAK) and average glandular dose (AGD) values determined from the ionization chamber measurements. CC: cranio-caudal view; MLO: mediolateral oblique view. 94
6.4 Entrance surface dose (ESD) determined for each breast image from the ionization chamber measurements and RL/OSL *in vivo* data. RL and OSL counts have been corrected for sensitivity differences between fiber 48 and fiber 49. 95
6.5 Ratios of Monte Carlo calculated values of absorbed dose crystal and air kerma for three various diameters (ø). Two beam qualities and three different spectral distributions were included in the comparison. The thickness of light-protective material around the crystal was set to 0 mm. The standard uncertainty of calculated ratios was 0.3% for the largest crystal, 0.5% for the middle-sized crystal and 0.8% for the smallest. *meas* refers to the measured spectra and *modif* to the modified measured spectra. *Incr* represents the percentage increase in Dc/Dair from exposure in a 25kV beam to exposure in a 31 kV beam. 100
6.6 Ratios of Monte Carlo calculated values of absorbed dose to the crystal and air kerma free in air for three various thicknesses of the light protective material surrounding the crystal. Two beam qualities and three different spectral distributions were included in the comparison. The diameter of the crystal was set to 0.48 mm. The standard uncertainty of calculated ratios was 0.5%. *meas* refers to the measured spectra and *modif* to the modified measured spectra. *Incr* represents the percentage increase in Dc/Dair from exposure in a 25kV beam to exposure in a 31 kV beam. 101

1 *In vivo* DOSIMETRY IN RADIATION MEDICINE

In vivo dosimetry is the final stage in a long series of quality assurance (QA) procedures in radiation medicine. As the term *in vivo* indicates, these measurements are generally performed during patient treatment or diagnostic examination, and the measuring instrument is either positioned inside the patient, on the patient's skin or as close as possible. The other quality assurance procedures are performed in phantoms (i.e., in the absence of the patient) in order to check the behavior of the medical apparatus (linear accelerator, or diagnostic imaging unit) or the validity of a computer-designed treatment plan. Today, the use of *in vivo* dosimetry is increasing following recommendation by many national and international organizations. New diagnostic and treatment techniques like intensity modulated radiation therapy (IMRT) introduce new challenges and requirements, such as the need to provide real-time dosimetry devices with high spatial resolution, sensitivity and accuracy. Such *in vivo* dosimeters can identify deviations in the delivery of standard or complex treatments, evaluate the dose to radio-sensitive organs or estimate the absorbed dose delivered in situations where computer calculations are not reliable (for example at interfaces between tissue and air (lungs, skin), tissue and bone, etc). Several *in vivo* dosimetry systems are available, but have pitfalls in terms of accuracy or require considerable investments in time and money. These factors have so far greatly limited the widespread application of *in vivo* dosimetry. In order to fully understand the role and implications of *in vivo* dosimetry, it is necessary to know the goals of the medical procedures involving radiation, as well as the risk associated with them. In this chapter, the philosophy of radiotherapy and imaging is briefly outlined, and some of the most popular *in vivo* dosimetry devices are reviewed. In view of the topic of this thesis work, the discussion will be limited to two subfields: external radiation therapy and mammography. These two disciplines differ in terms of medical intent and the magnitude of the ra-

diation doses involved. Both situations are however carefully regulated and monitored. Whenever necessary, the relevant physical concepts are described but a full description of the science of dosimetry is beyond the scope of this work.

1.1 Radiotherapy

Radiotherapy (or "radiation therapy") describes the use of ionizing radiation such as photons and electrons, and to a lesser extent, protons and neutrons to treat a critical condition such as a cancerous tumor. The term "external radiation therapy" is also used to differentiate treatments delivered by linear accelerators or "linacs" from brachytherapy treatments (where the radioactive source is positioned near the tumor, often inside the patient's body). Most radiotherapy treatments involve high-energy x-rays (4 to 25 MV), but high energy electron beams (6-22 MeV) are also used, either alone or in conjunction with photon beams. The patient is generally affected by a life-threatening disease, and will be requiring a long (5-7 weeks) and difficult (side-effects) treatment procedure. Conventional external therapy and intensity modulated radiation therapy (IMRT) are two kinds of treatments differing in their technological complexity. They are illustrated in figure 1.1 and are detailed below.

1.1.1 Conventional external therapy

For a patient treated with external radiation therapy, the process is the following: the extent of the volume to be treated (usually referred to as "target volume") is delineated on computerized tomography (CT) images of the patient before the beginning of the treatment. These CT data (containing the patient specific 3D anatomy information) are then transferred to a computerized treatment planning system (TPS), where the physical details of the radiation beams are going to be defined (such as the angles and the energy). The TPS will then calculate a 3D dose distribution, according to an algorithmic modeling of radiation interactions with matter. Several beam combinations can be achieved by trial and error before the optimal dose distribution is achieved. In most conventional therapy cases, no additional quality assurance (QA) check is performed. The treatment itself is typically divided into 25 fractions of 2 Gy, in order to deliver a total absorbed dose of 50 Gy to the target volume. *In vivo* dosimetry may or may not be performed in conventional treatments, depending on the institution's practices.

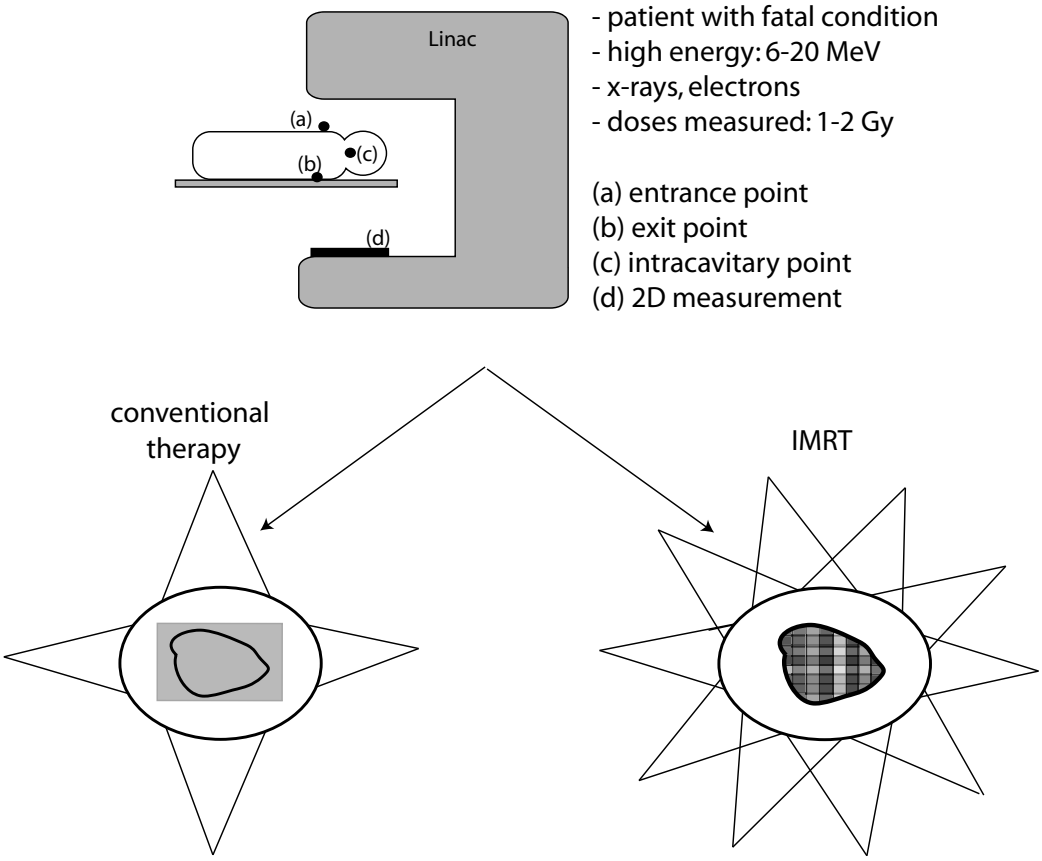

Figure 1.1: Characteristics of external radiation therapy and differences between conventional treatments and IMRT. In conventional treatments, few beams are used and a high dose is delivered to the tumor and to some healthy tissue. In IMRT, many small modulated beams are used, resulting in "tailored" dose delivery to the target volume. As a result, healthy tissue is spared.

1.1.2 IMRT

Intensity Modulated Radiation Therapy (IMRT) is arguably one of the most sophisticated forms of radiation treatments available today. As opposed to conventional radiation therapy, many fields and beam angles are used, and the dose delivery is modulated by a multi-leaf collimator (MLC) within each field. Figure 1.1 illustrates these differences: the dose distribution is conforming closely to the tumor. As a result, high dose gradients are observed outside the target volume (because of the sharp dose fall-off) and some healthy tissue is spared. The treatment planning softwares used in IMRT are based on a method called "inverse planning": the target volume, the critical organs, as well as some dose constraints are entered in the TPS, and the algorithm

itself calculates the optimal beam parameters, instead of the "trial and error" approach used in conventional TPS. Because of this, IMRT is significantly more "computer-dependent" than conventional treatments: the treatment parameters are almost entirely chosen by the planning software. Hence, a dosimetry check of the dose calculation in a solid water phantom is usually performed before the treatment. Additionally, *in vivo* dosimetry is strongly recommended.

The role of *in vivo* dosimetry in radiation therapy is two-fold:

1. to verify the calculations of the TPS at interfaces, i.e. close to the skin.
2. to evaluate the target dose in order to verify the treatment delivery process.

The former goal can be reached by using "entrance" and "exit" detectors, positioned on the patient's skin during treatment (see positions (a) and (b) in figure 1.1). According to the European Society for Therapeutic Radiation Therapy (ESTRO), the latter condition can only be fulfilled when detectors are inserted in natural body cavities (position (c) in figure 1.1), because of all the potential errors associated with entrance and exit measurements (Van Dam and Marinello, 1994). There is no universal agreement on the benefits of *in vivo* dosimetry (Feldman et al., 2001), but several large scale studies (Noel et al., 1995; Fiorino et al., 2000) confirmed that *in vivo* checks can detect systematic errors as well as estimate the accuracy of the treatment delivery. It is also recognized that major errors, such as the over-exposure of 28 patients in Panama (IAEA, 2001) in 1991, would have been avoided if an *in vivo* dosimetry program had been in place. For this reason, the use of *in vivo* dosimetry is recommended by international agencies (AAPM (TG40, 1994), ICRU (ICRU, 1976), NACP (NACP, 1980), ICRP (ICRP, 2000)). The frequency of *in vivo* measurements varies greatly among institutions. In Sweden, for example, it is common practice to perform *in vivo* entrance measurements for each patient and each treatment fraction. Other institutions choose to do *in vivo* checks once for each patient, or only for specific groups of patients (such as those treated with IMRT or other high-precision techniques). Nonetheless, *in vivo* dosimetry is performed in relatively few institutions because of time or financial constraints and its widespread use depends on the availability of user-friendly, affordable dosimeters.

1.1.3 Required accuracy

The aim of a radiation therapy treatment can be crudely summarized as: "give a sufficient dose to the tumor to guarantee tumor control as long as

the probability of serious side effects remains sufficiently low". As a result, the tumor control probability (TCP) has to be balanced against the normal tissue complication probability (NTCP). For some types of cancer, those probability curves are well defined and helped establish that the outcome of a radiotherapy treatment depends on doses that do not vary by more than $\pm$ 5 % about the optimum. This accuracy requirement is generally extended to all treatments, though some studies highlight the need of higher accuracy in some situations (Mijnheer et al., 1987; Dutreix, 1984).

1.2 Diagnostic radiology and mammography

Diagnostic radiology uses x-rays to help diagnose disease and injury. This discipline includes among others traditional x-ray imaging, CT imaging and mammography. In this work, the discussion will focus on mammography. Mammography refers to the imaging of the human breast and is mostly used as a screening tool to detect early breast cancer. Breast cancer is the most frequent cancer among women, and its incidence is generally increasing all over the world. The purpose of screening mammography is to obtain an image of the breast where potential malignancies can be identified and, ideally, not be confused with benign growth in the glandular breast tissue. The main characteristics and goals of mammography are summarized in figure 1.2. The x-ray energies encountered in mammography are low (23-35 kV), and the absorbed doses measured are of the order of 1 mGy. A higher dose will usually lead to a better contrast in the diagnostic image. However, as with any exposure to radiation, there is a small but significant risk that the x-ray exposure will induce a cancer in the radiosensitive breast tissue (BEIR, 1991). Since screening mammography involves potentially healthy subjects, as opposed to radiotherapy where the clinical intent is to cure an often deadly disease, the risk of the procedure has to be carefully balanced against the benefits.

1.2.1 International recommendations and regulations

In mammography, doses are small and do not approach the threshold for deterministic[1] effects. However, radiation-induced stochastic events are of concern. As a result, it is crucial to optimize both the equipment and the

[1]The probability of occurrence of stochastic effects increases with increasing dose, but their severity does not. Deterministic effects, on the other hand, increase in severity with increasing absorbed dose (examples include cataract, reddening of the skin, etc.)

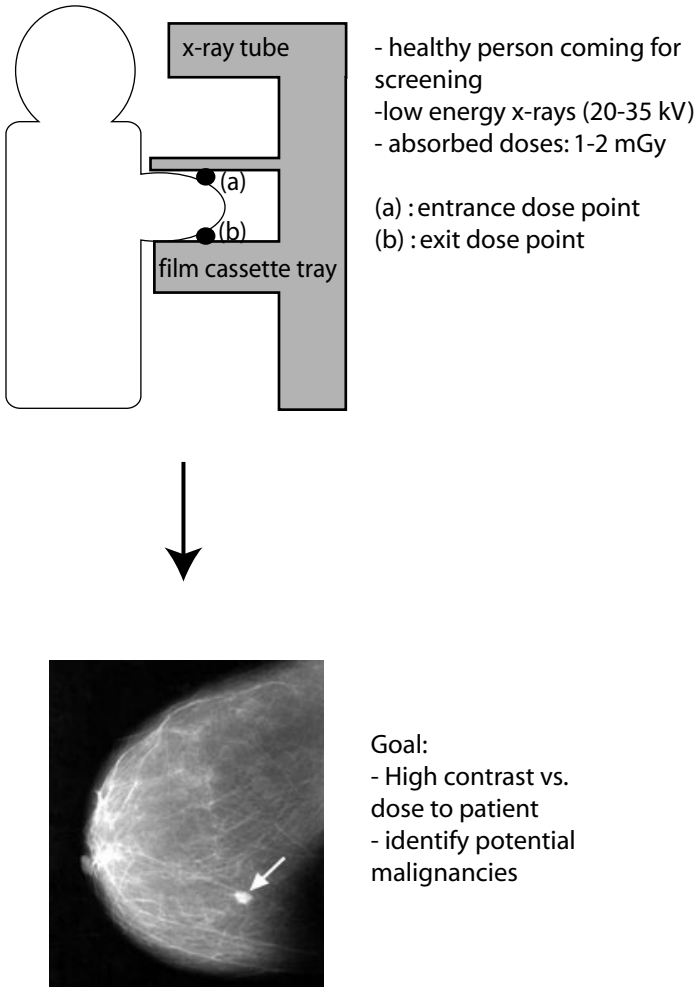

Figure 1.2: Main characteristics of a mammography screening. The goal is to obtain a high quality (high contrast) image at an acceptable dose.

imaging technique in order to produce the best diagnostic image at the lowest possible dose (following the "as low as reasonably achievable" (ALARA) recommendations for radiation protection). With modern equipment and techniques, the absorbed dose delivered to the breast per image is about 1-2 mGy but this number can vary considerably depending on the choice of technique (target/filtration combination) and the characteristics of the breast imaged (density, thickness, etc.). Some new imaging techniques (such as digital mammography) are also emerging and may result in a higher exposure in order to obtain a superior diagnostic image. Accordingly, there are international demands on quality control in mammography (Zoetelief et al., 1996). In Sweden, there is an additional requirement to make direct patient mea-

surements in mammography screening for at least 20 patients each year (SSI, 2002) using the European protocol on dosimetry in mammography (Zoetelief et al., 1996).

1.2.2 Dosimetry in mammography

The radiation risk is best characterized by the average dose to the glandular tissue of the breast (Zoetelief et al., 1996). The average glandular dose (or "mean glandular dose") can not be measured directly, but can be derived from the entrance surface dose (i.e., the absorbed dose at the top of the breast). Air is used as the reference medium (as opposed to radiation therapy dosimetry, where water is now the medium of reference) and all quality assurance dosimetry is performed using ionization chambers, in the absence of patients. If *in vivo* measurements are performed, thermoluminescence dosimeters (TLDs) on the breast can be used as a simple method of determining the dose received by the patient. However, TLDs have only a limited accuracy in these conditions and an uncertainty of the order of 30% can be expected on the measurements (Zoetelief et al., 1996). Hence, an *in vivo* dosimetry system with an increased sensitivity and precision is desirable.

1.3 Current *in vivo* dosimetry techniques

Thermoluminescence dosimeters, semiconductor diodes and films are the tools most commonly used in *in vivo* dosimetry to date. The purpose of this section is to offer a brief overview of their characteristics, and highlight potential pitfalls.

1.3.1 The standard: ionization chambers

The "state of the art" of radiation dosimeters is without doubt the ionization chamber (or ion chamber).Different types of ionization chambers are available, from "free-air" (used only in standards labs) to cylindrical chambers (most commonly used in radiation therapy) or parallel plate chambers (used for electron dosimetry or in diagnostic radiology). When the chamber (connected to an electrometer) is exposed to radiation, ion pairs are created in the sensitive air volume. A high voltage applied across the chambers enables these ion pairs to be collected, and the resulting current can be converted to absorbed dose after the application of several correction factors. Those correction factors include: correction for atmospheric conditions (temperature and pressure), for recombination of the ion pairs within the air volume, etc.

In standard conditions with well-defined correction factors, ionization chambers are extremely precise and accurate, making them an invaluable tool for QA measurements. Though some sealed ionization chambers can be used for *in vivo* measurements, their current use is mostly limited to phantom measurements.

1.3.2 Thermoluminescence dosimeters

When certain crystalline materials are heated following irradiation, they emit light proportionally to the amount of radiation dose absorbed. This principle, known as thermoluminescence, has been recognized for several decades for its potential in dosimetry (see chapter 2). Today, thermoluminescence dosimeters (TLDs) are used both in radiation therapy and in diagnostic radiology (Berni et al., 2002). TLDs offer the best option for *in vivo* measurements in mammography because of their high sensitivity and small size: they can be placed anywhere on the skin or inside the body without the inconvenience of cables. In regions of high dose gradients, several TLDs can be used to obtain many dose points over an area of interest. Lithium fluoride is the most popular TLD material because of its tissue equivalence ($Z_{eff} \simeq 8$, compared to about 7 for tissue[2]) and high sensitivity: it can be used to measure dose ranging from 10 μGy to 10^3 Gy (Johns and Cunningham, 1983). However, TLDs suffer from sensitivity variations between readings. As a result, they have to be calibrated before every use. Annealing (i.e., resetting the TLDs by heating them) needs to be performed after each measurement. With great care in manipulation from an experienced technician, a reproducibility of about 2% can be reached (Johns and Cunningham, 1983). The overall TLD handling process is a time consuming procedure, which can take up to several hours. Another major pitfall of TLDs is their relatively low precision in daily clinical uses. As a result, the total uncertainty on dose determination can be high: one study reported deviations up to 7% (1 SD) for in vivo TLD measurements of patients over a 7 year period (Kalef-Ezra et al., 2002).

1.3.3 Semiconductor diodes

Diodes have been widely accepted in medical dosimetry because they are robust and relatively simple to operate. They also offer the advantages of high sensitivity, and immediate read-out. Silicon diodes are available as either "p-type" or "n-type" depending on their minority charge carriers. There seems to be a trend to favor p-type diodes, although recent studies contest

[2]See chapter 2 for a definition of Z_{eff} and tissue equivalence issues.

their advantages over n-type diodes in terms of dose-rate dependence and resistance to radiation damage (Jornet et al., 2000; Saini and Zhu, 2004). In *in vivo* dosimetry, diodes are commonly used for entrance and exit dose measurements. The sensitivity of the diode detector depends on the lifetime of the charge carriers and will decrease with accumulated dose (Jursinic, 2001; Rikner and Grusell, 1987). This reaction to radiation damage is the main limitation of silicon diodes. Other factors to be considered are their energy dependence (Z_{Si} =14), dose rate dependence (Wilkins et al., 1997) and temperature dependence (Rikner and Grusell, 1987). Because of these dependencies, several correction factors have to be applied to the diode signal (Meiler and Podgorsak, 1997). Diodes also suffer from angular dependence, and one recent study recommends to limit the angles of incidence of the beam to no more than ± 45 degrees in electron beams (Marre and Marinello, 2004). It is generally agreed that diodes have a higher precision than TLDs (Loncol et al., 1996). However, there seems to be no consensus on the achievable *in vivo* accuracy: many studies report an accuracy below 3 % (1SD) (Jursinic, 2001; Essers and Mijnheer, 1999), but other researchers quote accuracies around 10% (Alecu and Alecu, 1999). In particular, Higgins et al. (2003) used diodes for IMRT quality assurance, and found deviations up to 16% for individual field measurements. The same authors suggest that an accuracy of ± 10% at best should be expected for IMRT measurements. These discrepancies can be explained by the fact that entrance dose measurements depend critically on accurate calibration factors. Indeed, a surface diode is exposed to a different spectrum than a detector positioned at depth. This effect can be minimized if a thick build-up cap is used to achieve electron equilibrium, but as a result the dose delivered to the target volume under the diode will be decreased. Heukelom et al. (1991) insist on the necessity of accurate calibration factors, and the need for frequent re-calibration for good agreement with ion chamber measurements. It is likely that *in vivo* diode measurements could achieve a higher accuracy if performed at depth. New diodes are being developed for insertion in the patient (especially for IMRT measurements), however no clinical studies are available at this time. Perhaps the great advantage of diodes over TLDs is their relative ease of use and time saving potential: no annealing procedure is necessary, calibration is less frequent, and the dose estimate is available almost immediately.

1.3.4 2D techniques

Though this review concerns mainly point dosimeters, 2D *in vivo* dosimetry techniques such as radiographic film, or Electronic Portal Imaging Devices (EPIDs) need to be mentioned for the sake of completeness. These detectors

give a measure of the transmission dose through the patient (see position (d) in figure 1.1). The obvious advantage of these dosimeters is that they can be used to record the dose across the whole field. The response of radiographic (AgH) films tends to vary with depth and field size due to an over-response to low energy photons (Khan, 1992). Few solid references are available for the adequate handling of radiographic films in *in vivo* dosimetry, but some national recommendations for film dosimetry are being processed (TG69, 2005). Radiochromic films change color after irradiation and do not need chemical processing. Their response is however still dependent on many parameters (such as emulsion differences between film batches and post irradiation conditions). Hence, the handling conditions can be quite elaborate if high accuracy is desired (Butson et al., 2003; Ciocca et al., 2003). EPIDs are commonly used as an imaging device, to verify the patient's position before treatment. EPID dosimetry, though, is a relatively new field. TG58 (2001) quote an achievable accuracy below 5% but advise caution due to quality control and calibration issues.

1.4 Novel dosimetry techniques

Several novel approaches have been reported in the literature, and the most significant are reported in this section. In general, they are still in the development stage and therefore not used clinically (except in very few institutions).

1.4.1 MOSFETs

Metal oxide semiconductor field-effect transistors (MOSFETs) are commercially available and offer the advantages of instant read-out, extremely small size, and permanent storage of the dose (Soubra et al., 1994; Butson et al., 1996; Rosenfeld, 2002). In spite of this, their clinical application has been limited, probably because of their angular dependence, their change of sensitivity with use, and their relatively short lifetime (Ramani et al., 1997; Peet and Pryor, 1999; Scalchi and Francescon, 1998). It has to be noted that some recent improvements have fixed most of the reported problems for MOSFETs (Cheung et al., 2004; Ramasehan et al., 2004) and new formats ("micro-MOSFETs", 2D-array) renewed the interest in MOSFETs for medical dosimetry. New studies (Dong et al., 2002), (Rowbottom and Jaffray, 2004) testify to their potential in radiotherapy and diagnostic imaging. However, the precision is still lower than for diodes, resulting in a higher uncertainty on the dose determination (Jornet et al., 2004) (precision 0.7% 1SD for MOS-

FETs and 0.05% for diodes). MOSFETs have a very high spatial resolution (Kron et al., 2002), making them suitable for small field measurements like IMRT: Chuang et al. (2002) quote an agreement within 5% of TPS dose for MOSFETs for a phantom verification of an IMRT treatment. Ramasehan et al. (2004) conclude that an accuracy of 5% in *in vivo* dosimetry is possible, but warn of the necessity to wait 2 minutes between read outs because of the so-called creep-up effect: this is not a problem for conventional radiation therapy, but prevents the use of MOSFETs if individual field doses are desired in IMRT.

1.4.2 Diamond detectors

The use of synthetic diamonds as *in vivo* radiation detectors has been reported as early as 1987 (Nam et al., 1987). Diamonds have been considered suitable for clinical purposes because of their small size and good tissue equivalence. They are also resistant to radiation damage. However, their use for *in vivo* dosimetry can be impaired by their dose-rate dependence and the need for pre-irradiation (Laub et al., 1999; Hoban et al., 1994; Bucciolini et al., 2003). Diamond detectors exhibit high sensitivity and high resolution (with a sensitive volume of 1 mm^3), but their advantage over diodes is debated (Heydarian et al., 1993) except in very small fields (Heydarian et al., 1996). Diamond detectors also have less angular dependence than diodes in electron beams (Bjork et al., 2000). Laub and Wong (2003) demonstrated the need of a small dosimeter for small IMRT fields, and recommend the use of diamond detectors, TLDs or water equivalent scintillators. Bucciolini et al. (2003) compared diamond detectors to diodes and ionization chambers, and concluded that in spite of their positive characteristics, diamonds did not offer a significant advantage over diodes in photon beams in conventional radiation therapy.

1.4.3 Optical fiber dosimetry

Plastic scintillators Plastic scintillator systems also offer excellent tissue equivalence, but their present design makes it difficult to subtract the noise signal produced in the light-guide (Cerenkov radiation and fluorescence) from the signal originating from the actual plastic scintillator chip (Beddar et al., 1992a,b). Several approaches have been reported to improve the signal-to-noise ratio. One approach consists in adding a "blank" optical fiber for subtraction of the light-guide signal: this can compromise the size of the optical fiber bundle (Beddar et al., 1992c) and make the scintillator probe too bulky to be inserted in a patient. Another approach is the optimization of the

coupling between the fiber and the scintillator which, so far, has only had a limited success in reducing the influence of the noise signal from the light guide (Beddar et al., 2003, 2004). Plastic scintillation dosimetry may benefit from a renewed interest if this problem gets solved.

Optically stimulated luminescence Optically stimulated luminescence (OSL, see chapter 2) is related to thermoluminescence, but uses light (e.g., from a laser) instead of heat as the stimulation source. Huston et al. (2001) described an OSL system for radiation therapy that uses two light guides (one for the laser light, the other for the signal) and copper-doped glass as the detector. This system demonstrated a very high sensitivity, dynamic range, and stability (Huston et al., 2001), no dose rate dependence, and little energy dependence (Huston et al., 2002). Though promising, this system has not been applied in internal *in vivo* dosimetry to date. OSL signals from aluminum oxide doped with carbon (Al_2O_3:C) were also investigated by a group in Orsay, France: the system consists of a relatively large pellet of Al_2O_3:C (4 to 10 mm in diameter) and two light guides (Roy et al., 1997). Few results have been reported from this system, which seems to be designed for radioprotection dosimetry more than *in vivo* radiotherapy applications.

1.5 Practical issues: time and money

The ideal *in vivo* dosimetry system should:

- have a high accuracy
- be safe (no electronics/high voltage close to the patient)
- have a small size
- have no or few dependencies on beam parameters
- provide the absorbed dose in real-time
- be comprehensive (able to function in both photon and electron beams)
- be easy to use and calibrate
- be affordable

Table 1.1 summarizes the principal characteristics of the *in vivo* dosimeters mentioned in the previous section and figure 1.3 illustrates their respective size. Overall accuracy is not the only requirement of a useful *in*

vivo dosimeter: indeed, the spread of *in vivo* dosimetry has been limited by practical issues, such as cost and time. Acquisition costs vary greatly among dosimetry systems, and so does the amount of time the physicist (or other person in charge) spends preparing and calibrating the system. Essers and Mijnheer (1999) report that the total time invested for a comprehensive *in vivo* dosimetry program with diodes in conformal radiotherapy is about 1.5 day/week, or 0.3 full-time equivalent (for two measurements per patient, three patients per week). Calibration is quicker for TLDs (there are fewer calibration factors), but the overall time spent for patient measurements is longer. Essers and Mijnheer (1999) conclude than a diode program would be cheaper than TLDs for most institutions. Diodes are an extremely convenient tool for quality assurance dosimetry, and most clinical institution have some experience using them. Hence, the time and skill investments needed to transfer that knowledge to *in vivo* dosimetry is greatly reduced compared to the acceptance of new dosimetry techniques, such as MOSFETs or diamond detectors. As far as acquisition costs are concerned, a diamond detector system is generally considered expensive (Bucciolini et al., 2003). The relatively low lifetime of MOSFETs could also make them an expensive dosimetry system in the long run. The time involved in calibrating these systems can not be evaluated before their characteristics are better defined.

1.6 This thesis

The work summarized in this PhD thesis describes the development of a new real-time dosimetry system for *in vivo* dosimetry and its applications in radiotherapy and mammography. The intent was to develop a point dosimeter which would be highly accurate and would offer real-time information about the dose delivered to the point of measurement. This approach uses optical fibers and the OSL from Al_2O_3:C but differs from the systems described in section 1.4.3 in several critical aspects: its size, its sensitivity and the use of the radioluminescence (RL) signal emitted by Al_2O_3:C during irradiation.

Chapter 2 describes the physical principles behind RL and OSL, and investigates the characteristics of Al_2O_3:C as a tissue-equivalent dosimeter. Chapter 3 deals with instrumentation features, as well as the methods developed to obtain reliable absorbed dose assessments from the RL and OSL signals. Chapter 4 presents the response of the RL/OSL dosimeter in relation to beam parameters: the reproducibility, linearity, energy dependence, etc of the system will be detailed there. Chapters 5 and 6 present the application of the RL/OSL dosimeter and the results of the first patient measurements in radiotherapy and in mammography, respectively. In addition, chapter 6

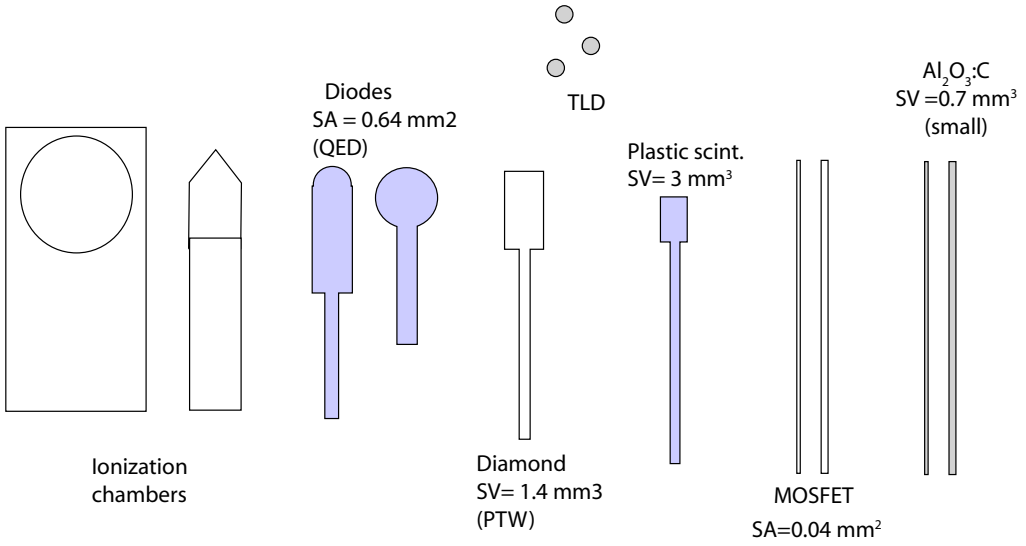

Figure 1.3: Several commonly used point dosimeters, their size and sensitive volume (SV) or sensitive area (SA).

investigates the influence of the design of the RL/OSL probes with Monte Carlo simulations.

During the course of this thesis work, the following articles have been produced:

1. Aznar MC, Nathan R, Murray AS and Bøtter-Jensen L (2003) Determination of differential dose rates in a mixed beta and gamma field using shielded Al_2O_3:C : results of Monte Carlo modelling. Radiation Measurements vol.37 (4-5), pp 329-334.

2. Aznar MC, Andersen CE, Bøtter-Jensen L, Back SAJ, Mattsson S, Kjaer-Kristoffersen F and Medin J (2004) Real-time optical-fibre luminescence dosimetry for radiotherapy. Physics in Medicine and Biology vol.49, pp 1655-1669.

3. Aznar MC, Hemdal B, Medin J, Marckmann CJ, Andersen CE, Bøtter-Jensen L, Andersson I, Mattsson S. In vivo absorbed dose measure-

ments in mammography using a new real-time luminescence technique. British Journal of Radiology. In Press.

4. Aznar MC, Medin J, Hemdal B, Thilander Klang A, Bøtter-Jensen, L, Mattsson S. A Monte Carlo study of the energy dependence of Al_2O_3:C crystals for real-time in vivo dosimetry in mammography. Radiation Protection Dosimetry. In Press.

5. Andersen CE, Aznar MC, Bøtter-Jensen L, Back SAJ, Mattsson S and Medin J (2003) Development of optical fibre luminescent techniques for real-time *in vivo* dosimetry in radiotherapy. Standards and code of practice in medical radiation dosimetry : Proc. Int. Symp. Vienna, IAEA (2002), vol. 2 pp 353-360.

6. Marckmann CJ, Aznar MC, Andersen CE and Bøtter-Jensen L. Influence of the stem effect on radioluminescence signals from optical fiber Al_2O_3:C dosemeters. Radiation Protection Dosimetry. In Press.

7. Andersen CE, Marckmann CJ, Aznar MC, Bøtter-Jensen L, Kjær-Kristoffersen F and Medin J. An algorithm for real-time in vivo dose-rate measurements using the radioluminescence signal from Al_2O_3:C . Radiation Protection Dosimetry. In Press.

8. Marckmann CJ, Andersen CE, Aznar MC and Bøtter-Jensen L. Novel optical fiber dosimeter systems for clinical applications based on radioluminescence and optically stimulated luminescence from Al_2O_3:C . Radiation Protection Dosimetry. In Press.

9. Edmund JM, Andersen CE, Marckmann CJ, Aznar MC, Akselrod MS and Bøtter-Jensen, L. An optimized CW-OSL measurement protocol using optical fibre Al_2O_3:C dosimeters. Radiation Protection Dosimetry. In Press.

10. Buckley L, Rogers, DWO, Aznar M and Medin J. Monte Carlo calculated dose to Al_2O_3 per unit dose to water in photon beams compared to measured OSL response per unit dose to water. Presentation at the AAPM annual meeting, Pittsburgh PA July 2004.

Dosimeter	cable	size	delay between meas.	dose	dose accumulation	dose rate	temp.	energy	direction	overall accuracy
Diodes	X	X	0	0	XX	XX	X	XX	X	0
TLDs	0	0	X	X	X	0	0	X	0	X
MOSFETs	0	0	X	0	XX	XX	X	0/X	0/X	0/X
Diamonds	X	0	0	0	0	XX	0	0	0	X
Plastic scintillators	XX[1]	0-X	0	0	0	0	0	0	0	X[1]

Table 1.1: Summary of the characteristics of different in vivo point dosimeters: 0=no concern, X= mild concern, XX=major concern (based on (Van Dam and Marinello, 1994) and adapted for novel dosimeters)

. 1: for plastic scintillators, the noise signal generated in the cable has prevented clinical applications to date.

2 Luminescence dosimetry with Al_2O_3:C

Before describing the RL/OSL dosimetry system based on Al_2O_3:C which is the topic of this thesis, it is necessary to consider in some detail the characteristics of Al_2O_3:C, first as a luminescent material, and secondly as a potential *in vivo* dosimeter. In the next section, the unique luminescence characteristics of Al_2O_3:C are described, with an emphasis on its use in real-time optical fiber dosimetry. Subsequently, the physical quantities and units which will be used in this work are defined and some theoretical considerations of the interaction of radiation with Al_2O_3:C are provided.

2.1 Principles of luminescence

2.1.1 Band gap theory

The different processes by which non-thermal energy transforms into light are grouped under the term luminescence. When certain materials with a crystalline structure are exposed to ionizing radiation, luminescence can arise from either thermal or optical stimulation. The overall process can be broken down in three steps:

1. ionization due to exposure of the crystal to radiation
2. storage of radiation energy
3. stimulation

. In a solid, where atoms are closely bound together, electrons populate bands of allowed energy states, separated by "forbidden" bands. The "band gap" is defined as the forbidden energy band between the two outermost allowed bands in a solid, namely, the conduction band and the valence band.

The valence band is the lower band of allowed energy states, and is usually filled with electrons. In the band gap model, absorption of energy (e.g., from ionizing radiation) in a crystalline structure results in the creation of electron-hole pairs: if sufficient energy is provided to an electron to break from the valence band and overcome the band gap, this electron is moved to the conduction band, where it can move freely about the crystal (see figure 2.1). The deficit of negative charge in the valence band creates a "hole". The width of the band gap depends on the material considered: luminescent materials have a wide band gap (e.g., around 9 eV for Al_2O_3:C (Akselrod et al., 1998)). Once in the conduction band, the electron quickly loses its excitation energy and can either

- fall back to the valence band immediately and recombine with a hole
- or get trapped at defects within the crystalline structure

. Traps are defined as crystal defects which are able to capture a charge carrier (electron or hole) and release it to its original band. Some particular defects that can hold both electrons and holes are referred to as "recombination centers". A trapped electron will remain so until it is provided with enough stimulation energy to overcome the trap and eventually recombine with a hole at a recombination center. These recombinations can result in the emission of light, i.e. luminescence. Several factors compete with the production processes: some hole traps are classified as non-radiative recombination centers (a hole-electron recombination in those traps won't lead to emission of light). Similarly some electron traps are not responsive to stimulation by light and won't easily release their trapped electrons: they are referred to as "optically deep traps". "Shallow traps" on the other hand are unstable at ambient temperature, and may release their trapped electrons even without external stimulation. In general, radiative processes which happen during the exposure of the crystal to radiation are classified as "prompt luminescence" or radioluminescence, "RL". In case of an emission during stimulation, this phenomenon is referred to as "optically stimulated luminescence" or "thermoluminescence" depending on whether the stimulation source is light or heat. The presence of shallow, deep traps, as well as non-radiative traps are grouped under the term "competing processes", because they interfere with the type of luminescence which is of dosimetric interest. The luminescence emitted by Al_2O_3:C crystals is characteristics of the oxygen vacancy centers introduced by the presence of carbon impurities (in concentrations up to 5000 ppm). The occupancy of an oxygen vacancy center by two electrons gives rise to a neutral "F" center, whereas occupancy by one electron forms a positively charged "F^+" center. The main luminescence emission occurs around 420 nm

and is believed to be caused by:

$$F^+ + e \rightarrow F^* \rightarrow F + h\nu \tag{2.1}$$

where F^* is an excited F center, which decays to the ground state with the emission of a photon at 420 nm (Yukihara et al., 2003). The process is associated with a relaxation time of approximately 35 ms.

2.1.2 Uses of Al_2O_3:C in non-medical dosimetry

During the last 20 years, OSL techniques have been successfully applied to environmental dosimetry (Huntley et al., 1985; Bøtter-Jensen, 1995; Bøtter-Jensen et al., 1997), now widely replacing thermoluminescence (TL) methods. The advantages of OSL over TL are, among others, an increased sensitivity, fast reading, the possibility of making repeated read-outs and the absence of heating processes. The materials used in environmental dosimetry are mostly quartz and feldspars because of their abundance in soils. Al_2O_3 appeared on the thermoluminescence dosimetry scene in the mid-50ies, but its sensitivity was too low for uses in environmental dosimetry. The dosimetric properties of pure Al_2O_3 were improved significantly by introducing oxygen vacancies under strong reducing conditions and in the presence of graphite: TL measurements with Al_2O_3:C single crystals were first reported by Akselrod et al. (1990). Single crystals are grown as rods of varying diameters (down to 200 mm). The most interesting features of Al_2O_3:C are its excellent OSL sensitivity, reproducibility and linearity. Bøtter-Jensen et al. (1997) showed that the OSL detection limit of standard Al_2O_3:C chips (5 mm diameter and 1 mm thickness) is below 1 mGy. The response of OSL is linear with dose over a very large range (0.05-50 Gy), as demonstrated by McKeever et al. (1996) and Polf et al. (2002). Al_2O_3:C detectors have been used in personal dosimetry for over 50 years and are commercialized by Landauer Inc. (Chicago, USA). As part of this project, the response of Al_2O_3:C to gamma and beta radiation from the soil was studied, in order to investigate the potential of an RL/OSL optical fiber dosimeter in environmental dosimetry (Aznar et al., 2003).

2.2 OSL from Al_2O_3:C

When the crystal is stimulated by light to produce OSL, the resulting signal starts at a high value and decreases with time. The depletion of the signal as stimulation continues indicates that the supply of electrons from the OSL traps is becoming exhausted. As seen with the band gap model, the OSL

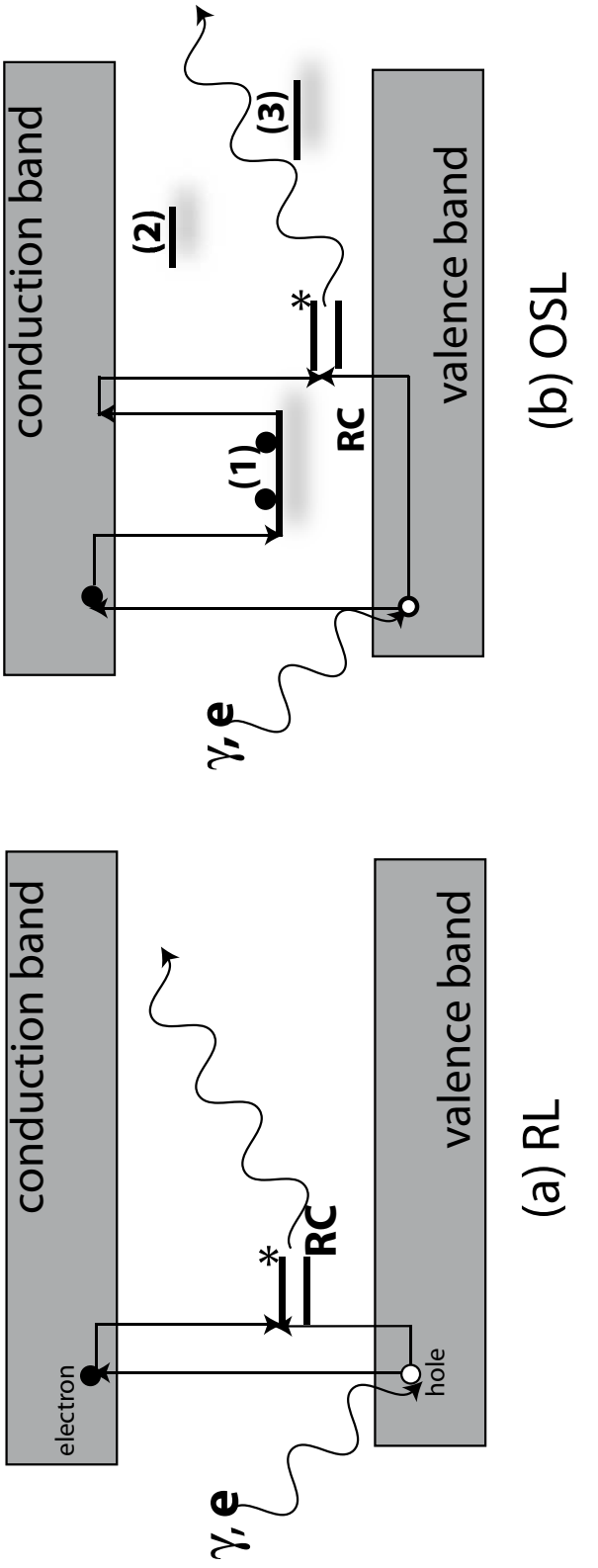

Figure 2.1: Band gap theory: prompt luminescence or "RL" (a) and stimulated luminescence e.g. "OSL" (b). RC: recombination center. *: excited state of the recombination center. (1) OSL trap, (2) shallow trap, (3) deep trap.

signal will depend on several factors, such as the number of traps, their capacity to release a charge carrier under stimulation (referred to as the "photoionization cross section"), the number of electrons in the traps after the end of the exposure. It will also depend on the wavelength of the stimulation (related to how much energy is imparted to the trapped electrons). These parameters and their influence on the rate and the shape of the OSL decay curve are discussed in this section. Theoretical models have been developed in great detail to describe the complex phenomena involved in OSL[1], and only a brief review will be given here. This model is based on several assumptions: there is only one type of electron trap and one type of recombination center, all charge transport takes place via the conduction band, etc. The OSL intensity can be described as:

$$I_{OSL} = -\eta \cdot \frac{dm}{dt} \tag{2.2}$$

where η is the luminescence efficiency (η=1 if all the recombinations are radiative) and m is the concentration of trapped holes. If we assume that the crystal is in quasi-equilibrium (no free electrons in the conduction band) and we have charge neutrality in the crystal, then $dm/dt = dn/dt$ (where n is the concentration of trapped electrons), and equation 2.2 becomes:

$$I_{OSL} = -\frac{dn}{dt} \tag{2.3}$$

On another hand, if we assume that there is no retrapping (all ejected electrons will lead to radiative recombinations), then we can write:

$$I_{OSL} = n \cdot \sigma(\lambda) \cdot \phi(\lambda) \tag{2.4}$$

where ϕ is the intensity of optical stimulation and σ is the photoionization cross section. Combining equations 2.2 and 2.4 shows that the OSL signal can be described as an exponential decay, such as:

$$I_{OSL} = I_{OSL_0} \cdot \exp(-\frac{t}{\tau}) \tag{2.5}$$

where $\tau = \sigma(\lambda) \cdot \phi(\lambda)^{-1}$ and can be seen as a lifetime. This model is referred to as the "one trap-one center model": if several traps are considered, the OSL signal will be a sum of several exponentials, depending on the specific ionization cross section of each type of traps. However, the presence of competing

[1] A more complete discussion of OSL mathematical models is provided in the book "Optically stimulated luminescence dosimetry" by L. Bøtter-Jensen, S.W.S. McKeever and A.G. Wintle, (Elsevier Science, Amsterdam, 2003).

processes (e.g., deep traps) is going to disturb these exponential relationships. It can be shown that the one trap model can be expanded to account for shallow and deep traps in the following fashion:

$$I_{OSL} = I_{OSL_0} \cdot \exp(-\frac{t}{\tau}) + a_1 \cdot \exp(-\frac{E}{kT}) - a_2(t) \tag{2.6}$$

where the term following a_1 describes the action of shallow traps (E being the trap depth, T the temperature, and k the Boltzmann constant), and $a_2(t)$ describes the time dependent influence of deep traps. These two terms give rise to a very slow, temperature dependent component in the OSL decay curve. The shape of the OSL decay will vary according to the relative distribution of OSL traps with respect to deep and shallow traps in the crystal (which is determined partly by the growth conditions). As a result, some OSL signals decay in an exponential fashion, while some others will display a more complex pattern.

2.3 RL from Al_2O_3:C

RL is produced continuously when the material is irradiated and information about the irradiation can be obtained in real-time. The different components of the RL signal are illustrated in figure 2.2. At the beginning of the irradiation, a "slow-rise" phenomenon can be observed. This is referred to as the "transient". As the crystal is being irradiated, the electrons transported to the conduction band can either get trapped (OSL) or recombine promptly (RL). As the OSL traps are being filled, they offer less competition to RL recombinations. This produces a "sensitization" of the crystal (Erfurt and Krbetschek, 2002), and thus the RL signal increases with irradiation time. The signal eventually reaches a plateau (as observed by (Erfurt et al., 2000)). However, absorbed doses relevant for medicine are too small to observe this phenomenon, and the RL signal usually presents a continuous increase during the irradiation. At the end of the irradiation, the signal does not immediately return to background level; this afterglow is caused by some charge being released from the shallow traps, giving rise to phosphorescence.

2.4 Dosimetric considerations

2.4.1 Interaction of radiation with matter

When a photon beam (e.g., megavoltage x-rays) passes through an absorbing medium (such as water or body tissue), some energy is transferred to

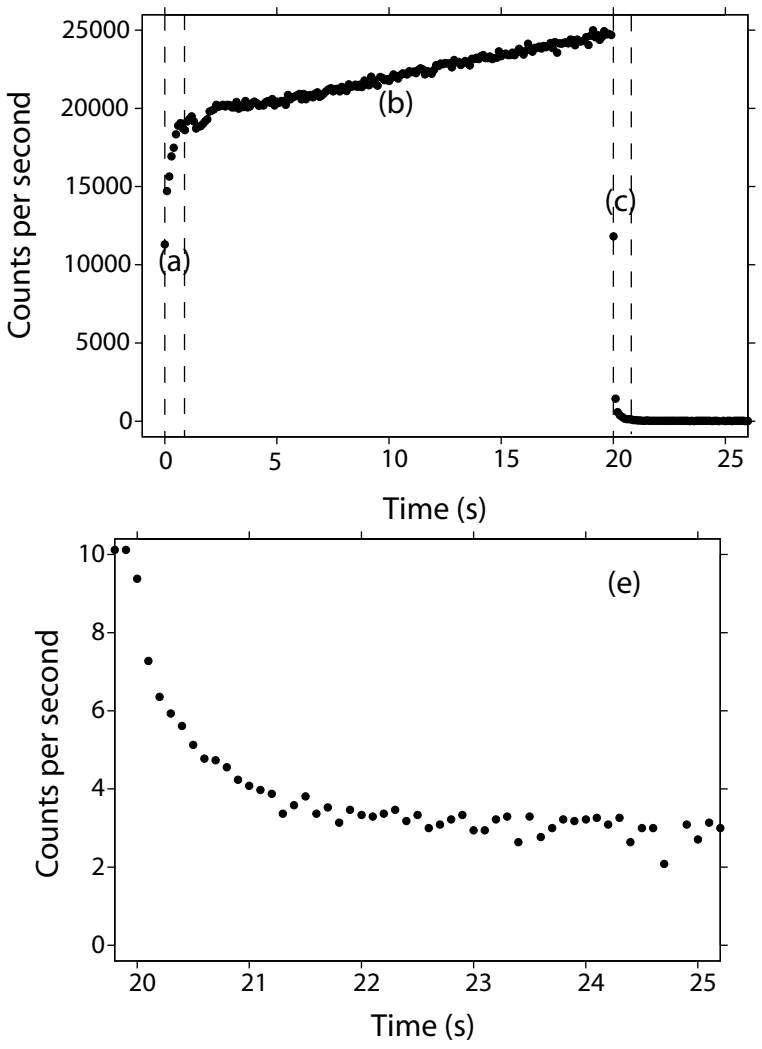

Figure 2.2: Components of the RL signal for exposure at a constant dose rate. Top: the whole RL signal from Al_2O_3:C for an absorbed dose of 1 Gy, (a) transient, (b) slope due to sensitization, (c) afterglow. Bottom (e): after the end of the irradiation, some afterglow is observed due to the presence of shallow traps.

the medium. The fraction of this energy which is eventually absorbed in the medium can be used as a predictor of biological damage. The interaction of photons with matter in the energy range used in radiation medicine is described by three majors effects: the photoelectric effect, Compton incoherent

scattering, and pair production. Their characteristics are very simply summarized in figure 2.3. A fourth process, coherent (or Rayleigh) scattering also takes place, but is much less prevalent at the energies considered in radiation medicine. The relative occurrence of the different processes is usually expressed in terms of cross-sections. The cross-section for a given event is the number of events divided by the incoming fluence and has the dimension of area. For example, the attenuation undergone by a photon beam in a medium of thickness Δx is described by the linear attenuation coefficient (ICRU, 1998), defined as:

$$\mu = \frac{\text{number of photons interacting in } \Delta x}{\Delta x} \tag{2.7}$$

Most commonly, the attenuation characteristics of the medium are described by the mass attenuation coefficient, μ/ρ. Since the absorption of energy is related to the biological effect, the mass energy absorption coefficient is the quantity of interest and can be calculated as:

$$\mu_{en}/\rho = \mu/\rho \cdot \frac{\bar{E}_{ab}}{h\nu} \tag{2.8}$$

where $\bar{E}_{ab}$ is the average energy absorbed per interaction, and hν is the energy of the photon (ICRU, 1998). One fundamental quantity is the kerma (kinetic energy released per unit mass). It is defined as:

$$K = \frac{dE_{tr}}{dm} \tag{2.9}$$

where dE_{tr} is the sum of the initial kinetic energies of all the charged particles (electrons and positrons) liberated by the uncharged particles (photons) in a mass dm of material. The kerma is expressed in J.kg^{-1} or Gray (Gy) The kerma concerns the initial transfer of energy to matter. However, the quantity of interest in most dosimetric situations is the absorbed dose within a certain volume, which is defined as:

$$D = \frac{d\bar{\epsilon}}{dm} \tag{2.10}$$

where $d\bar{\epsilon}$ is the mean energy imparted to matter of mass dm. The unit of absorbed dose is also Gy. If certain conditions are respected (i.e., if charged particle equilibrium exists across the volume of interest and if radiative losses are negligible), then equality between absorbed dose and kerma is approached.

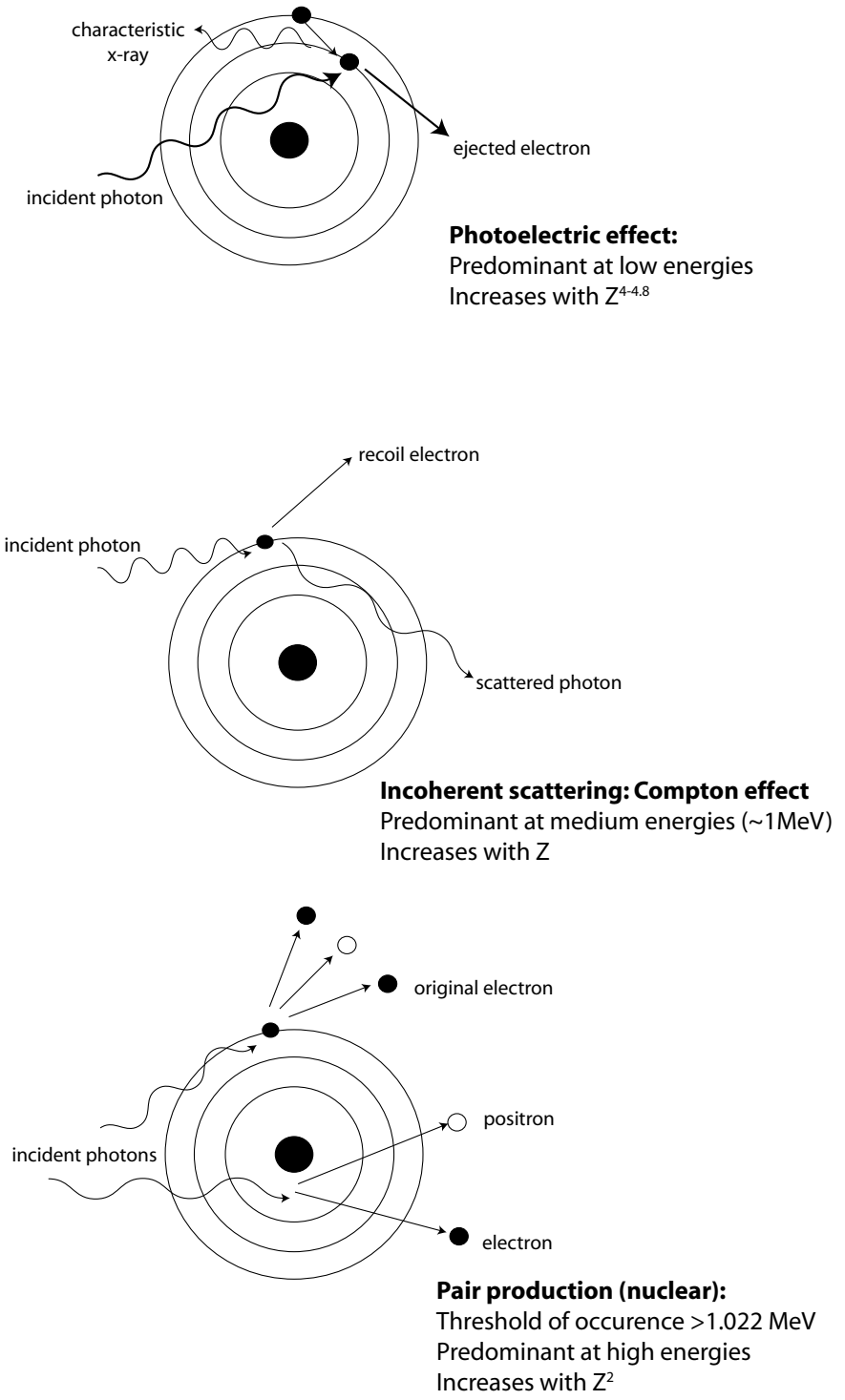

Figure 2.3: Characteristics of the major interaction processes: photoelectric effect, Compton scattering and pair production.

2.4.2 Tissue equivalence

In order to be as accurate as possible, a dosimeter must respond to radiation the same way body tissue would. This requirement is hard to satisfy as was seen in chapter 1. For a closer look at tissue equivalence (and resulting energy dependence), it is useful to know the respective proportion of the interaction processes. Figure 2.4 compares the relative importance of interaction processes for a wide range of energies. Because of the higher effective atomic number of Al_2O_3, the photoelectric effect is dominant for a wider range of energies than for water. At low energies (10-20 keV), it is clearly dominating all other interaction processes. Also the pair production process (which is strongly dependent on Z) is becoming significant for Al_2O_3 around 10 MeV (compared to around 30 MeV for water). This could have an influence on the response of Al_2O_3 at high radiotherapy energies. A quick way to estimate whether a material is tissue equivalent or not is to look at its atomic number (Z). For composite materials (air, Al_2O_3), an approximative value of the effective atomic number (Z_{eff}) can be calculated according to equation 2.11 (Johns and Cunningham, 1983).

$$Z_{eff} = \sqrt[m]{a_1 Z_1^m + a_2 Z_2^m + \ldots} \tag{2.11}$$

In the radiotherapy energy range, the Compton effect is the predominant mode of interaction: since the cross section for the Compton effect depends on Z, $m = 1$. For Al_2O_3, this results in $Z_{eff} = 10.2$ compared to 7.5 for tissue. In the diagnostic energy range however, the photoelectric effect, whose cross section depends on approximately the fourth power of Z, is predominant. It is recommended to use $3.4 < m < 3.8$ (Johns and Cunningham, 1983), leading to $Z_{eff} = 11.4$ for Al_2O_3. These results indicate that Al_2O_3 is not tissue equivalent. The tissue equivalence of a material can also be investigated in detail by looking at the way radiation interacts with it over a range of energies. In photon beams, this would imply looking at the mass energy absorption coefficient, or rather at the ratio of the mass energy absorption coefficients of the material of interest and a reference material (water for radiation therapy, as the human body is close to water). The ratio of μ_{en}/ρ of many materials with respect to water is presented in figure 2.5. Among all those dosimetric materials, plastic (vinyltoluene) has the flattest energy response, and graphite (i.e., diamond) is the closest to water. Al_2O_3 will underestimate the dose (compared to water) for energies 0.3 to 3 MeV, but will overestimate the dose to water outside of this range. However, this behavior is less pronounced than for silicon. The interaction of charged particles (such as electrons) is described by the mass stopping power (usually expressed in $MeV.cm^2.g^{-1}$). Figure 2.6 shows that Al_2O_3 has a slightly flatter response

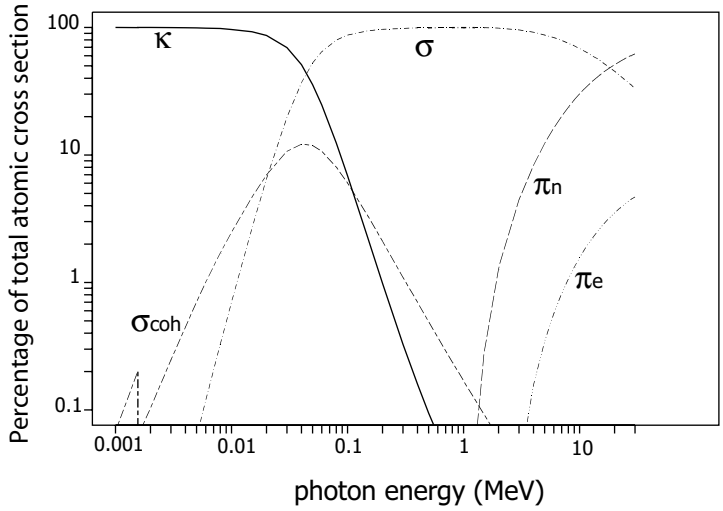

(a) Al_2O_3

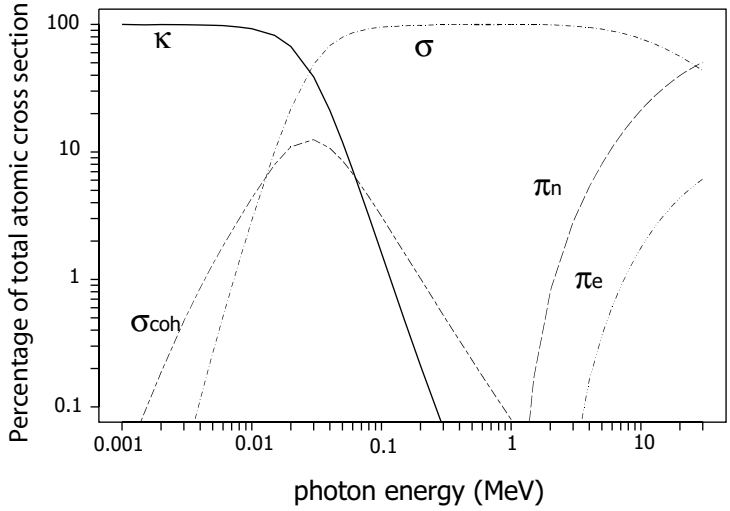

(b) water

Figure 2.4: Predominance of interaction processes: photoelectric effect (κ), Compton scattering (σ), coherent scattering (σ_{coh}), pair production (π_n in a nuclear field, π_e in an electron field). Source: NIST (XCOM).

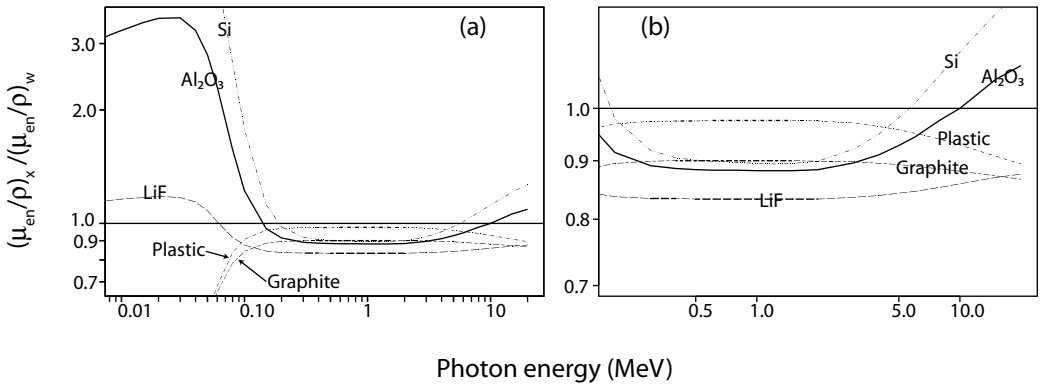

Figure 2.5: (a): Ratio of mass energy absorption coefficients of many dosimetric materials with respect to water, (b): detail at high energies. Source: NIST (XCOM).

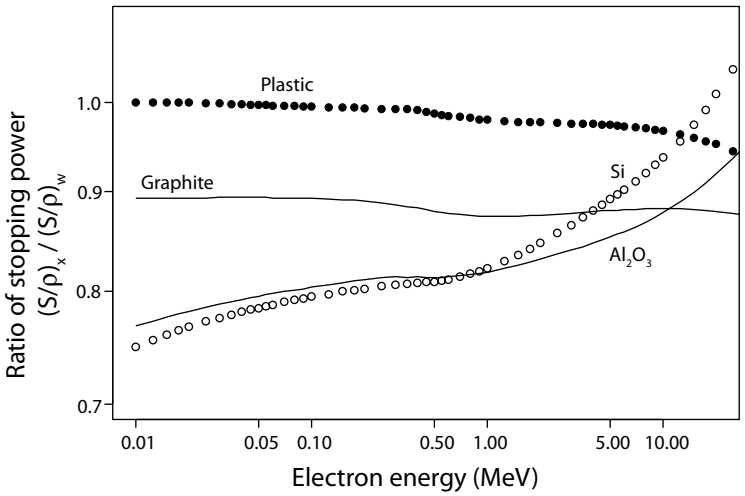

Figure 2.6: Ratio of total stopping power to water for several dosimetric materials. Source: NIST (ESTAR).

than silicon. In conclusion, it can be seen that Al_2O_3, though not as tissue equivalent as graphite or plastic, should be more appropriate than silicon, from a purely dosimetric point of view.

2.4.3 Cavity theory: size matters

A last parameter to take into account when studying the tissue equivalence of a detector is its size: indeed, a small detector will measure the absorbed dose resulting from interactions in its own material, but also in the neighboring medium. This is described by the "cavity theory". A detector introduced in water or in tissue is said to form a cavity in this medium. Cavity theory attempts to define the relationships between the absorbed dose recorded by the detector ($\overline{D}_{cav}$) and the absorbed dose in the unperturbed medium in the absence of the cavity (D_{med}). A general cavity theory for photon beams has been proposed by Burlin in 1966 (Burlin, 1966) and states that:

$$\frac{\overline{D}_{cav}}{D_{med}} = dS_{cav,med} + (1-d)(\frac{\mu_{en}}{\rho})_{cav,med} \tag{2.12}$$

where $S_{cav,med}$ is the ratio of mass collision stopping power of the medium to the cavity, and $(\frac{\mu_{en}}{\rho})_{cav,med}$ is the ratio of mass energy absorption coefficient of the medium to the cavity averaged over the photon spectrum. d is a weighting factor which describes the contribution to the total dose of electrons generated by photon interactions in the medium, and (1-d) is the contribution to the total dose from electrons generated in the cavity. If $d \rightarrow 1$, the equation approaches the Bragg-Gray conditions, and the cavity is said to be small. On the other hand, if $d \rightarrow 0$, the cavity is said to be large. Burlin made several approximations to permit the simple calculation of d (the attenuation of the electrons is exponential and the energy spectrum is not significantly changed by the presence of the cavity), and concluded that d could be expressed as:

$$d = \frac{1-\exp(-\beta g)}{\beta g} \tag{2.13}$$

where β is the effective mass absorption coefficient and g is a factor related to the size of the cavity. There have been many discussions in the literature about the correct formulations for g and β, and there is no general agreement (Burlin and Chan, 1969; Janssens et al., 1974; Paliwal and Almond, 1976). It was however noted (Mobit, 1996; Miljanic and Ranogajec-Komor, 1996) that the disagreement between those different formulations was less than 5%. Hence, for the simple purposes of this discussion (i.e., characterize where the size of the detectors position them in cavity theory) a simple approach will be used where g (the pathlength of the electrons crossing the cavity) is given by $g = 4\times$volume/surface area and β is given by

$$\exp(-\beta R) = 0.04 \tag{2.14}$$

This last formulation was suggested by Janssens et al. (1974), and R is the extrapolated range of the electrons crossing the cavity. The same analysis is used by Beddar et al. (1992b) in their work on plastic scintillators. Figure

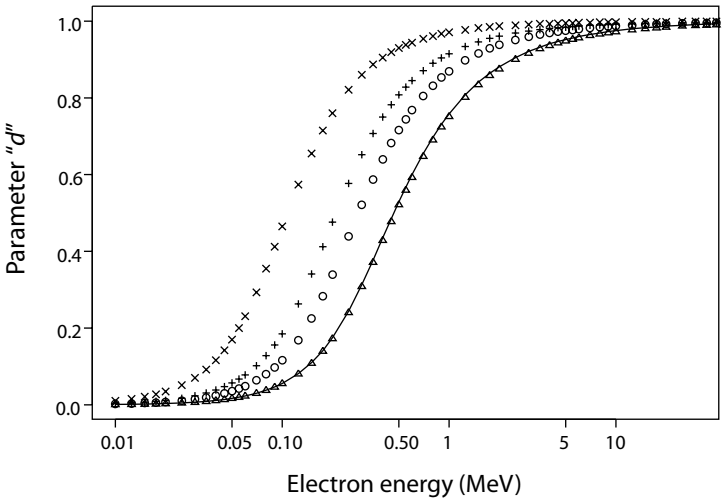

Figure 2.7: Parameter "d" from Burlin cavity theory versus electron energy for several dosimeter sizes. Circles: 0.5 mm ø x 2 mm ℓ. Triangles: 1 mm ø x 2 mm ℓ. + : 0.3 mm ø x 1 mm ℓ. X : 0.1 mm ø x 0.5 mm ℓ. The solid line represents the response of a plastic scintillator (1 mm ø x 4 mm ℓ).

2.7 shows parameter "d" as a function of electron energy for different dosimeter sizes, including a plastic scintillator (the smallest described by Beddar et al. (1992b), 1 mm ø x 4 mm ℓ). As can be seen, this scintillator has the same behavior in terms of cavity theory as the largest aluminum oxide crystal used in this work (0.5 mm ø x 2 mm ℓ). Small cylinders of aluminum oxide approach the small cavity approximation for radiotherapy energies (i.e., secondary electrons are generated in the medium outside the cavity), but will form a large cavity at diagnostic energies. Based on figure 2.7 and equation 2.12, the following deductions can be made:

1) at low energies, where the photoelectric predominates and the parameter d is low, the ratio D_{cav}/D_{med} is dominated by the strong dependence of the mass energy absorption coefficient on Z. Hence, $D_{cav}/D_{med} >> 1$ for aluminum oxide.

2) at high energies, the Compton effect predominates and μ_{en}/ρ does not vary much with Z. Moreover, the parameter d is larger and the final results depends mostly on the stopping power ratio. In this context, D_{cav}/D_{med} approaches 1 for aluminum oxide crystals.

This discussion gives some insight on the importance of the size of the detector, and its potential effect on its ability to estimate absorbed dose to water. At low energies (such as encountered in mammography), small changes in d can have a significant effect on the D_{cav}/D_{med} ratio because of the strong dependence on Z. Hence, for applications in mammography, it can crucial to optimize the size of the detector in order to minimize its variation in response with energy. In contrast, at radiotherapy energies, changing the size of the detector will not have as dramatic an impact on energy response. However, because of the increased requirement for accuracy in radiotherapy applications, even minor improvements in energy dependence could justify using smaller detectors.

2.5 Summary

The properties of RL and OSL from Al_2O_3:C crystals have been reviewed. The use of Al_2O_3:C in environmental and accident dosimetry means that a large body of literature is available, and theoretical models have been developed to predict the behavior of the OSL signal. This forms a solid basis for the investigation of the properties of Al_2O_3:C as a medical dosimeter. Some theoretical dosimetry considerations have been developed in this chapter to show that Al_2O_3:C crystals are suitable choice for *in vivo* radiation dosimetry. Of particular interest for the next chapters are the following conclusions:

- The luminescence produced by Al_2O_3:C crystals can be classified as: "prompt luminescence" or RL, and "luminescence under optical stimulation" or OSL
- RL and OSL signals are influenced by competing processes, due to the presence of deep and shallow traps in the crystalline structure: the OSL signal does not follow a purely exponential decay, and the RL signal exhibits an "afterglow" component
- Competition between RL and OSL traps gives rise to RL sensitivity changes during the irradiation: the RL signal presents a linearly increasing slope for exposure at a constant dose rate
- The decay of the luminescence-producing centers results in an emission at 420 nm and has an associated lifetime of 35 ms
- The relatively high effective atomic number of Al_2O_3 ($Z_{eff} \sim$ 10-11) is still lower than that of silicon diodes ($Z_{eff} \sim 14$)

- The small size of the crystals means that, at high energies, most of the secondary electrons are generated in the medium outside the cavity
- The optimization of the size of Al_2O_3:C crystals is crucial for applications at low energies

3 Instrumentation and methods

The RL/OSL optical fiber dosimeter system developed at Risø can be divided into three major components: i) a sensor crystal, ii) an optical detection system, and iii) the signal-processing electronics. The sensor Al_2O_3:C crystal is connected to the optical system via a plastic fiber. To produce OSL, a green laser beam is focused through a dichroic color beam splitter and transported via the optical fiber into the Al_2O_3:C dosimeter. The OSL signal is then transported back along the same fiber. The dosimeter system is controlled using a standard laptop computer (Andersen et al., 2003a). This configuration enables the system to be compact (40x30x10 cm^3) and transportable. This configuration uses only one optical fiber to reduce the size of the probe inserted into a patient for *in vivo* dosimetry. Figure 3.1 is a schematic illustration of the instrument, including the main electronic components. A photograph of the whole system is shown in figure 3.2.

This chapter describes in more detail the components of the system, as well as the analysis procedures developed to obtained reliable absorbed dose assessments from the RL and OSL signals.

3.1 Overview of the system

In all experiments performed in the present work, the RL and OSL signals were measured according to the protocol sketched in figure 3.3, using a 10 Hz sampling rate unless otherwise specified. As shown, the RL is collected during irradiation, while the OSL is measured by switching the laser on after the irradiation is completed. This approach allows the investigation of the respective properties of the RL and the OSL signals. Other protocols have been described by Polf et al. (2002) and Gaza et al. (2004), where the laser

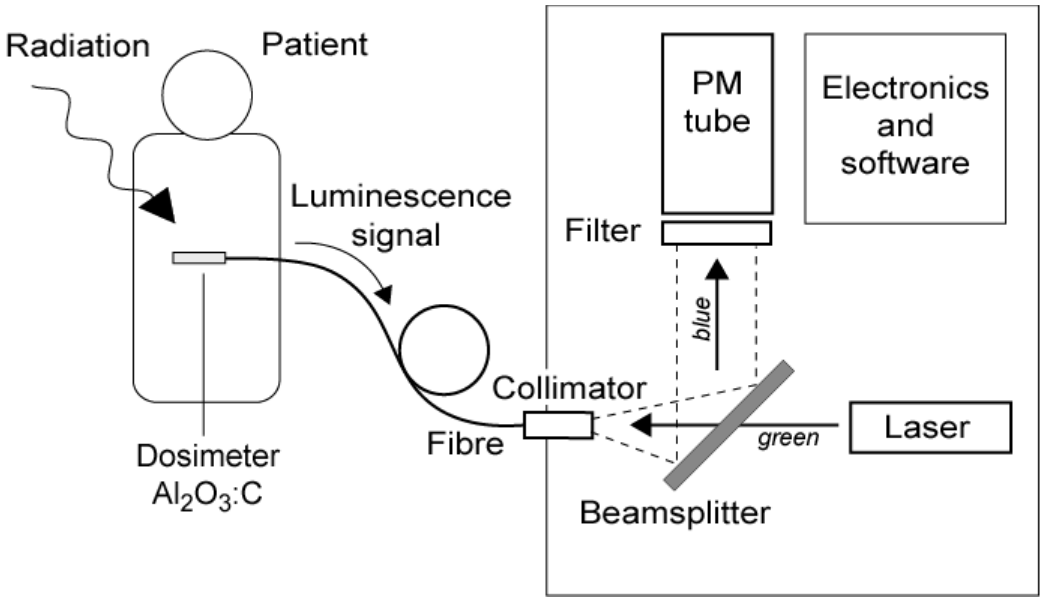

Figure 3.1: Schematic of the RL/OSL dosimetry system.

is switched on and off during the irradiation. However, this approach does not enable the use of the RL signal for dose assessment.

The RL/OSL dosimetry system is controlled from a laptop computer equipped with a Labview interface (National Instruments), as shown in figure 3.4. Two RL/OSL readers can be connected through a parallel interface and thus controlled by a single computer as seen in figure 3.2. From there, the laser can be switched on and off manually, or a program file can be created to keep the laser on in a specific time window. Data are stored as ASCII files and are later processed with the statistical software programme S-Plus (Insightful Corporation, Seattle, USA).

3.2 Optics and electronics

The signals generated in the Al_2O_3:C crystal are carried through the fiber to a fiber collimator which focuses the light onto a dichroic beam splitter. This dichroic beam splitter (Delta BSP 480) reflects more than 99% of the 390-425 nm bandwidth. This range includes the wavelength of the luminescence signals. From the beam splitter, the luminescence signal passes through a lens focusing the light through a filter pack consisting of three 3.5 mm thick band pass filters (BP25-395440 with band pass from 395-440 nm) and onto a Perkin-Elmer photomultiplier tube (CP-982). The PMT was selected

Figure 3.2: Photograph of the RL/OSL dosimetry system, showing a configuration where two measurement probes can be used simultaneously.

for its low dark count signal (3-5 counts per second) and almost constant response from 200 to 650 nm. To generate the OSL, a green laser (Laser2000, frequency doubled YAG laser, 532 nm, 20 mW) is transmitted through the beam splitter (transmitting 500-700 nm with more than 90% throughput) and coupled into the fiber dosimeter through the collimator. After interaction with the Al_2O_3:C crystal, the OSL signal is transmitted back through the fiber together with some of the laser light reflected from the fiber-crystal interface and from the facets of the crystal. The laser light reflected by the beam splitter is subsequently sufficiently reduced by the filter pack in front of the PMT. Thus, only luminescence is transmitted to the PMT. The filter combination was designed to yield a high signal to noise ratio (S/N) between the RL signal from the dosimeter Al_2O_3:C crystal and the noise signal generated in the fiber (see section 3.3.2). The whole system is made light-tight, thus preventing blinding of the PMT from ambient light sources and reducing the background noise level. A PC program made in Labview controls the system through a National Instruments 6036 PCMCIA card. The system is able to record data at 5 kHz sampling rate.

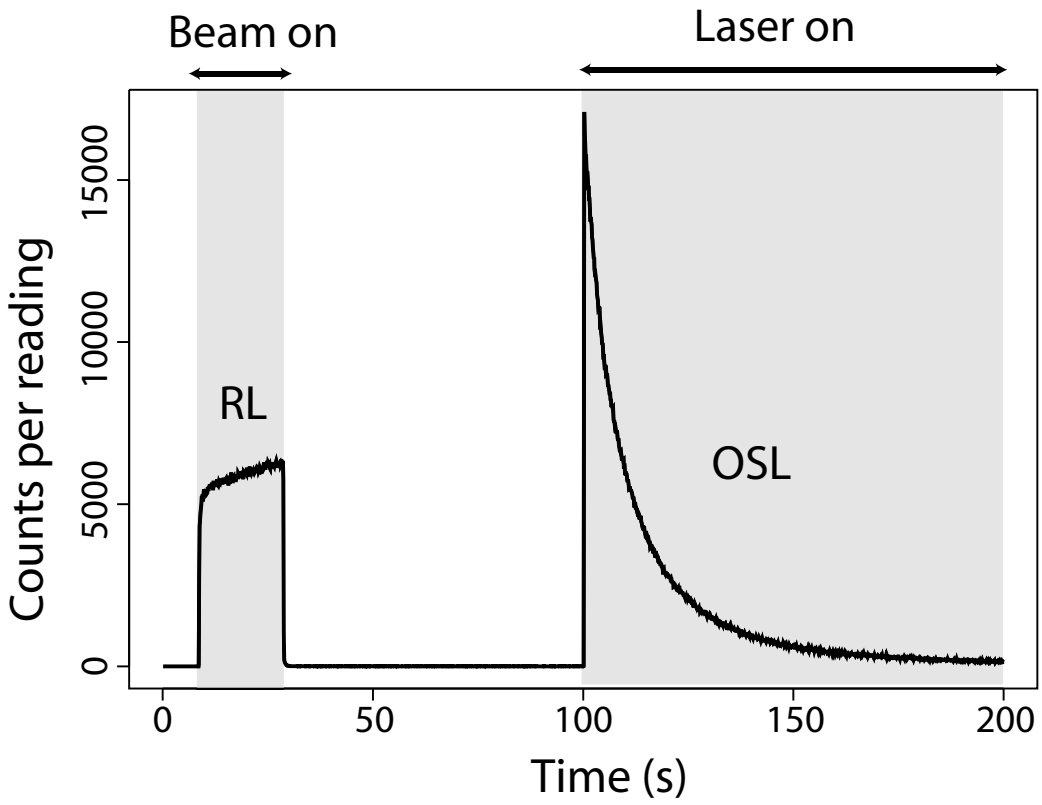

Figure 3.3: RL and OSL signals from Al_2O_3:C for an absorbed dose of 1 Gy.

3.3 The optical fibers

3.3.1 PMMA fibers

Most optical fiber dosimeters described in the literature use pure silica fibers (Beddar et al., 1992b; Huston et al., 2001). In this project however, it was decided to use plastic fibers (based on polymethylmethacrylate or PMMA) because of their increased flexibility and reduced cost compared to silica fibers. The PMMA fibers vary slightly depending on the size of the detector crystal considered. A description of every "fiber+crystal" assembly used in this project is given in table 3.1.

Super Eska SK-40 (Mitsubishi Rayon Co., LTD., Japan) optical fibers are made of a 1 mm PMMA core. The total diameter of the fibers, including cladding and jacket, is 2.2 mm (see figure 3.5). In the first probe prototype that was designed at the beginning of this project, no adhesive was used between the crystal and the fiber. Instead, the crystal was held close to the

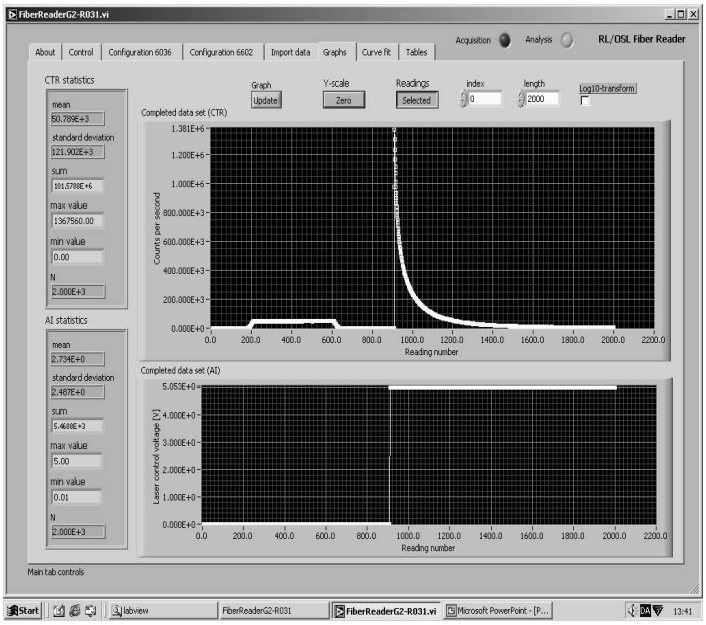

Figure 3.4: User interface of the RL/OSL dosimetry system.

Table 3.1: Fibers and crystals used in this work

Fiber number	Total diameter	Characteristics	Crystal origin	Crystal size (mm)	Adhesive
01	2.2 mm	Super Eska SK-40	pellet	1x1x2	none
43	2.2 mm	Super Eska SK-40	pellet	1x1x2	NOA 61
48	1 mm	GH-2001-P	growth 52	0.48 ø x 1 ℓ	NOA 61
49	1 mm	GH-2001-P	growth 52	0.48 ø x 1 ℓ	NOA 61
40B	2.2 mm	GH-4001-P	pellet	0.9x0.9x2.6	NOA 61
37	1 mm	GH-2001-P	growth 60	0.48 ø x 3 ℓ	NOA 61

fiber extremity by a “shrinkflex wrapping”. Though this method provided a satisfactory sensitivity, it resulted in a rather bulky probe (see figure 3.5). Hence, a new method was developed using NOA 61 as an UV curable optical adhesive (Polf et al., 2002; Marckmann et al., 2005). In order to protect the probe against the harsh hospital environment (tight bends in catheters and humid environment), a jacket made from Araldite is cast around the exposed crystal and fiber area. According to this technique, fiber 01 was reworked to become fiber 43 in August 2003. Similarly, new probes were developed using small crystals and GH-2001-P fibers (also from Mitsubishi Rayon Co., LTD.). The resulting probe has a total diameter of only 1 mm. In all fibers, the fiber end not connected to the crystal is fitted with an SMA fiber connector. The

choice of SMA connectors was made because FC connectors for multimode fibers with a core/cladding diameter above 125 μm were not available.

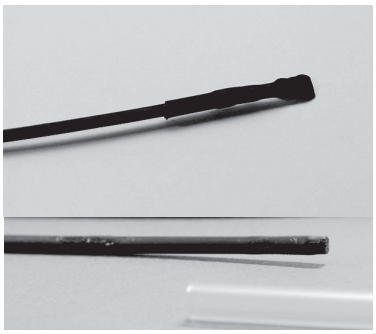

Figure 3.5: Photograph of the large RL/OSL fiber. Top: fiber 01, with shrinkflex wrapping. Bottom: fiber 43 using NOA 61 adhesive and an Araldite coating.

3.3.2 Signal coming from the light guide

The signal generated by ionizing radiation in the optical fiber during exposure introduces a noise component in all real-time measurements. Extensive literature attests to the presence of this so-called "stem-effect" in optical-fiber dosimeters using both plastic and silica fibers (de Boer et al., 1993; Clift et al., 2000). Beddar et al. (1992a) analyzed the effect of noise in plastic scintillator measurements (using pure silica fibers) and concluded that the main contributor was Cerenkov radiation. Cerenkov radiation is generated in a dielectric medium when a charged particle with a velocity greater than that of light in the medium is passing through the medium. The Cerenkov light is generated in an angle Θ defined as

$$\cos\Theta = \frac{1}{\beta n} \tag{3.1}$$

where β is the ratio of the charged particle velocity to the speed of light in the medium, and n is the refractive index of the medium. For the PMMA fibers used in this project, it has been shown that the main contribution to the stem effect is not from Cerenkov light, but from fluorescence (see (Marckmann et al., 2005) for more detail). As a result, the signal generated in the optical fiber is constant regardless of the angle of incidence of the radiation beam. In the case of the RL/OSL system, this signal will be present when the RL signal is collected. The OSL is collected after the irradiation is completed and is not affected by the noise signal from the fiber. Simple measurements were performed in a solid water phantom with fiber 43 to assess the order of

magnitude of the noise signal. For electron beams (from 6 to 22 MeV), the stem effect represents between 1 and 2% of the RL signal generated by this particular crystal. The effect is larger for photon beams, and can reach 4%. These estimates, however, are only valid for measurements in a conventional radiotherapy set-up, where the detector is positioned at the center of the beam. The impact of the stem effect turns out to be more critical for IMRT-type measurements. Indeed, due to the nature of an IMRT treatment plan, many small fields are used, "sweeping" over the target volume. Inevitably, there will be some instances where the detector lies outside the beam and only the fiber is irradiated. Consequently, the uncertainty on the dose estimate due to the presence of stem effect is likely to be much larger. Hence, it is crucial to discriminate the real RL signal from the noise signal if a reliable absorbed dose assessment is to be achieved. A method using temporal gating of the signals will be detailed in section 3.6.3.

3.4 Crystals

Three different Al_2O_3:C crystals were used in this work, as summarized in table 3.1. All crystals were manufactured by Landauer Inc, Chicago, USA and were grown according to the Stepanov method and Laser Heated Pedestal Growth (LHPG) method. The crystal in fibers 01 and 43 was cut from a standard Al_2O_3:C pellet (5 mm in diameter and 1 mm in thickness, used for environmental dosimetry at Risø) to obtain a 1x1x2 mm^3 crystal.

Smaller crystals were grown as a 0.48 mm diameter rod by Landauer Incèspecially for this project. This rod was referred to as growth #52 and was cut into 2 mm long segments, resulting in crystals #52-1 and #52-2. These crystals were annealed to 900 degrees Celsius, then exposed to a high dose of radiation (to fill all traps), and bleached with UV light (to free the dosimetric traps) before being used as dosimeters. As mentioned in chapter 2, different crystals have different luminescence characteristics. The signals from three fibers used in this project and simultaneously irradiated in a small beta source at Risø are displayed in figure 3.6. It can be observed that fiber 43 exhibits higher RL and OSL signals because of its larger crystal. In terms of luminescence signal per gram of crystal, however, fibers 48 and 49 are actually more sensitive. Fiber 43 also shows a slower OSL decay and experiences an increased RL sensitization compared to the other fibers. The apparent difference in sensitivity between fibers 48 and 49 is caused by differences in optical coupling or in the sensitivity of the photon counting systems.

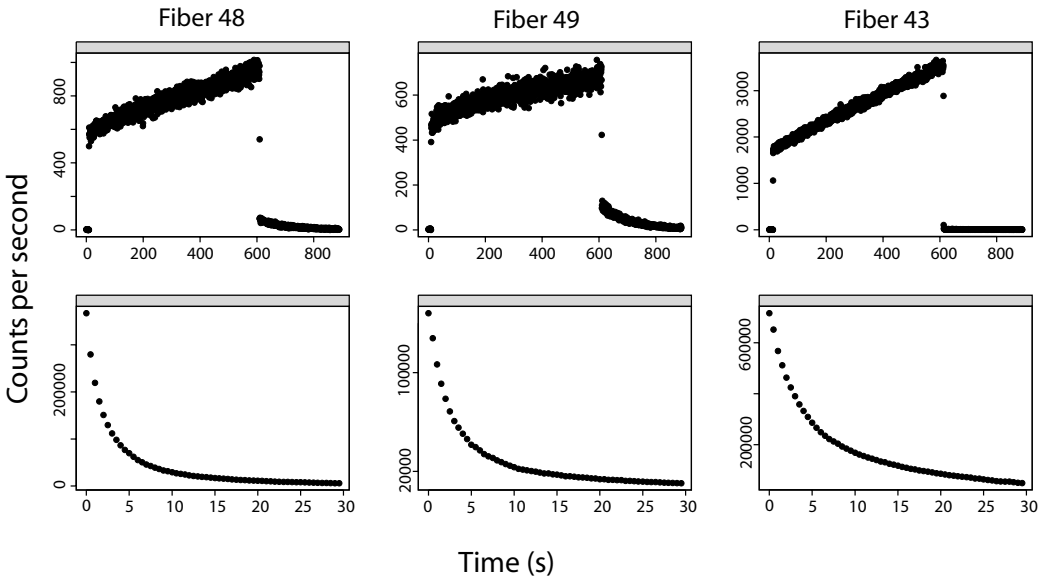

Figure 3.6: Signal from three different Al_2O_3:C fibers for an absorbed dose of approximately 2 Gy, delivered at 3 Gy/s: RL (top row) and OSL (bottom row). Fiber 43 exhibits the highest sensitivity, the most RL sensitization and the slowest OSL decay.

3.5 Analysis of the OSL signal

The depletion rate is a crucial parameter, since in theory all traps should be emptied in order to "reset" the OSL signal to zero and prepare the crystal for a new measurement. The dose absorbed by the detector is proportional to the intensity of the OSL signal and, in principle, a dose estimate can be obtained within a few seconds by reading the initial value of the OSL decay curve. However, for high precision, it is necessary to integrate the OSL decay curve and subtract the background noise caused by e.g. scattered laser light. Indeed, a dose estimate obtained by looking only at the "initial" value of the decay curve is susceptible to uncertainties due to variations of the laser output, for example. As a result, a long integration time could reduce the significance of these fluctuations and lead to increased precision of the dose estimate. On another hand, the influence of the competing (deep and shallow) traps increases with longer integration times. A compromise must be found between these two effects, and this can only come from experience with a specific crystal. Figures 3.7 and 3.8 illustrate this issue in the case of fiber 48. The crystal was irradiated in the small beta source and was exposed to five different doses between 0.5 and 4 Gy. This process was repeated 5 times. It can be observed that a significant improvement in the linearity of the dose response can be obtained by integrating the OSL signal for more

than 20 seconds. However, figure 3.7 indicates that the overall reproducibility of the dose assessment can be degraded by integrating for too long. As a compromise between these two competing effects, the OSL signal should be integrated for 100 seconds. This value was found to be optimal for all the crystals used in this work.

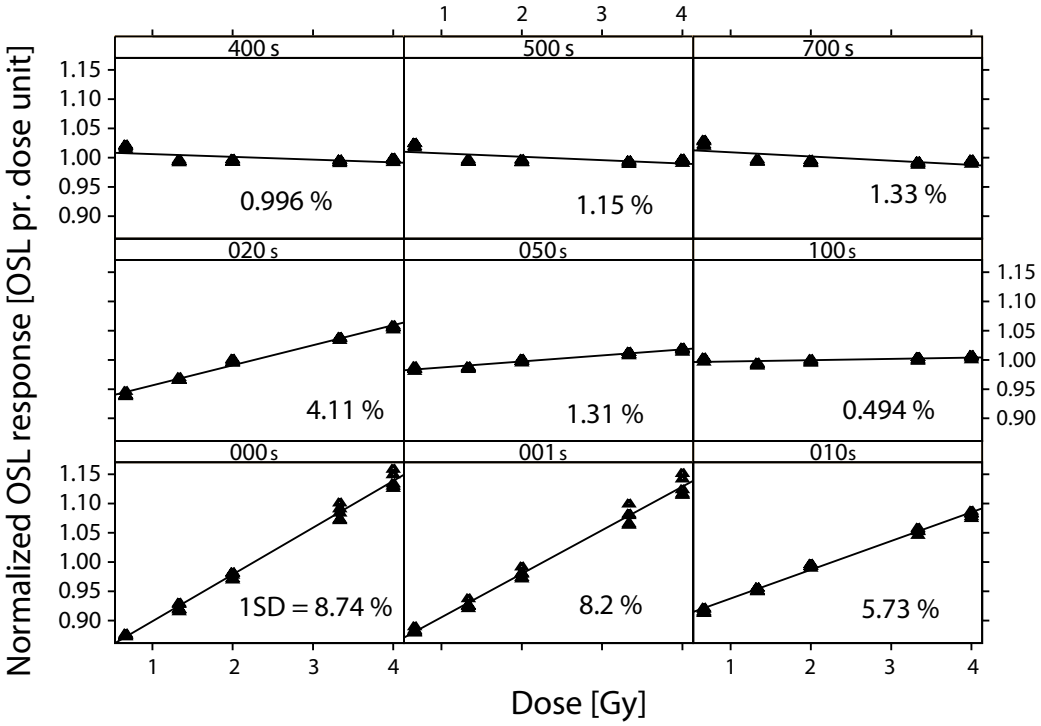

Figure 3.7: Reproducibility of the OSL response depending on the integration time. The OSL signal is integrated for durations ranging from 0s (using only the "initial" OSL reading) to 700 s, and the results are plotted as OSL response per dose unit (absorbed doses ranged from 0.7 to 4 Gy). The standard deviation of the results is given for each integration time. Integrating for 100 s gives the flattest response of the OSL signal per dose unit.

3.6 Analysis of the RL signal

Because the sensitization effect is the result of competition between RL and OSL traps, this initial RL sensitivity (i.e., the luminescence output per dose rate unit) will be reset every time the crystal is bleached (and the OSL traps are emptied). Since the crystal is reset between each measurement, the RL sensitivity at the start of the exposure is the same from one measurement to the next. Experimental data suggest that at the beginning of an irradiation, the instantaneous RL signal is directly proportional to the dose rate. An

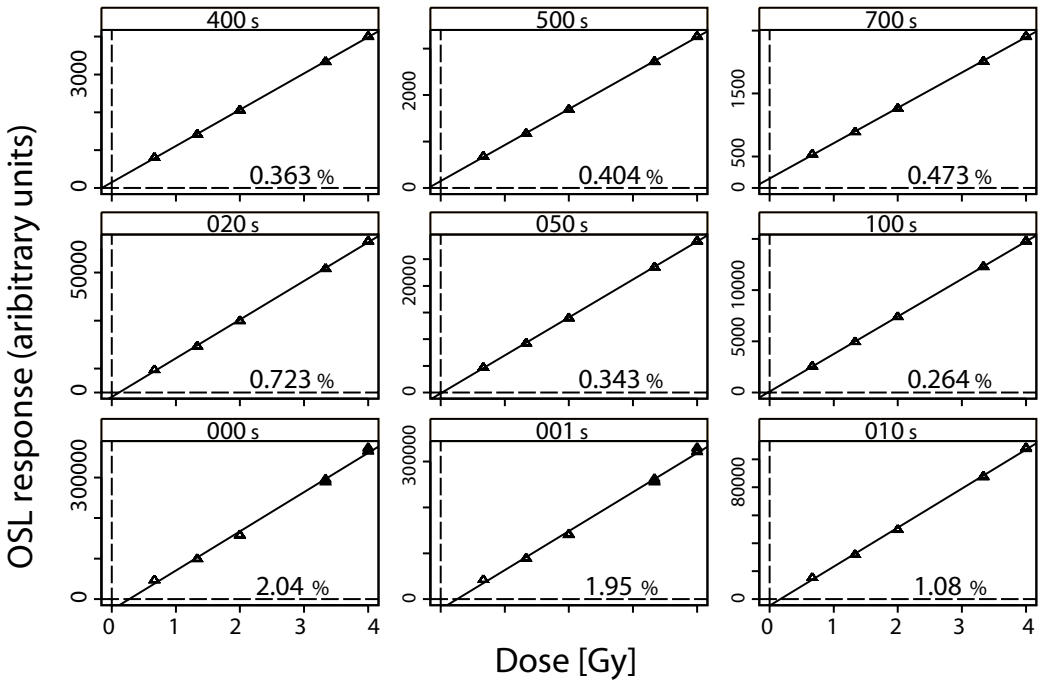

Figure 3.8: Linearity of the OSL response depending on the integration time. The OSL signal is integrated for durations ranging from 0s (using only the "initial" OSL reading) to 700 s. The standard deviation of the residuals from the linear fit divided by the maximum response is given for each integration time. Integrating for 100 s or more results in the most linear OSL response versus absorbed dose.

example for an irradiation in a 6 MV beam for a total absorbed dose of 1 Gy with dose rates varying from 2 to 6 Gy/min, is given in figure 3.9. These data also suggest that the sum of the RL signal depends only on the total absorbed dose, and not on the dose rate. Finally, the slope of the RL signal appears to be proportional to the square of the dose rate. For doses up to 1-3 Gy, the RL sensitivity changes are well described by a second order polynomial. For larger doses, a higher order polynomial is needed, and eventually a saturating exponential.

3.6.1 Dose assessment from the RL signal

A simple model can be developed to predict the behavior of the radioluminescence from one crystal. In the following model, we will assume that the RL sensitivity depends only on the absorbed dose D to the crystal. If the sensitivity β (in counts/Gy) is expressed as the count rate of the signal per dose rate unit then this assumption can be expressed as $\beta=\beta(D)$. If $\beta=\beta(D)$

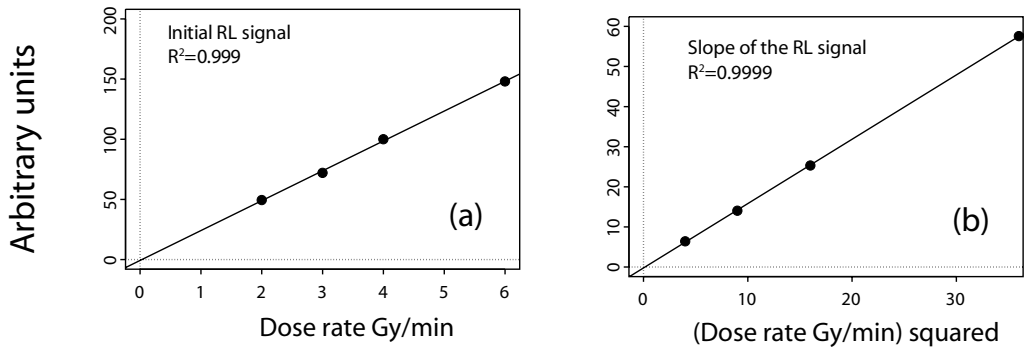

Figure 3.9: Sensitivity changes of the RL signal in a 6 MV beam (absorbed dose = 1 Gy): the initial RL signal increases linearly with the dose rate (a) and the rate of sensitivity changes ("slope") increases with the square of the dose rate (b).

and the dose rate is constant ($\dot{D} = \alpha$), then the luminescence output L (in counts) is the integral of the RL-signal from $t = 0$ to $t = T$.

$$L = \int_0^T \beta(D) \cdot \dot{D} \cdot dt \tag{3.2}$$

Since the dose rate is constant, equation 3.2 resolves into:

$$L = \alpha \cdot \int_0^T \beta(D) \cdot dt \tag{3.3}$$

Experimental data suggest that the sensitivity β is a polynomial function of the dose D: $\beta(D) = a + bD + cD^2 + ...$ It can then be shown that L is only a function of the absorbed dose D, $L = L(D)$. Since the total luminescence output does not vary with dose rate, the RL signal can be reliably use for dosimetry, and assessment of the total absorbed dose. Likewise, if the dose rate increases linearly with exposure time ($\dot{D}$=αt), it can be shown that $L = L(D)$. The implication, in two situations described above, is that when the same absorbed dose D is delivered with two different dose rates $\dot{D}_1$ and $\dot{D}_2$, the total luminescence outputs from the crystal will be equal: $L_1(D) = L_2(D)$. An experimental verification is shown in figure 3.10. It is however not possible to draw the same conclusion for any dose rate variation. Also, it does not necessarily result from the above that there is a proportionality between the total luminescence output and the absorbed dose, as in $L(D)/2 = L(D/2)$. Hence, the total sum of the RL signal can only be used in situations where the same absorbed D is delivered in different fashions.

Based on this model, the absorbed dose can be assessed from the RL signal in two ways. Firstly, the total sum of the RL counts can be considered. However, this method requires that the assumption β=$\beta(D)$ holds, and may

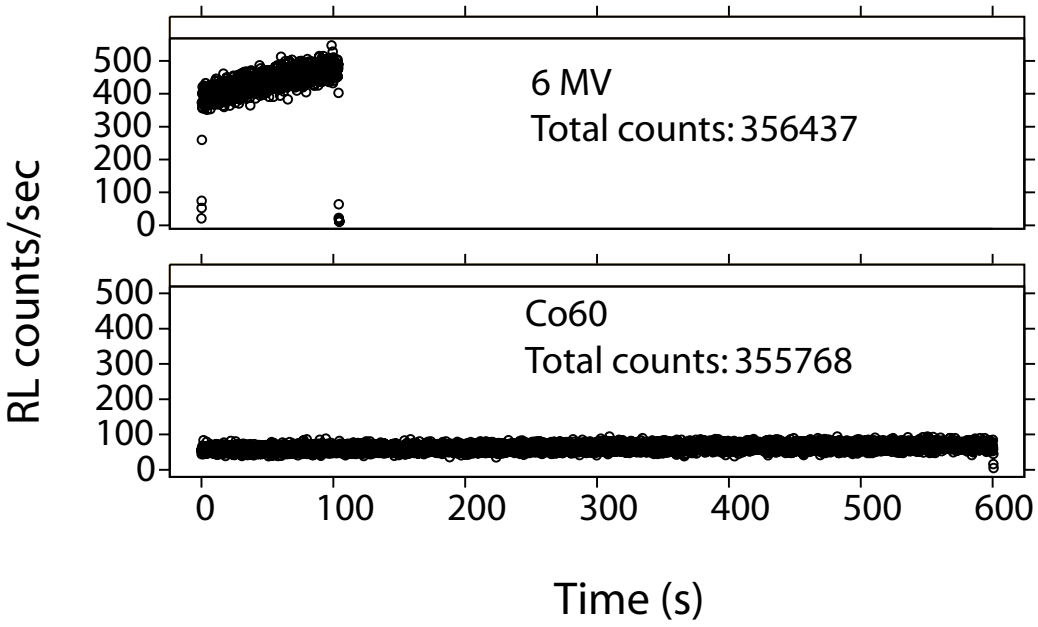

Figure 3.10: RL curves from exposure of the same Al_2O_3:C crystal to two sources: (a) 6 MV linac (dose rate =12 mGy/s), (b) Cobalt-60 source (dose rate = 2 mGy/s). The absorbed dose was 1 Gy in both cases. The difference in total RL counts is smaller than 0.2%.

result in some uncertainty on the dose estimate. Secondly, it is possible to consider only the first readings from the RL signal (which are directly proportional to the dose rate) and multiply this value by the duration of the exposure. This method will work well if there is no variation in dose rate at the beginning of the exposure. It has been observed that certain linacs take several seconds before the dose rate is stabilized (see figure 3.11). In this case, the "RL initial" method will lead to high uncertainties on the dose estimates. For a more reliable dose estimate, both methods are used and their results are compared.

3.6.2 Correcting for sensitization effects

Using the RL signal in its raw form (i.e., without correcting for sensitization or stem effects) does not enable a reliable assessment of the dose rate variations during the exposure. For this purpose, a correction algorithm was developed during the course of this project. This method consists in obtaining a reference curve of the sensitization effect.

The correction algorithm used is based on the following approach: if the sensitivity β is defined as the count rate of the signal per dose rate unit, then

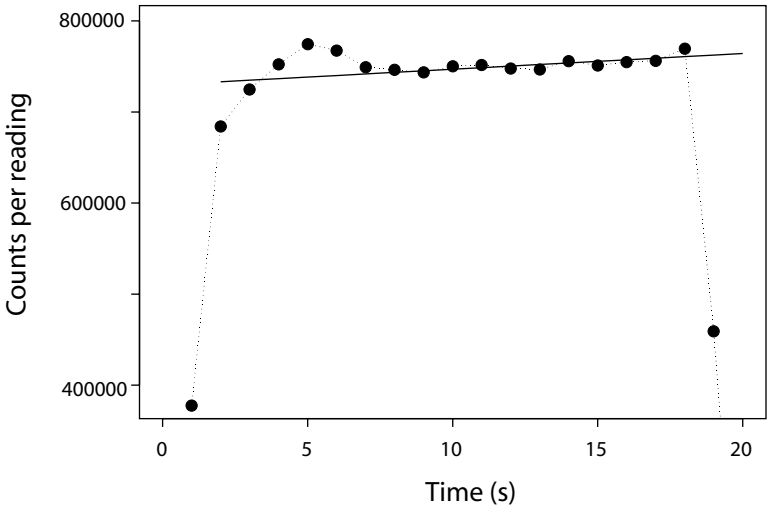

Figure 3.11: RL at the start up of a Varian clinac 2100: the instability of the dose rate delivered by the linac at the beginning of the exposure is clearly demonstrated and prevents the use of the "RL initial" method.

we have

$$\beta \cdot \frac{\Delta D}{\Delta t} = \frac{\Delta c}{\Delta t} \tag{3.4}$$

where Δt is the time resolution of the data acquisition (e.g., 0.1 s), Δc is the number counts and ΔD the dose increment during a period Δt. The calibration curve of the sensitization of a particular crystal, $\beta(D)$ is acquired by exposing the crystal to a relatively high dose of radiation (high enough to cover the range of doses that will need to be estimated). It is assumed that β depends only on the absorbed dose. With the crystal bleached to $D = 0$ before the experiments, the algorithm performs the following steps during the irradiation:

1. Estimate β at the present D from the calibration curve
2. Acquire reading $\Delta c/\Delta t$
3. Estimate dose increment according to $\Delta D = \Delta c/\beta$
4. Update dose $D \leftarrow D + \Delta D$
5. Repeat from step 1

An illustration of the sensitization correction algorithm is shown in figure 3.12. Figure 3.13 shows the use of the corrected RL signal to resolve a depth dose distribution in water. Such an experiment is a valid test of the sensitization algorithm since the dose rate varies with the depth of the detector

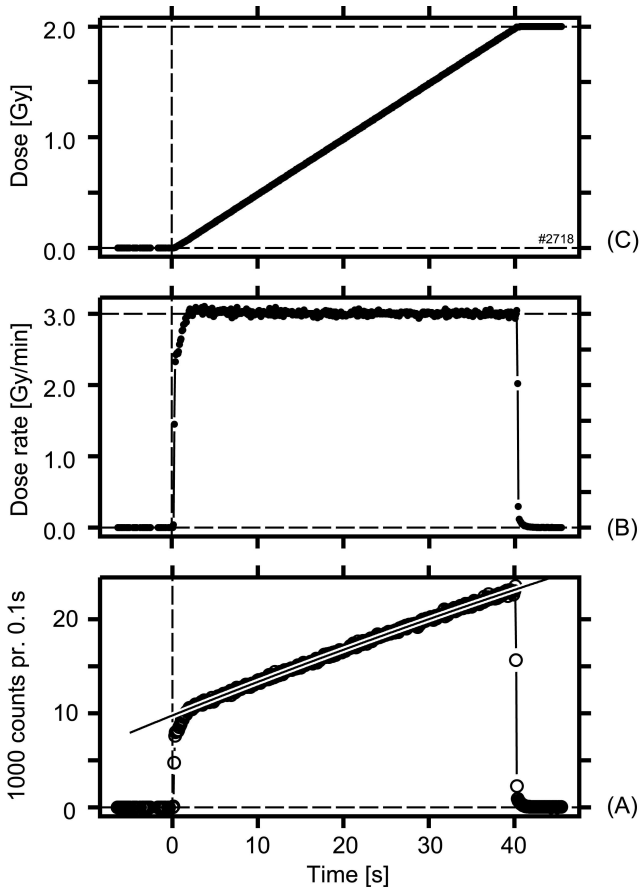

Figure 3.12: An example of the RL sensitization correction algorithm for dose of 2 Gy, delivered at 3 Gy/min with 6 MV photons. (a) shows the raw RL signal during the irradiation and the fitted calibration curve. (b) and (c) show the estimated dose rate (from the corrected RL signal) and the accumulated dose, respectively.

in the water phantom, and 15 data points (resulting in accumulated dose of 2-3 Gy) were acquired without resetting the crystal with laser light between measurements. The experiment was repeated three times. As can be seen, the RL data agree with reference data within 0.5% except at shallow depths, where positioning uncertainties are considerable. This example validates the sensitization correction algorithm and the reliability of the RL signal for dose rate and absorbed dose assessment.

3.6.3 Getting rid of the stem-effect: time gating

It is not possible to filter the stem effect out optically since its emission band overlaps with the RL signal (Marckmann et al., 2005). Temporal methods,

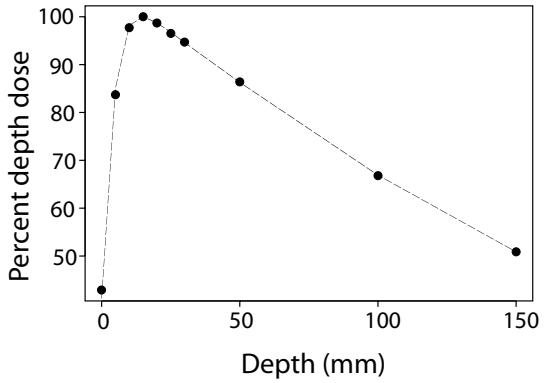

Depth mm	Reference %	RL estimate %		
		Mean	Std. dev	N
0	41.1	42.9	1.9	3
5	85.1	83.7	2.2	3
10	98.2	97.7	0.3	5
15	100.0	100.0	0.1	3
20	**98.7**	**98.7**	0.5	3
25	**96.8**	**96.5**	0.2	3
30	**94.6**	**94.7**	0.4	6
50	**86.3**	**86.4**	0.3	6
100	**66.9**	**66.8**	0.1	6
150	**50.9**	**50.9**	0.2	6

Figure 3.13: Test of the sensitization correction algorithm. A depth dose distribution was acquired using only the RL signal, without resetting the crystal with laser light between measurements. RL data agree closely with reference data (obtained with diodes) and demonstrate the validity of the correction algorithm.

involving other detectors, have been reported by Jordan (1996) and Justus et al. (2004) and take advantage of the different lifetimes of the signals. Radioluminescence in Al_2O_3:C primarily originates from direct recombination through the F-centers (see chapter 2), and this process involves a relaxation time of 35 ms. As a result, the main part of the RL signal is delayed relative to the irradiation. In contrast, fluorescence or Cerenkov light generated in the optical fiber has a lifetime of the order of a few picoseconds: this signal will only be present during the irradiation. Linear accelerators are pulsed radiation sources (usually delivering a 4 μs pulse every 2.6 ms). Thus, it is possible to separate the RL signal from the stem effect signal by measuring the RL in between the beam pulses.

A simple electronic circuit was developed to implement this temporal gating, using the synchronization signal from the linear accelerator (which typically triggers single 12-35 μs pulses). These pulses are used to block counting during and immediately after every beam pulse. The blocking can be made by gating the input to the counter. This system is illustrated in figure 3.14 (for more detail, see (Andersen et al., 2005)). Experiments testing the validity of this temporal gating method are presented in chapter 5.

3.7 Summary

- The RL/OSL dosimetry system can control two optical fiber probes from the same laptop interface.

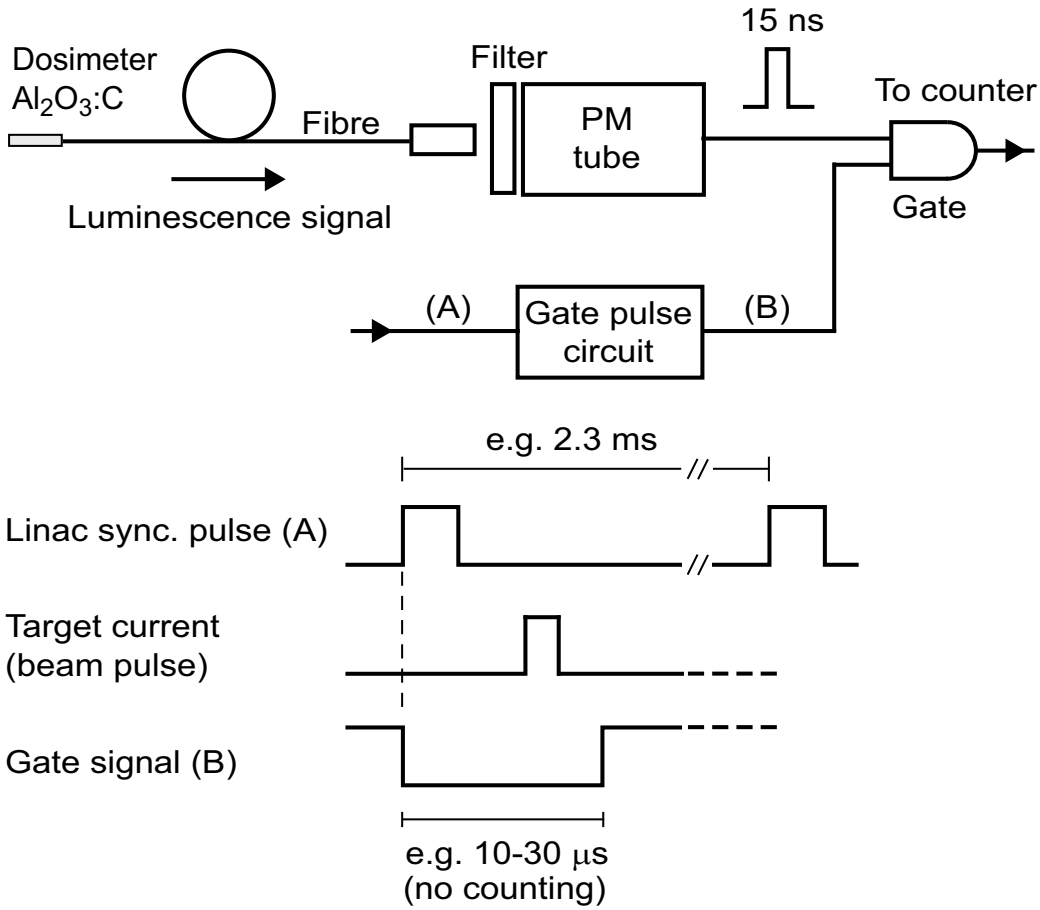

Figure 3.14: Temporal gating for acquisition of the RL signal.

- During the course of the project, considerable improvement has been made regarding the design of the probes, leading to a better coupling between the crystal and the optical fiber.
- Absorbed dose assessment from the OSL signal is made by integrating the OSL decay curve for 100s (which was found to be the optimal integration time for the fibers used in this project).
- The RL signal is subject to changes in sensitivity and to noise in the form of light generated in the optical fiber during irradiation (stem effect).
- Absorbed dose assessment from the uncorrected RL signal can be performed by using the integrated RL signal or the first readings of the RL signal only.

- Corrections algorithms developed during the course of the project enable to correct the RL signal for sensitivity changes and stem effects.

4 Basic dosimetry parameters for radiotherapy

The basic characteristics and dependencies on beam parameters of the RL/OSL dosimetry system were first tested in radiation sources at Risø National Laboratory. In this configuration, it is possible to fully automate the experiment: for example, both the RL/OSL dosimetry system and a small beta source can be controlled from the Labview interface. Hence, it is possible to launch two days of measurements without operator intervention. Since at present, every measurement takes between 15 and 20 minutes (because of the bleaching procedure), this is a valuable gain of time. However, these measurements are performed in air and in irradiation conditions very different from a clinical treatment. Therefore, measurements were repeated in a hospital environment, where radiotherapy beams and phantoms were available. However, due to the limited access to clinical beams, fewer data points are available. For this reason, whenever relevant, laboratory and hospital measurements are presented together in this chapter. In light of these experiments, the sources of variability (from the RL/OSL reader, from the crystal, or from the experimental set-up) are discussed.

4.1 Additional equipment and set-up

Laboratory experiments were performed at Risø and involved three types of radiation sources:

1. a 1.486 Bq (40 mCi) beta source in a lead casing (^{90}Sr/^{90}Y, average energy of emitted electrons: 0.196 MeV)

2. a mini x-ray generator from Varian (50 keV, 1 mA) (Andersen et al., 2003b)

3. a calibrated gamma irradiation facility, including Cobalt-60 and Cesium-137 sources with activities of 10 mCi and 8 mCi respectively.

These sources offer flexibility in the range of dose and dose rates for testing the performance of the RL/OSL dosimeter. However, parameters like field size, or distance from the source are not always adjustable. Since these sources have a constant output, the dose delivered to the detector can be expressed in seconds of irradiation.

Clinical measurements were performed at Malmö University Hospital (UMAS) and Copenhagen University Hospital (Rigshospitalet). The clinical beams included photon beams with energies ranging from 6 to 18 MV, and electrons beams from 6 to 22 MeV. The linear accelerators were either from Varian (type Varian Clinac 2300 or 2100, Varian Medical Systems, Palo Alto, USA), or Elekta (type Elekta SLi plus, Elekta AB, Stockholm, Sweden). The measurements were performed either in water, or, when convenient, in an epoxy resin-based mixture called "solid water" (available from Gammex-RMI, Inc. Middelton, USA). Solid water has the same density (1.00 g/cm^3) and electronic density (3.34 x10^{23} electrons per gram) as water and is widely used in radiation therapy dosimetry. Figure 4.1 illustrates a simple set-up of the dosimeter in a solid water phantom, as well as the different parameters used to commonly characterize a specific beam configuration in radiotherapy. The output of the linear accelerator is expressed in monitor units or "MU". This parameter basically reflects the irradiation time but also takes into account the small variations in output that can occur due to power fluctuations. Linear accelerators are usually calibrated to give 1Gy/100MU at a specific location (e.g, at 100 cm SSD and 1.5 cm depth for a 6 MV beam using a 10 cm x 10 cm field).

All the data in this chapter (unless otherwise specified) have been acquired early in this project, where only fiber 01 was available, and no sensitization correction or time-gating algorithm was developed. Nonetheless, these measurements offer insight on the characteristics of the "raw" RL and OSL signals, and provide a good base for understanding the challenges of accurate dose assessment from these signals. According to the data analysis protocol described in chapter 3, the analysis of the RL signal will be made using only the first readings (to avoid overestimates due to the sensitization effect). The OSL signals were integrated for 100 s to provide the most reliable absorbed dose estimate.

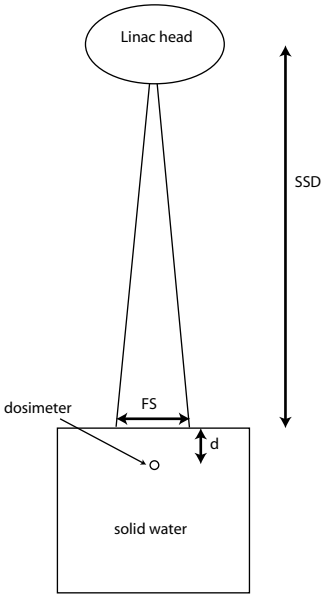

Figure 4.1: Set up for radiotherapy experiments. Parameters illustrated are the source-to-surface distance (SSD), field size (FS), and depth (d).

4.2 Reproducibility

The stability in response of the RL/OSL dosimetry system was first tested using the mini x-ray source at Risø. A fixed absorbed dose (500 s irradiation at 50 kV and 0.3 mA, ∼0.5 Gy) was delivered 66 times to fiber 01, and the crystal was bleached for 20 minutes after each irradiation. The results are presented in figure 4.2. For the OSL signal, all data points are well within ± 0.5%, with a standard deviation of 0.1%. These results include variations due to the output of the x-ray tube and show that the system has an excellent short-term reproducibility. They also demonstrate that the crystal can be regenerated as part of the measurement procedure.

The standard deviation for the RL response is 0.6% over 66 measurement points but RL results for this crystal present a upward trend. The cause of this trend is not well understood, but hypotheses include temperature variations in the laboratory facilities and a deep-trap effect, which would affect mostly the RL signal. The impact of this trend is limited if frequent calibrations are made, as is the case in all the experiments presented in this work.

The reproducibility was also tested in clinical photon beams of 6 MV and 18 MV in a water tank positioned at 100 cm SSD. The beam settings were: 10x10 cm^2 field, 1 Gy delivered at 3 Gy/min, with the detector positioned at

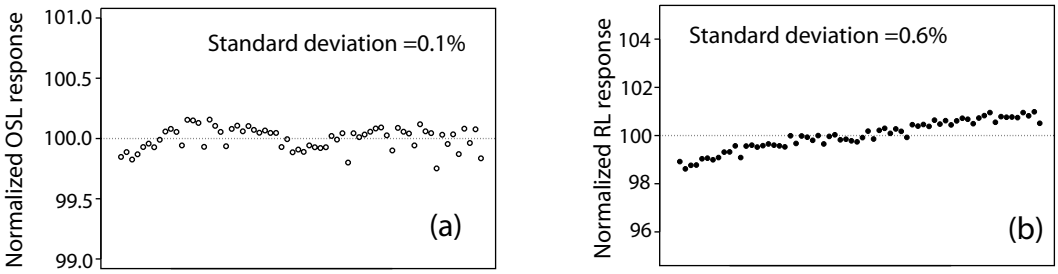

Figure 4.2: Reproducibility of the RL/OSL system in laboratory conditions: OSL (a) and RL (b) responses for 66 consecutive measurements.

depth dose maximum. Beams from this linear accelerator were reported to be stable (within 0.3% for the 6 MV beam and 0.7% for the 18 MV beam) for the month preceding this experiment. Measurements were repeated 10 times in the 6 MV beam and 8 times in the 18 MV beam. The initial "peak" of the OSL signal is reproducible with a standard deviation of 0.9% in the 18 MV beam (1.5% at 6 MV). The integrated OSL signal, however, has a reproducibility of 0.4% (0.7% for 6 MV, 1SD). This indicates the possibility of small fluctuations in the laser output. Figure 4.3 shows the RL signal, the first 5 seconds of the OSL signal, and the background signal after 400 seconds of bleaching for the 10 experiments. The initial readings of the RL signal (before any sensitization occurs) show a standard deviation of 0.8% (in both beams). The sum of the RL signals is here reproducible with a standard deviation of 0.5% (in both beams). It should be noted that the variation of the RL results in this experiment is random, which confirms a good short reproducibility of the RL signal.

4.3 Linearity and dose rate response

The linearity of the dose response of the RL/OSL dosimeter was investigated using the ^{90}Sr source at Risø. This source has a low dose rate and can deliver accurate doses of the order of 1 mGy. Results are presented in figure 4.4 and show that the dose response of the OSL signal is linear from a few mGy to 3Gy (R^2 >0.999).

The measurement of absorbed dose from a detector intended for use in clinical dosimetry has to be independent of variations in the dose rate. Dose rate measurements were performed using the ^{60}Co and ^{137}Cs gamma sources at Risø, because of the possibility to increase the source-to-detector distance (in air) and thereby obtain very low dose rates. The results are illustrated in figure 4.5. It is clear from figure 4.5 that the instantaneous RL signal

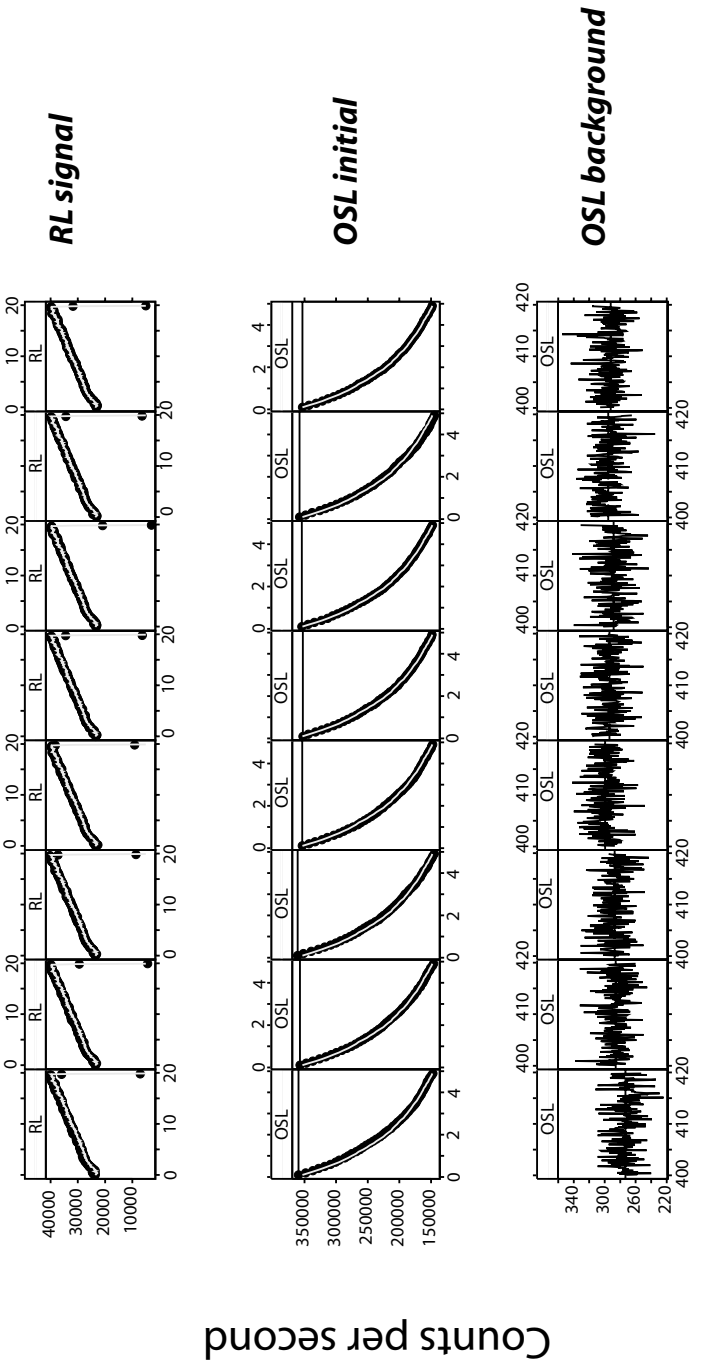

Figure 4.3: Reproducibility of signals in a 18 MV clinical beam. Results from 8 consecutive measurements are presented, showing the RL signal, the first 4 seconds of the OSL signal, as well as the background signal obtained after 400 s of bleaching.

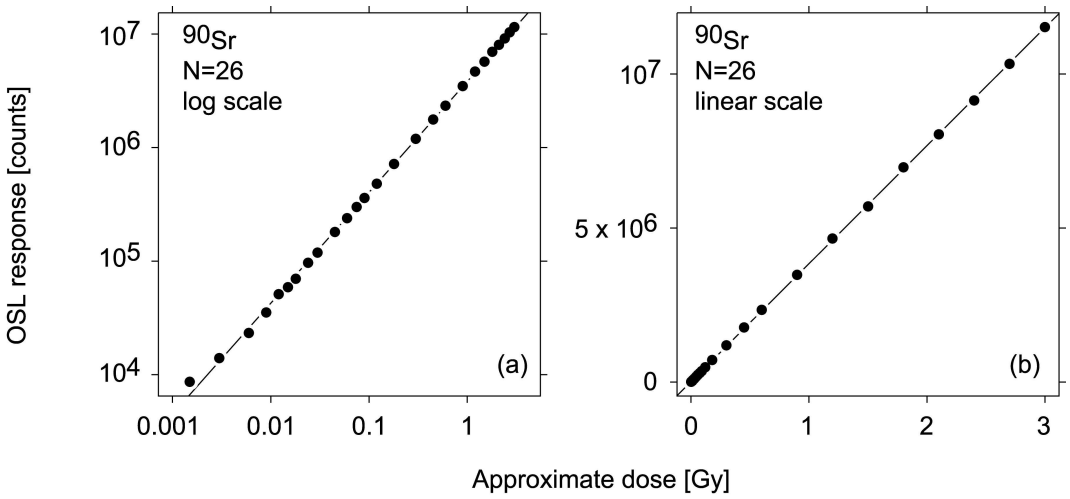

Figure 4.4: OSL signal versus absorbed dose: results are presented in log scale (a) and linear scale (b).

(as estimated from the first readings) increases linearly with dose rate if no sensitization effect is present. However, the integrated RL signal (without sensitization effect) should be proportional only to the total absorbed dose and independent of dose rate.

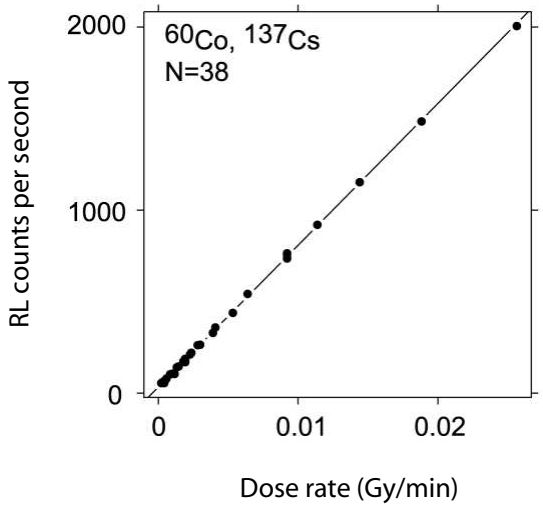

Figure 4.5: OSL signal versus dose rate in ^{60}Co and ^{137}Cs gamma sources

The response of the RL/OSL dosimeter was investigated in a water tank irradiated with a 6 MV photon beam (10x10 cm^2, 100 cm SSD). The RL/OSL detector was positioned at 5 cm depth in the water, and 100 MU ("monitor units", corresponding to 0.85 Gy at the point of measurement) were repeat-

edly delivered using different values of the pulse rate of the linear accelerator (0.85-5.1 Gy/min, or 100-600 MU/min). It should be noted that in this experiment, the instantaneous dose rate is not actually varied, but rather the number of dose pulses delivered by the accelerator in a certain amount of time. However, the response of the dosimeter to pulse rate is of clinical interest, and the term "dose rate" is often used instead of "pulse rate". In figure 4.6, the OSL signal normalized to the average of all measurements is plotted versus the pulse rate, and the variation is 0.3% (1 SD) for the range of pulse rates included in this investigation. Figure 4.6 also shows the excellent linear relationship between the amplitude of the initial RL signal and the dose (pulse) rate (R^2=0.9999).

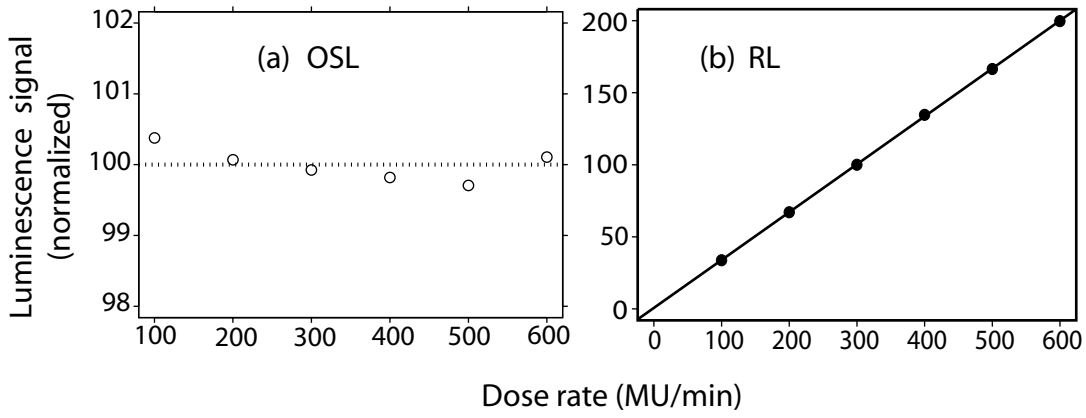

Figure 4.6: Dose rate response of the RL/OSL system in a 6 MV beam: (a) normalized OSL results; (b) Initial RL signal versus dose rate (here, pulse rate).

4.4 Energy dependence

As mentioned in chapter 2, Al_2O_3:C has an atomic number higher than water (10 vs 7). Therefore, the RL/OSL detector will show some energy dependence, i.e. the output signal from the detector might vary with the radiation quality used. In all the following measurements, the absorbed dose was determined using an ionization chamber calibrated in terms of absorbed-dose-to-water at the Swedish secondary standard dosimetry laboratory. The readings were normalized to the average of the RL or OSL signals for all measurements. Figure 4.7 shows the variation of the signal found when an absorbed dose of 2 Gy is delivered to the position of the detector at a depth of 10 cm in water, using 6 MV and 18 MV photons from an Elekta linac. The variation in output from the detector was 0.6% (1 SD) for both RL and

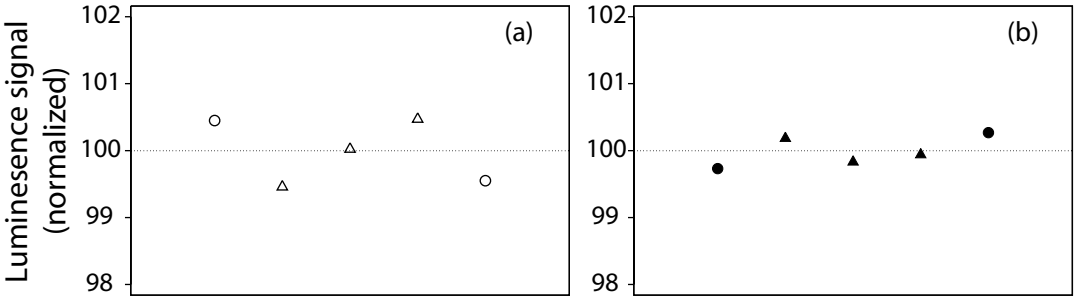

Figure 4.7: Energy dependence of the RL/OSL dosimeter in 6 MV (circles) and 18 MV (triangles) photon beams. (a) OSL results, (b) RL results.

OSL signals. This is acceptable for clinical purposes, although for greater accuracy, some correction factors could be determined. Additionally, some measurements were performed in water comparing gamma rays from a Cobalt source (with an energy of approximately 1.25 MeV) and 6 MV photons. The results from the OSL readings, normalized to ion chamber measurements, show a deviation of 2.3% between the average response to Cobalt and to 6 MV (see figure 4.8).

Theoretical calculations from Monte Carlo simulations were performed by L Buckley and DWO Rogers at Carleton University (Ottawa, Canada). These simulations were based on the code EGSnrc (Kawrakov and Rogers, 2000), including a new correlated sampling algorithm (Buckley et al., 2004a) and were based on the large Al_2O_3:C probe from Risø (fiber 01). The results show that an energy dependence of about 3% is expected between ^{60}Co and 18 MV (Buckley et al., 2004b), but that this variation in response should be less than 1% between 6 and 18 MV beams. This estimate is in agreement with experimental RL/OSL results. As mentioned in chapter 2, the energy dependence of the probes should decrease for smaller crystals.

4.5 Angular dependence

A dosimetry system is usually calibrated in a set-up such as described in figure 4.1 where the gantry is not rotated ("0 degree angle" set-up). However, *in vivo* measurements are often performed with a rotated gantry. Hence the variation in response of the RL/OSL system with respect to the angle of incidence of the beam is an important parameter. The angular dependence was investigated only in hospital conditions. The detector was positioned in the center of a spherical and hollow glass phantom, filled with water. The diameter of the sphere was 3 cm, enough to provide build-up for a

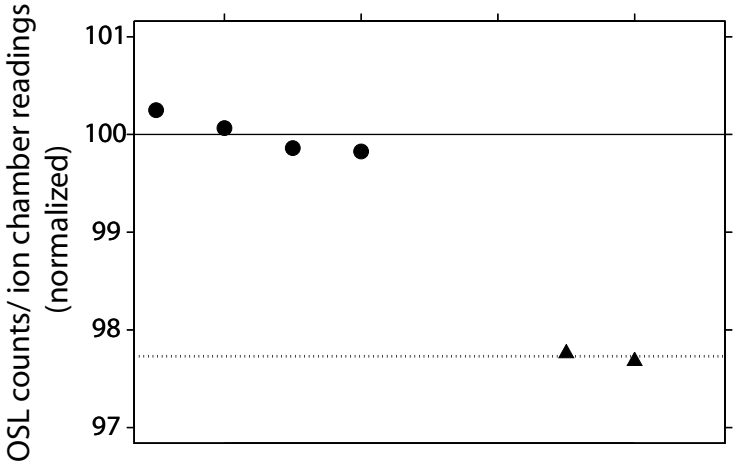

Figure 4.8: Energy dependence between ^{60}Co (circles) and 6 MV (triangles). OSL results are presented and are normalized by ionization chamber readings. The solid and dotted lines represent the average values of OSL response for ^{60}Co and 6 MV, respectively.

6 MV photon beam. The Al_2O_3:C detector was positioned at the beam isocenter. At a gantry angle of 0 degree, the optical fiber was placed along the central axis of the beam in the position illustrated in figure 4.9. In order to minimize the effects of a potential set-up error, data from 0 to 179 degrees are normalized to the value at 90 degrees, while data from 180 to 360 degrees are normalized to the value at 270 degrees. The OSL and the RL signals were found to have standard deviations of 1.3% and 1.7% respectively.

4.6 Crystal temperature

The temperature dependence of the system was only tested in laboratory conditions. The response of the dosimetry system should not vary with crystal temperature, as measurements can be performed at room temperature (18-22℃) or at body temperature (35-40 ℃). The RL/OSL dosimeter was tested at a variety of ambient temperatures ranging from 0 to 45℃. This experiment was performed with fiber 40B. The results are included in figure 4.10. The standard deviation of the results over the range of temperature studied is 1.3% for long integration times ($\geq$100s). However, it should be noted that the temperature dependence of the OSL signal increases if short integration times are used because of the slow depletion of shallow traps at low temperatures. This effect is illustrated in figure 4.11. Hence, an integration time over 100 s is recommended to minimize the temperature dependence of the

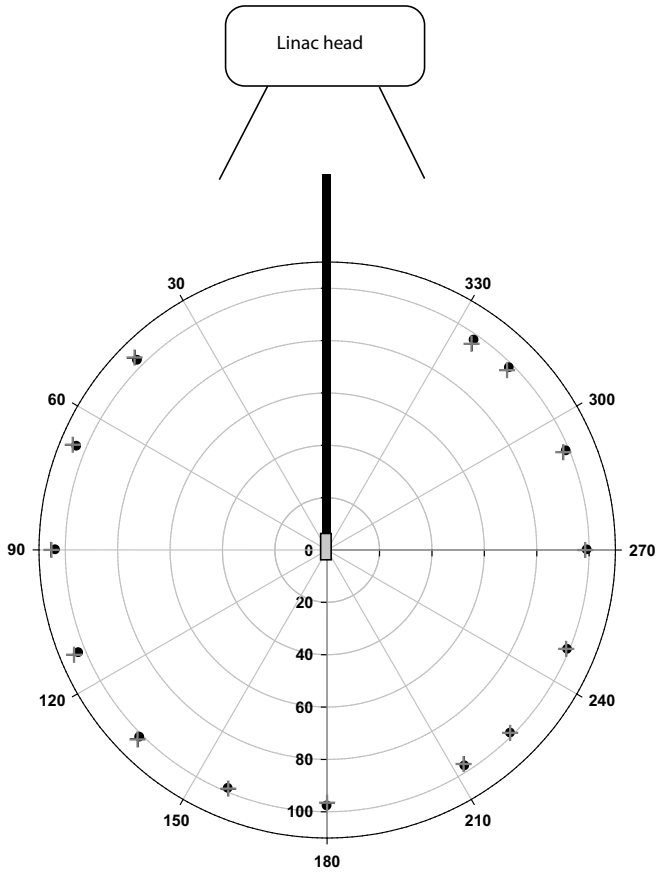

Figure 4.9: RL/OSL responses versus the angle of incidence of the beam. Black circles: OSL, Grey crosses: RL. The fiber was positioned along a vertical, downward axis

OSL response. The RL signal does not seem to be affected by temperature to the same degree (see 4.12). However, the afterglow following the end of the irradiation (see 2.3) exhibit a higher decay rate with increasing temperatures. Indeed, the decay rate of shallow traps is determined by the ambient temperature, and will thus increase with high temperatures.

4.7 Depth dose distributions

It is important from a clinical point-of-view to evaluate the ability of a new dosimeter to resolve depth-dose distributions, as it illustrates the behavior of the detector at depth, where it is exposed to slightly different beam spectra. In the following investigation, RL/OSL data have been compared

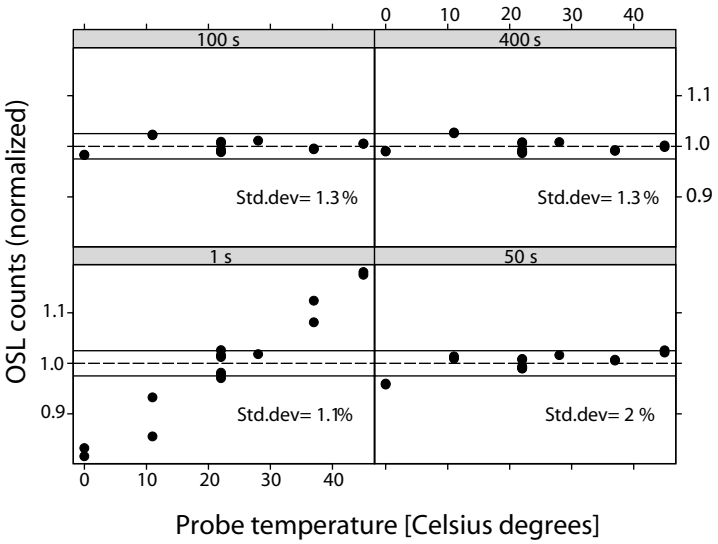

Figure 4.10: OSL response of the probe at different temperatures: the variation in response can be minimized if a long integration time is used.

to the results obtained with a commercial p-doped Si-diode detector (Scanditronix/Wellhöfer, Uppsala, Sweden). Figure 4.13 shows depth-dose distributions in water obtained at UMAS with 6 MV and 18 MV beams respectively, using a 10x10 cm^2 field set at 300 MU/min, corresponding to 3 Gy/min at the depth-dose maximum. All data have been normalized to the depth-dose maximum. On figure 4.13, it can be observed that the largest discrepancy between diode and RL/OSL data occurs at shallow depths. This can be explained partly by the positioning uncertainty in a high-dose gradient as well as by the under-response of diodes at shallow depth (Heydarian et al., 1996). Beyond the build-up region, the agreement between diode and RL/OSL data is 1% (1SD). Depth dose distributions from electrons beams (6,12 and 22 MeV) are presented in figure 4.7. The agreement between RL/OSL and diode data is within 1.1% for 6 MeV and 0.9% for 22 MeV (1SD). Absolute deviations between the diode data and the RL/OSL data are larger for 6 MeV, possibly because of the sharper dose gradients. Discrepancies between RL and OSL results can also be observed and are probably due to the the way the RL analysis is performed (using the sum of the uncorrected RL signal, see chapter 3).

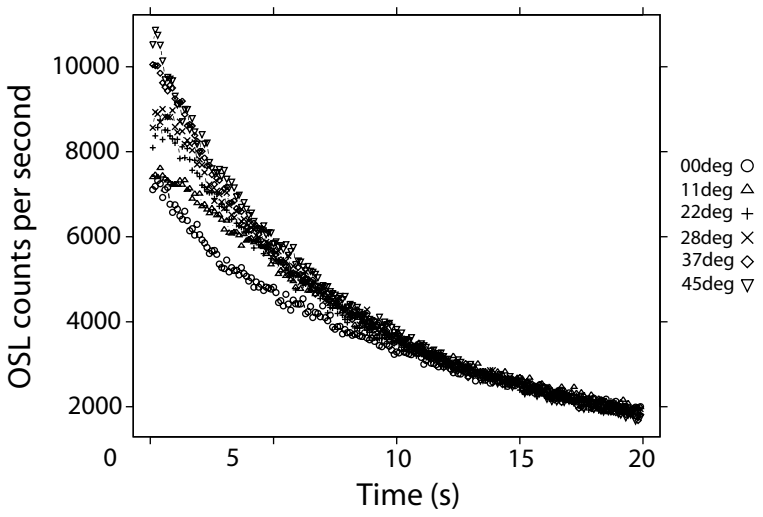

Figure 4.11: OSL response of the probe at different temperatures. The height of the initial signal varies with temperature, but the effect fades after a couple of seconds, suggesting a faster depletion of shallow traps at higher temperatures.

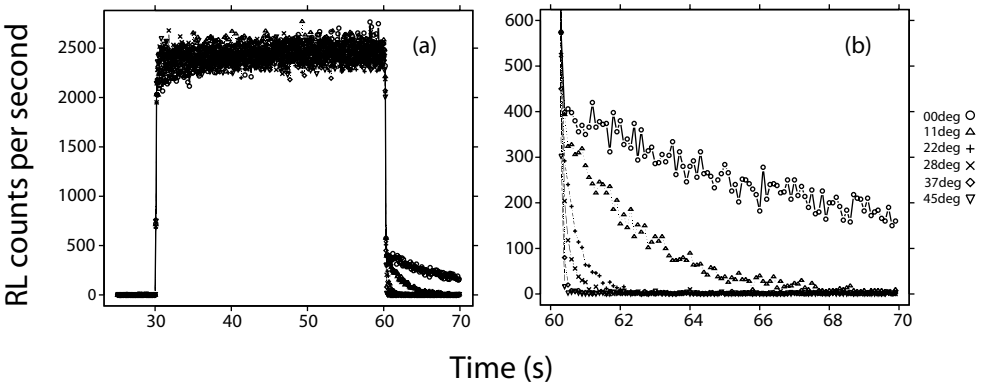

Figure 4.12: RL response of the probe at different temperatures. (a) total RL signal: no clear trend can be observed with increase in temperature; (b) detail of the afterglow: the decay rate increases with high temperatures.

4.8 Spatial resolution

A lateral profile was measured in a 5x5 cm^2 field for 6 MV photons (with an Elekta SLi plus at UMAS), at a depth of 10 cm in a water phantom, illustrated in figure 4.8. The diode and RL/OSL data were normalized to the result obtained at the center of the field. These results show that the spatial resolution of the RL/OSL detector system makes it suitable for measurements of depth and lateral dose distributions in clinical photon beams. The spatial

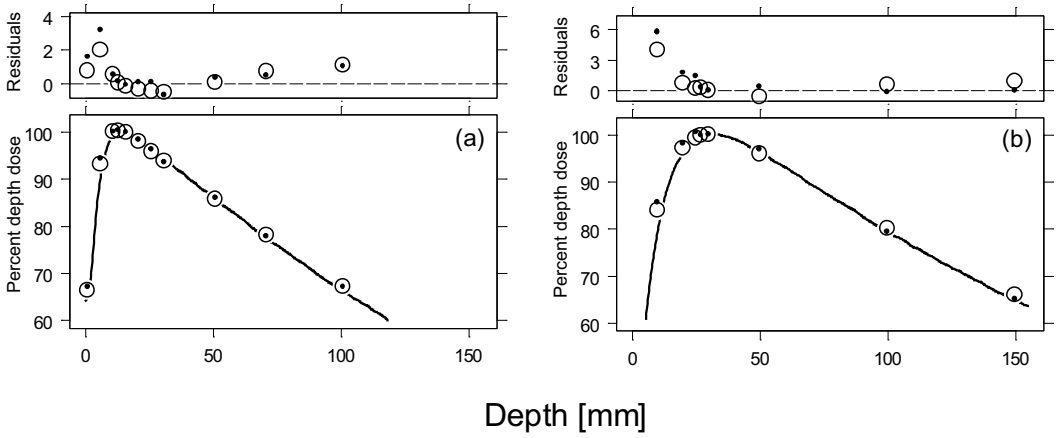

Figure 4.13: Depth dose distributions for 6 and 18 MV photons. Solid line: diodes, hollow symbols: OSL, full symbols: RL.

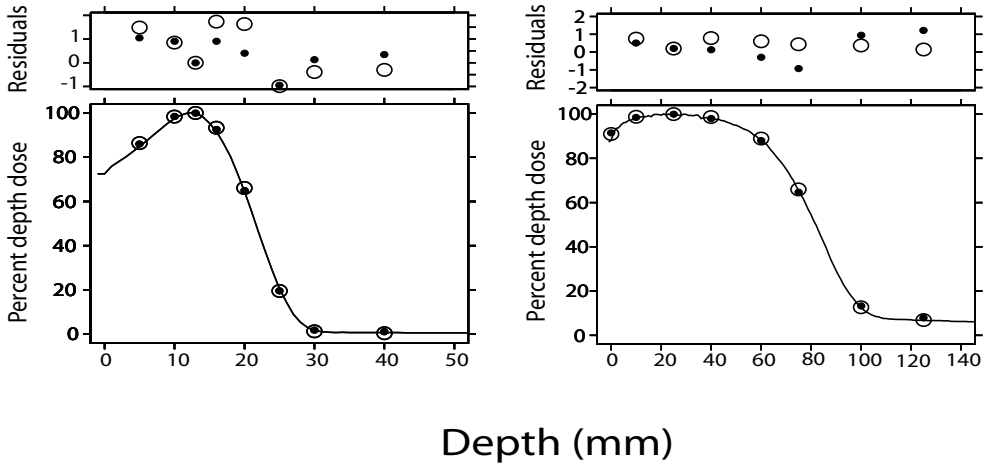

Figure 4.14: Depth dose distributions for 6 and 22 MeV electrons. Solid line: diodes, open symbols: OSL, filled symbols: RL. The inserts on top of the graphs show the discrepancy between diode and luminescence data.

resolution of the RL/OSL dosimeter could also be improved by using smaller crystals, such as those from fibers 48 and 49.

4.9 Sources of variability

In light of these measurements, several source of variation in the response of the RL/OSL dosimetry system have been identified and are listed in table

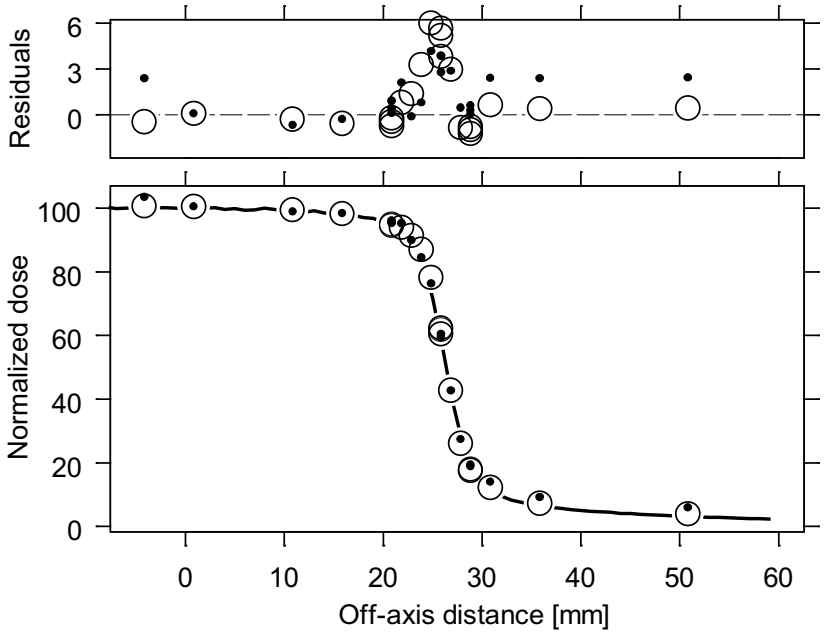

Figure 4.15: Lateral profile for 6 MV photons. Solid line: diodes, hollow symbols: OSL, full symbols: RL.

4.1. Some parameters which have not been mentioned previously are also detailed in this section.

4.9.1 Mechanical sources

Optical transmission effects

In fiber 01, no adhesive was used between the crystal and the fiber, which were held together by a shrinkflex wrapping. As a result, slight motion of the crystal with respect to the end of the optical fiber were possible. This coupling was improved with the new probe design using NOA-61. Some variability is also present when fibers are detached from the reader and then reattached to it: SMA connectors do not offer a highly reproducible coupling, and this effect has been shown to effect the response of the RL/OSL dosimetry system by up to 20%. Consequently, the system was calibrated every time the fibers were re-attached to the optical reader. In some situations, the fibers are taped to the treatment table: for example, they need to be out of the way of the nursing personnel during patient set-up. In contrast, during a phantom experiment, the fibers are left to run freely on the floor. Taping the fibers to the table may necessitate to bend them slightly, but should not

Table 4.1: Sources of variability in dosimetric measurements with the RL/OSL optical fiber system

Source	Type	Effect	Significance
Mechanical	Crystal-fiber	Loss of signal if improper coupling coupling	Major in fiber 01 minor in new fibers
	Fiber-reader connection	Variation in signal transmission with every plugging/unpluggin of fibers to reader	up to 20% variation (0.6% per C degree)
	Damage optical cable	Impaired transmission if the fiber is damaged and bent	Major in *in vivo* measurements
	PMT temperature	Variation in response if no warm-up or if changes in room temperature or (e.g., poorly insulated laboratory)	up to 10% variation (0.6% per degree)
	Laser instability	Uncertainty in OSL dose estimate	Only if very short integration times are used
Luminescence	Crystal temperature	Variation in OSL response and RL afterglow	Minor in *in vivo* meas.
	Improper bleaching	Residual signal in the crystal	Minor if long bleaching (>400s)
	Stem effect	Noise signal generated in the optical fiber Affects only the RL signal	Minor in standard meas. Major in IMRT meas.
Dosimetry	Angular dependence	Variation in response with beam incidence	Minor
	Energy dependence	Variation in response at depth or in different beam energies	Minor
	Linac output (absolute)	Uncertainty in the accuracy of the absorbed dose delivered by the linac	Minor
	Linac output (initial)	Slow start up of the linac, varying dose rate	Major if "initial" RL method is used for RL dose estimate
	Set-up	positioning uncertainty of the crystal in the field	Minor
	Air cavities	Presence of air in a phantom assumed to be homogeneous solid water	Minor

interfere with signal transmission as long as the fiber is undamaged. If the fiber cable is, on the contrary, damaged, the transmission of the luminescence will be impaired.

PMT temperature or "warm up effect"

The time interval between the system "power-on" and the data acquisition is an important factor. Indeed the temperature inside the reader varies after start-up and takes some time to stabilize. We know from experience that measurement taken shortly after the system has been switched on exhibit poor reproducibility (up to 10% standard deviation). Further investigation revealed that this "warm up effect" resulted in a decrease of the signal of 0.6% per Celsius degree. The logical recommendation is that the reader should stay switched on as long as possible before a measurement.

4.9.2 Effects due to the crystal

Luminescence

As was demonstrated in this chapter, the temperature of the crystal is going to affect is luminescence output. Another source of variability is the presence of residual signal due to improper bleaching: if the crystal is not stimulated with laser light for a sufficient amount of time, a residual signal will be present in the next measurement. This effect may amplify with each measurement until the accumulated residual signal can have a noticeable effect on the dose estimate. In the dose rate dependence experiment presented in section 4.3, the OSL signal presents a "trend": the absorbed dose estimate seems to decrease with repeated measurements. This phenomenon can be observed if the fibers are not properly bleached after each measurement. Hence, care must be taken to bleach the crystal as long as possible (and for at least 400s with the laser power presently used in the RL/OSL system) between measurements. This is especially valid if the crystal has been exposed to a high dose (>5 Gy). The stem effect, whose importance is related to the signal-to-noise ratio of the "crystal+fiber" assembly is also a considerable source of variability of the RL signal.

Dosimetry

Other factors affect the response of the crystal, although they are not related to luminescence phenomena. For example, the angular dependence is linked to the shape of the detector. The energy dependence is caused by the higher Z_{eff} of Al_2O_3:C . External factors, such as the stability of the radiation source

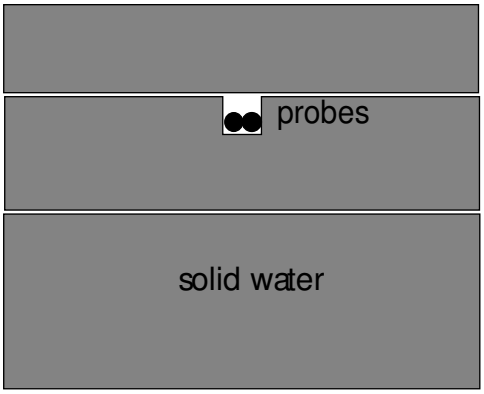

Figure 4.16: Position of fibers in a solid water phantom in presence of air cavities.

(here, the linac) as well as the precision of the set-up will introduce some variability in the measurements.

One last parameter is related to the composition of the solid water phantom used for some measurements in this chapter. For measurements in a solid water phantom, a groove was drilled into a solid water plate in order to accommodate the fibers. However, the fibers do not totally fill this groove. Hence, the phantom is actually a inhomogeneous volume consisting of air and solid water (as well as plastic fibers). The dose distribution may differ slightly from the one which would be performed on a homogeneous phantom (Haraldsson et al., 2003). This effect may be more significant at certain angles, which means it is more critical in IMRT than in conventional measurements. Its impact is difficult to quantify exactly, but should add an uncertainty of at least 1-2% on the absorbed dose estimate.

4.10 Conclusion

It can be concluded from this investigation that the RL/OSL dosimeter does not suffer from any major dependence (>5%) on beam parameters. The variation in response of the RL/OSL detector was generally smaller than 1.5% (1SD) and in many cases smaller than 1%. One exception is the angular dependence, though this effect may be reduced with smaller crystals. These results suggest that the overall accuracy of RL/OSL dosimeter is satisfactory for radiotherapy purposes.

The potential sources of variability (mechanical, crystal-related, dosimetric) have been identified and, when possible, quantified. Bearing these uncertainties in mind is useful in order to use the RL/OSL dosimetry in the most reliable way when it is applied to treatment-like measurements.

5 Clinical applications in radiotherapy

Once the basic dosimetric parameters had been tested and judged satisfactory, the RL/OSL dosimetry system was submitted to more realistic situations: a conventional radiotherapy treatment in an anthropomorphic phantom and IMRT treatment simulations on a solid water phantom. Three *in vivo* measurements were performed on IMRT patients. These treatment modalities present an increasing level of complexity from a dosimetric (and, for the patient measurements, practical) point of view. The results from these measurements are the main topic of this chapter, and a careful review of the challenges inherent to each situation is given.

5.1 Conventional radiotherapy simulation in an anthropomorphic phantom

The first experiments in a patient-like set-up were performed at Malmö University Hospital in Sweden in April 2003 (Aznar et al., 2004). Data were acquired at a sampling rate of 10 Hz, using fiber 01. We chose to test the RL/OSL dosimetry system by simulating a relatively simple treatment of the pelvic area. An anthropomorphic phantom (Alderson Rando Phantom, Alderson Research Labs, Inc., Stamford, USA) was chosen, and the pelvic portion of this phantom was scanned in a CT-scanner (see figure 5.1(a)). Two treatment plans were then designed with the TMS treatment planning system (Helax, Uppsala, Sweden).

Two types of dose delivery were chosen (see figure 5.2):

- The first plan consisted of two parallel-opposed "anterior-posterior" and "posterior-anterior" (AP-PA) open fields, delivered using 10 MV photon beams with field size 10x10 cm^2.

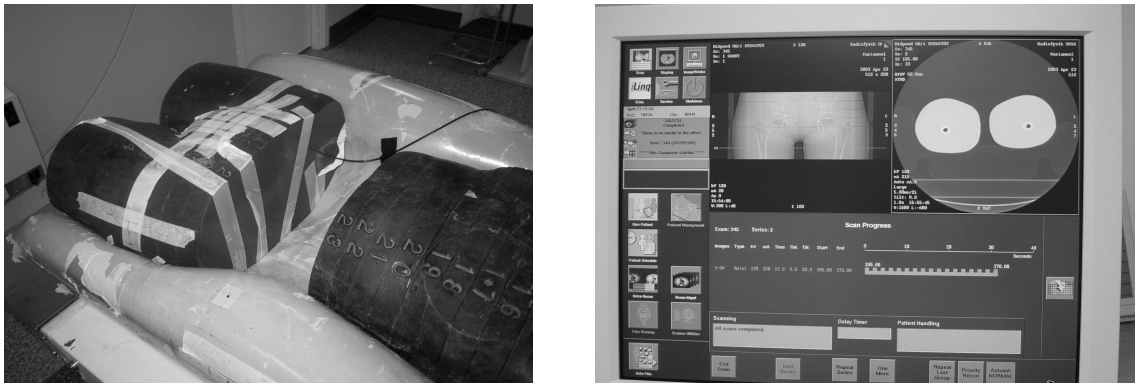

(a) Position of the fiber in the phantom (b) CT scanning

Figure 5.1: Position of the fiber in the anthropomorphic phantom during CT-scanning.

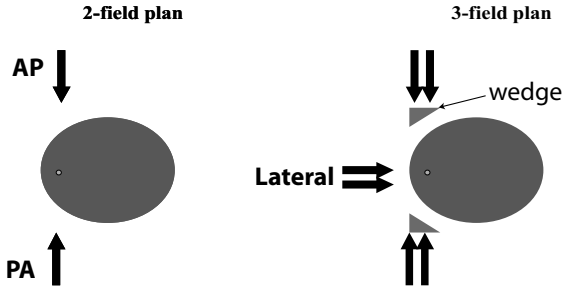

Figure 5.2: Treatments plans for the anthropomorphic phantom: the first plan consists of two opposed fields in the anterior-posterior direction; the second plan includes, in addition, a lateral field and wedges for dose homogeneity within the target volume.

- The second plan included, in addition to the AP-PA fields, a 7x10 cm^2 right lateral field, as well as some filters ("wedges") for the AP-PA fields to obtain a homogeneous dose distribution

Both plans were normalized to deliver 1.0 Gy at a specific point in the phantom.

This normalization point was chosen to be in one of the channels of the phantom, where the fiber could be introduced. An absorbed dose of 1 Gy was planned to be delivered at the location of the crystal with an Elekta SLi plus accelerator. The RL signal was collected for each field during irradiation, and the OSL signal was measured at the end of each treatment fraction. Each plan was delivered at two occasions. These results were compared to a calibration dose of 1.0 Gy at 100 cm SSD in solid water, at the depth of

2 cm, which was repeated three times before the delivery of the treatment plans, and once after.

Hence, in all these experiments, the same absorbed dose of 1 Gy was delivered to the RL/OSL detector in three different fashions:

1. in a simple set-up with a solid water phantom
2. in an anthropomorphic phantom with a 2-field plan and only 6 MV photons
3. in an anthropomorphic phantom with a 3-field, and using 6 and 10 MV photons.

Table 5.1: Results from the experiment using an anthropomorphic phantom.

Type of irradiation	OSL (Gy)	RL (Gy)
Calibration 1	1.008	1.003
Calibration 2	1.001	1.004
Calibration 3	1.001	1.004
2-field plan 1	0.977	0.976
2-field plan 2	0.992	1.003
3-field plan 1	0.995	1.000
3-field plan 2	0.978	0.986
Calibration 4	0.990	0.989

Since several fields are considered, each yielding a slightly different dose rate at the location of the detector, the sum of the RL signal was used to establish a dose estimate. Table 5.1 gives a detailed view of the results. It can be seen that there is a tight agreement between the RL and OSL results in every case, which suggests that the stem-effect and the sensitization phenomena do not impair a reliable dose estimate in this relatively simple set-up. Results from both the 2-field and the 3-field treatments are approximately 2% below prediction. This discrepancy is likely to be caused either by a small imprecision in setting up the anthropomorphic phantom or positioning the fiber inside the channel, or by uncertainties in the dose prediction from the TPS (most TPS in clinical use today claim an accuracy of 2-3%). The results of the four calibrations agree within 1% where the largest deviation was found for the set-up after delivery of the four treatment plans, including the uncertainty caused by re-positioning the detector in the field at the specified depth of measurement. An analysis of variance (ANOVA) between calibration data and treatment data shows that no significant variation can

be observed between those two groups (p=0.5 for OSL data, and p=0.27 for RL data). This suggests that the RL/OSL system can reliably estimate the dose from 2-field and 3-field treatments in a solid water phantom: the orientation of the beams, the difference in energy spectrum (due to the position at depth, the presence of wedges and the inhomogeneities in the anthropomorphic phantom) as well as the different beam energies, did not affect the response of the RL/OSL dosimeter.

5.2 IMRT simulation in a solid water phantom

To test the ability of the RL/OSL dosimetry system to assess the absorbed dose to the target volume in these extreme dosimetric conditions, several phantom experiments were first performed in a solid water phantom. The set-up was similar to the one used for the treatment QA with the ionization chamber. The following data was acquired with fibers 48 and 49. The solid water phantom was set up on the couch. Slabs were selected so that the total thickness of the phantom was 15 cm, and the fibers were positioned 2 cm below the surface. A quick reproducibility and linearity check was performed and used as calibration data. Particularly, several shots of 200 MU were delivered with a 6 MV beam to deliver an absorbed dose of 1.96 Gy at the position of the fibers. The IMRT plan was then loaded and delivered to the phantom. RL data were acquired during the duration of the exposure (around 15 minutes) and the resulting signal is displayed in figure 5.3. OSL was acquired once the delivery was completed, and the process was repeated 3 times. The results are presented in table 5.2.

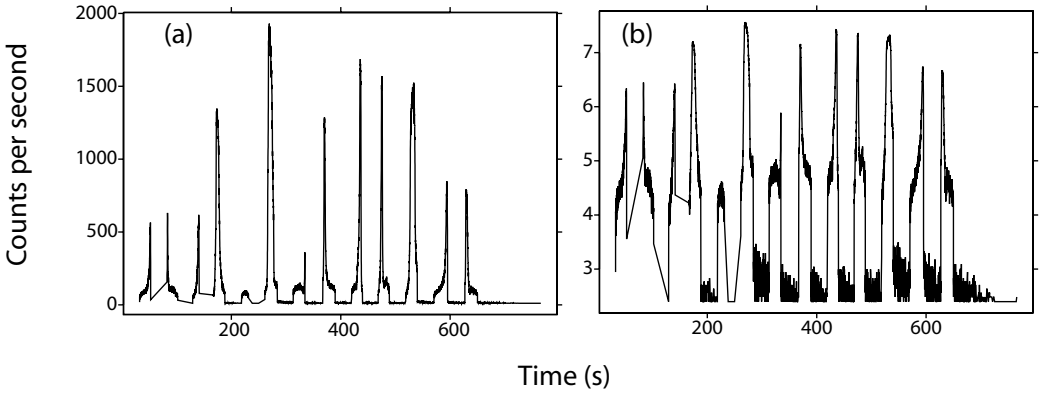

Figure 5.3: RL signal for the IMRT treatment in a solid water phantom: (a) linear scale, (b) semi-log scale.

Table 5.2: RL/OSL results from the IMRT treatment in a solid water phantom with fibers 48 and 49.

Signal	Fiber 48 Dose (Gy)	Fiber 49 Dose (Gy)	TPS Dose (Gy)	Fiber 48 vs TPS	Fiber 49 vs TPS
RL1	2.202	2.221		20.7%	19.7%
RL2	2.225	2.249		22.2%	20.9%
RL3	2.225	2.245		22.0%	20.9%
OSL1	1.819	1.812	1.84	-1.1%	-1.5%
OSL2	1.812	1.807		-1.5%	-1.8%
OSL3	1.807	1.796		-1.8%	-2.4%

5.2.1 RL results: stem effect and sensitivity changes

The RL data show a clear overestimate, which is mainly due to the influence of the stem effect and of the sensitivity changes throughout the dose delivery. In most experiments described in chapter 4 and in the anthropomorphic phantom experiment, the crystal is in the center of the irradiation field. In dynamic IMRT however, because the field shape changes during the exposure, the crystal might be out of the field at some occasions, while some portion of the optical fiber is being irradiated. In this situation, only the stem effect will be recorded. The total signal to noise ratio of the RL signal is then greatly affected. Moreover, with complex treatments such as IMRT, the dose rate varies greatly during a very short time, as is clearly seen in figure 5.3. Hence, the sensitization effect can not be contoured by using only the initial RL readings (as was done in chapter 4). As a result, though each field can clearly be visualized, the uncorrected RL signal can not be used to estimate the absorbed dose to the detector.

5.2.2 OSL results

The agreement between the OSL data and the TPS prediction is within 3%. Apart from the possibility of inaccuracies from the TPS itself, the potential sources of discrepancy are analyzed in the following sections.

Positioning uncertainties

The raw RL signal can be used as a "fingerprint" of the position of the two fibers. Indeed, if the fibers were apart for more than, say, 1mm, their

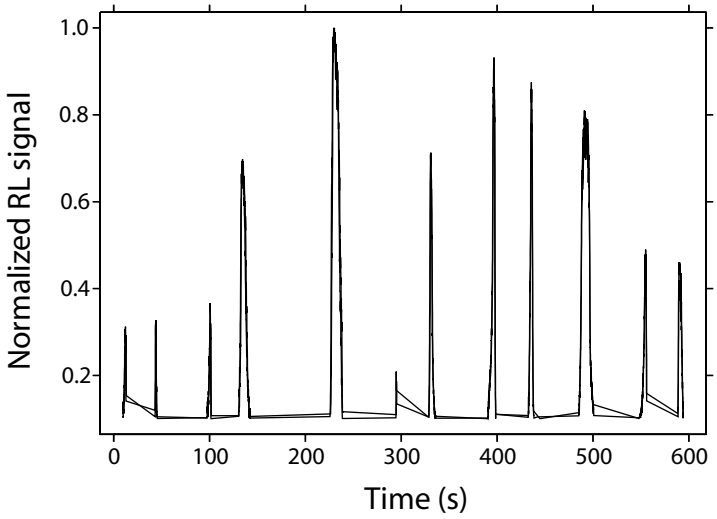

Figure 5.4: The RL signal can be used as a "fingerprint" of the fibers' respective positions. Here, the signals from fiber 48 and fiber 49 overlap, i.e. the two fibers were in the same measurement location.

respective crystals would not always be in the beam simultaneously: this should be noticeable looking at the shape at the RL signals. Figure 5.4 shows that the RL signals from both fibers are indistinguishable: we can safely conclude that the two probes were at the same measurement location. However, there are other types of positioning uncertainties. IMRT is by definition a highly conformal treatment modality, and as a result, there is a sharp dose fall-off outside the target volume. If the probes are located in one of the high gradient dose regions, a positioning uncertainty of 1 mm could result in a difference of several percent on the total absorbed dose estimate. Even though care was taken to position the probes as precisely as possible at the isocenter, some issues could have been overlooked. For example, figure 4.16 shows the position of the probes in the solid water phantom, and the potential uncertainty in positioning in the AP direction. The effect could add an uncertainty of about 2% on the final absorbed dose estimate.

5.3 *In vivo* IMRT

5.3.1 IMRT with TLDs at Rigshospitalet

Intensity modulated radiation therapy is a complex procedure (see chapter 1) and *in vivo* dosimetry is strongly recommended. At Rigshospitalet, 2-3 patients per month are treated with IMRT for cancers of the head and

neck region. *In vivo* dosimetry was usually performed with TLDs (Haraldsson et al., 2003). Each patient's treatment plan is tested with an ionization chamber in a solid water phantom as part as the treatment QA (see chapter 1). The day of the first treatment fraction, several LiF TLD rods (1 mm ø x 6 mm ℓ) are positioned inside a catheter (Maersk Medical A/S) along with lead markers, in order to aid the localization of the pellets on the portal images. The catheter is then inserted through the nose of the patient down into the oesophagus. After the treatment fraction is delivered, the catheter is withdrawn and the TLDs are extracted and measured in a special TL apparatus (Harshaw 5500 reader). It has been reported that the TLD readings from 6 patients (15 fractions, 153 measurements) show an average ratio of measured versus planned (TPS) dose of 0.99±0.06 (Van Esch et al., 2002). Though this procedure has the advantage of giving a dose estimate at several points within the treatment volume, it is time consuming. As an alternative, three conclusive *in vivo* measurements have been undertaken with the RL/OSL dosimeter between September 2003 and February 2004. These measurements were performed in patients treated for cancer of the head and neck region with IMRT. The catheter/lead markers assembly was the same as the one used for the TLDs. Measurements were carried out either with fiber 43 alone or with both fiber 48 and fiber 49 inserted in the catheter. In the latter case, two separate estimates of the absorbed dose at the same point are obtained.

5.3.2 Protocol for RL/OSL measurements in patients

With *in vivo* measurements, some practical issues must be considered, such as minimizing the interference of the measurement with the actual treatment. Also, calibration must be kept to a minimum if it has to be performed shortly before or after the treatment (since the machine has to be used to treat more patients). We established the following procedure:

- Before treatment: one data point was obtained in solid water (2 Gy)
- During treatment: real-time RL acquisition
- After treatment: the fibers are removed from the catheter, the system is shut down and moved to another location where OSL is acquired.
- Additional dose-response tests are performed for the calibration of the RL/OSL system.

5.3.3 Potential sources of uncertainty

Positioning: probe, set-up and patient motion

In addition to the positioning issues discussed for the phantom case, several uncertainties are specific to an *in vivo* measurement. Indeed, if the probe moved away from the lead marker during the insertion of the catheter in the patient, it is unlikely to be noticed. The set-up of the patient itself is subject to uncertainties and this can affect the dose delivery at the position of the probe. Finally, even if the patient is perfectly set-up and immobilized, the internal organs can move by 1.5 mm during a single treatment fraction (due to breathing, deglutition, etc) (Kim et al., 2004). If the detector is positioned in a high dose gradient, all these small motions can lead to a considerable discrepancy between the TPS estimates and the absorbed dose recorded by the crystal. The importance of positioning the detector in a region of low dose gradient seems obvious. In practice however, this is not easily achievable, because of time and imaging constraints. If the dose is positioned in a high gradient region, a 2 mm uncertainty in positioning could result in a 5% uncertainty on the dose estimate.

TPS error: inhomogeneities

The solid water phantom with which the TPS calculations were performed for the previous experiments is homogeneous. The head and neck area of a real patient will contain soft tissue, air (sinuses, trachea) and bone (facial bones, spinal processes). The algorithms used to model the interaction of radiation with matter have greatly improved over the years. Nonetheless, the way they handle interactions in an inhomogeneous media is not perfect. It has been shown that the uncertainty on the TPS dose estimates can be significant, especially with the presence in inhomogeneities in the medium (Knoos et al., 1995), (Jeraj et al., 2002). In the case of a head and neck patient, this uncertainty could be as high to 1-2%.

5.3.4 Results from RL/OSL *in vivo* measurements

OSL Results from the 3 patient measurements are presented in table 5.3. The uncertainty on the OSL dose estimates is given in the form of confidence intervals (95%). OSL dose estimates are within 2% of the predicted dose for all measurements except one. In the third patient measurement, fiber 48 give an absorbed dose estimate which lies 19% below the TPS value. The "fingerprint" from the RL signal shows that the two fibers were at the same location in the patient. Because of the sensitization and stem effects

Table 5.3: Results of three *in vivo* measurements: OSL absorbed dose estimates versus predicted doses from the treatment planning system. Confidence intervals (95%) are given for the OSL estimates.

Patient	Fiber	OSL (Gy)	TPS (Gy)	OSL vs TPS
2	43	1.73 *(1.66-1.80)*	1.760	-1.7%
4	48	1.83 *(1.79-1.87)*	1.852	-1.1%
4	49	1.82 *(1.79-1.85)*	1.852	-1.7%
5	48	1.64 *(1.63-1.65)*	2.030	-19%
5	49	2.06 *(2.04-2.08)*	2.030	1.5%

(which are not corrected for), it is expected that the RL signal will lead to a gross overestimate of the absorbed dose at the location of the detector. Indeed, in most cases, analysis of the RL signal leads to an overestimate the dose by 20% or more. However, in the third patient measurement, the RL dose estimate from fiber 48 is actually 11% below the TPS prediction. After the patient measurement, the dose-response test of fiber 48 showed excellent reproducibility and linearity of the signal. This suggests a technical or mechanical problem during the patient measurement. Indeed, the transmission properties of fiber 48 were tested and showed that the fiber had been damaged. As a result, the transmission of laser light or luminescence signal is much lower when the fiber is bent (see section 4.9.1). This was the case for the patient measurement: during the treatment, the fiber was bent and taped to the treatment table to avoid interference with the patient set-up (resulting in a reduced RL acquisition). Right after the treatment, while the OSL was acquired, the fiber was rolled on itself to avoid lying on the floor. However, the dose-response test was performed in a treatment room where the fiber was straight and transmission was not impaired. Apart from this particular instance, the RL/OSL dosimetry system showed to provide reliable and accurate absorbed dose estimates for IMRT treatments. The RL signal, however, was not used to its full potential in the absence of stem effect and sensitization corrections.

5.4 IMRT with improved RL analysis

In summer and fall 2004, some IMRT measurements were repeated using the sensitization correction and temporal gating methods described in chapter 3. With these methods, it is possible to correct for the sensitization effect by calibrating the sensitivity changes in the crystal with respect to accumulated dose. Moreover, temporal gating takes advantage of the longer lifetime of the

radioluminescence compared to the light generated in the optical fiber. In IMRT treatments, dose rate variations are large and stem effects are important since the detector is not always in the irradiation field. Hence, IMRT measurements represent the ultimate test of the RL correction methods.

Fibers 43 and 37 were used in a solid water phantom. The system was first calibrated with a fixed field (10 cm x 10 cm) of a 6 MV beam, with the detectors positioned slightly apart at a depth of 2 cm in a 15 cm thick phantom. The position of the two fibers is shown in figure 5.6. In order to take into account the influence of small uncertainties in the positioning of the fibers, several dose estimates were obtained from the TPS within a 2 mm cube centered on the assumed location of the fibers[1]. Three successive deliveries of the IMRT plan were performed. The reproducibility of the RL signal is illustrated in figure 5.5. Figure 5.7 illustrates the RL "fingerprint" phenomenon: the fibers are only a few mm apart but their luminescence output are considerably different, as is expected in a high dose gradient. The absorbed dose estimates from RL and OSL are summarized in table 5.4. Because the RL results are now meaningful, field-by-field absorbed dose estimates are presented. RL dose estimates are highly reproducible among the 3 measurements at 0.2% (1SD) for fiber 43 and 0.04% for fiber 37. OSL results showed standard deviations of 0.7% and 0.04% for fibers 43 and 37, respectively. The results show a good agreement between RL and OSL dose estimates (1% 1SD for fiber 43, 0.3% 1SD for fiber 37). Luminescence results deviated from TPS values by 2% (RL) and 3% (OSL) for fiber 43 (probe A), and by 1% (RL) and 0.4% (OSL) for fiber 37 (probe B). Field-by-field dose estimates from the RL signal are highly reproducible and always within the "dose estimate window" given by the TPS, except in the case of field #5 for both fibers. These results suggest that both fibers can reliably estimate the absorbed dose in IMRT measurements. They also indicate that fiber 37 is more precise, and possibly more accurate than fiber 43. This difference between the two fibers is probably due to the inherent characteristics of each crystal (see chapter 3). The results also validate the RL correction methods, and confirm the potential of the RL signal for field-by-field absorbed dose estimates.

[1]Since the TPS calculations are performed with a voxel size of 5 mm, measuring the dose 2 mm away from the point of measurement will only give qualitative information about the presence of a dose gradient. However, the "dose estimate window" read in this 2 mm cube might not accurately represent the quantitative dose variation.

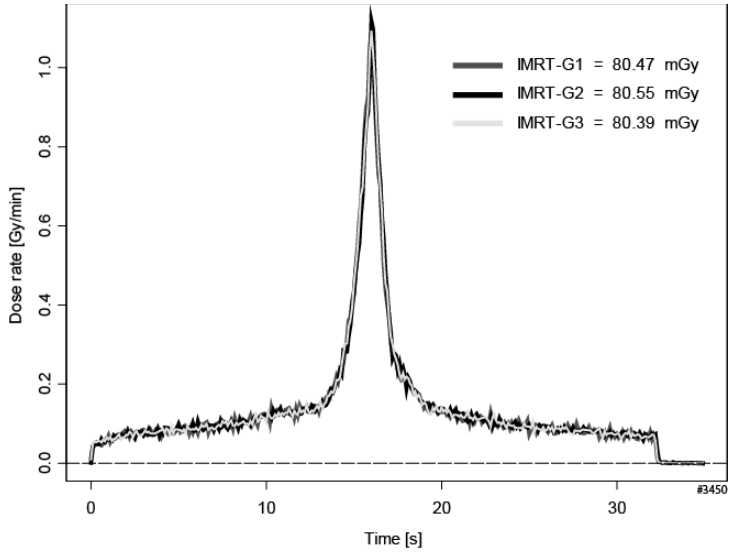

Figure 5.5: Field 1 dose delivery versus time with probe A (fiber 43). Note the high reproducibility from treatment to treatment (IMRT-G1, G2, and G3).

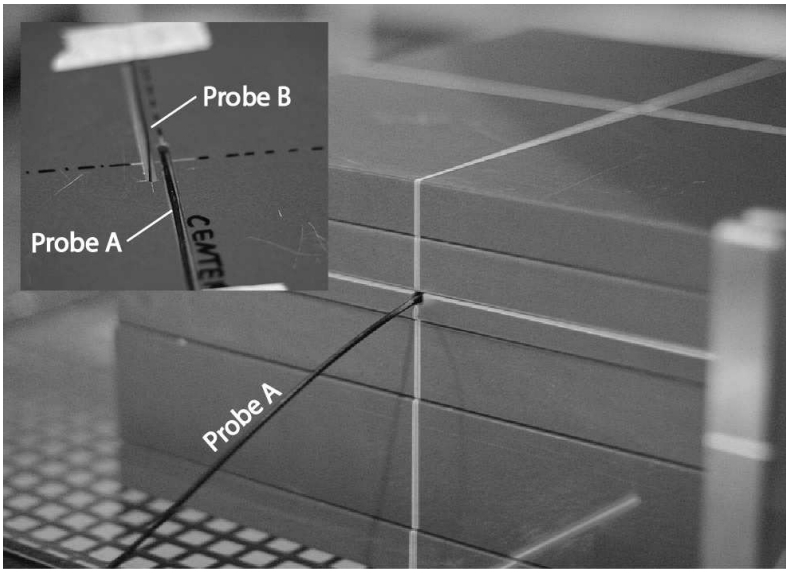

Figure 5.6: Position of fibers 43 (probe A) and 37 (probe B) in the solid water phantom.

5.5 Conclusion

The measurements presented in this chapter show that the RL/OSL dosimeter can estimate the absorbed dose within 2-3% even in complex situations, such as *in vivo* IMRT. Some results suggest that this accuracy could be

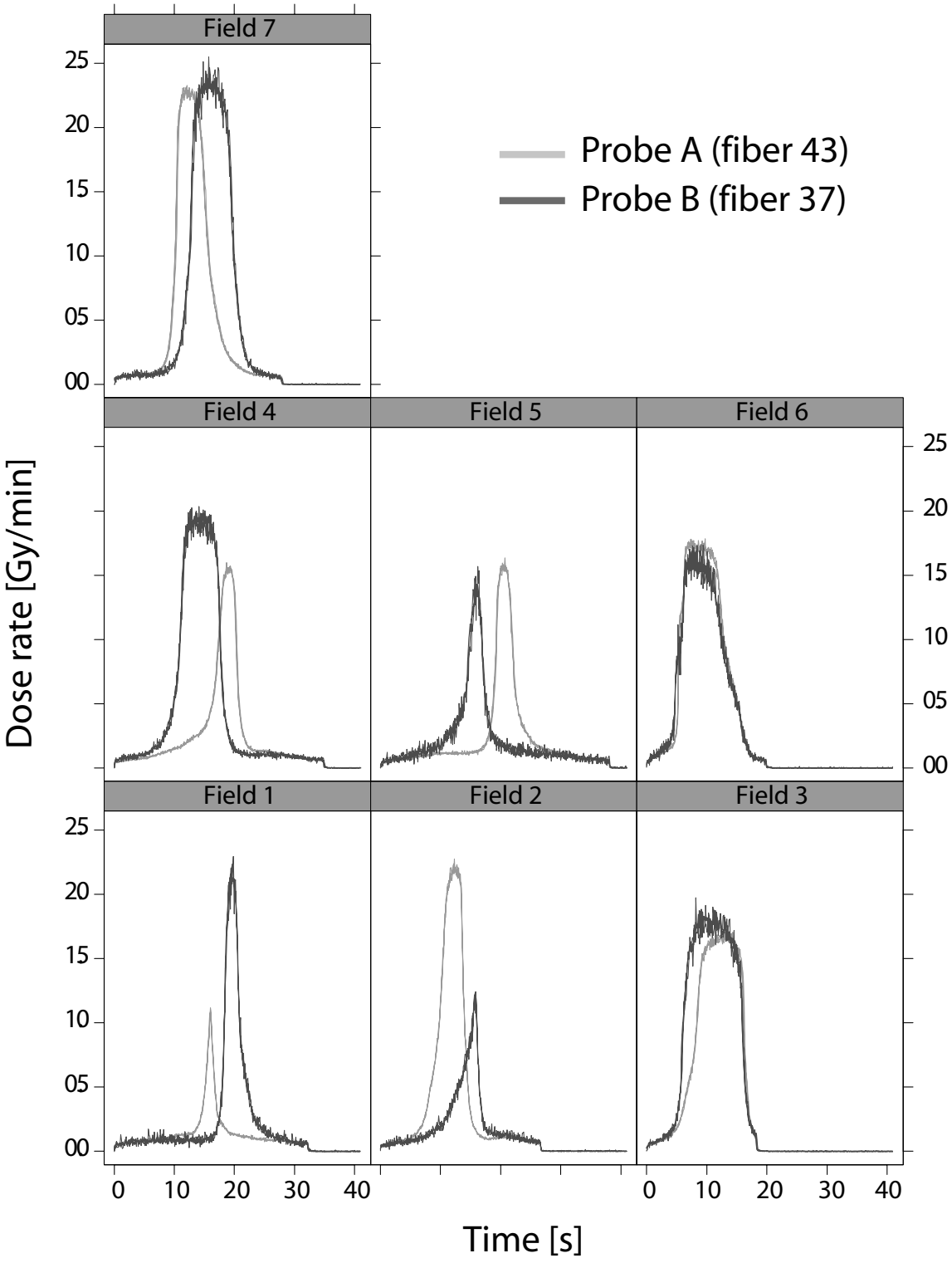

Figure 5.7: Field by field dose delivery versus time for probes A and B. The offset between the signals confirms that the fibers are a few mm apart.

improved to reach 1% if care is taken to choose a good fiber (i.e., highly reproducible, and showing no sign of damage) and to follow a certain protocol (i.e., very accurate set-up, adequate warm-up of the system before the measurement, etc). The RL and OSL signals can both reliably estimate absorbed doses. The RL signal also offers the possibility of estimating the individual dose from each field in an IMRT treatment. Hence, the RL/OSL can provide two independent dose estimates from the same *in vivo* treatment: one integrated dose estimate (OSL) and one real-time dose estimate (RL), which can be compared to one another, and act as a useful "diagnostic tool" in case of an odd result. These measurements also demonstrate the considerable potential of the RL signal for giving a "fingerprint" of the fibers: small positioning errors can be picked up by looking at the unique dose rate information delivered by each fiber. Two patient measurements failed for reasons unrelated to the performance of the RL/OSL dosimetry system (for one patient treatment, the lead markers were not visible and the location of the probe was unknown; for the other, a manipulation error occurred and the PMT was switched off during OSL acquisition). Three conclusive patient measurements for IMRT of the head and neck region were performed and confirmed the considerable potential of the RL/OSL dosimetry system.

Field	Gantry (deg.)	Probe A (mGy)				Probe B (mGy)			
		TPS min - max	IMRT-G1	IMRT-G2	IMRT-G3	TPS min - max	IMRT-G1	IMRT-G2	IMRT-G3
1	0	86 80 - 90	80	81	80	156 140 - 174	150	146	149
2	51	212 188 - 236	198	197	197	90 80 - 102	102	99	100
3	102	242 224 - 256	251	250	250	306 294 - 312	303	300	301
4	154	152 142 - 164	156	155	155	278 268 - 284	273	272	273
5	206	174 162 - 186	149	148	148	158 146 - 170	137	142	140
6	258	272 240 - 292	251	251	251	216 190 - 244	235	237	235
7	309	236 210 - 264	249	250	249	324 314 - 336	314	316	315
Total dose from RL		1372 1264 - 1468	1333	1333	1329	1528 1476 - 1562	1514	1514	1513
Total dose from OSL			1358	1343	1360		1522	1523	1523

Table 5.4: Dose estimates in mGy for three IMRT treatments in a solid water phantom: IMRT-G1, IMRT-G2, and IMRT-G3 and the corresponding reference values from the treatment planning system (TPS). To indicate the influence of set-up errors, we both report the TPS values for our best estimates of two probe locations (A and B) as well as the minimum and maximum of TPS values observed ± 2 mm away (along the three principal axes). For example, the TPS value for probe A, field 1 is 86 mGy, but values from 80 to 90 were observed in the ± 2 mm cube.

6 Clinical applications in mammography

In vivo dosimetry in mammography is a different challenge than in radiation therapy. First of all, it is not a common procedure: most of the dosimetry checks in mammography are done without any patient present and are performed in air or with a plastic phantom, usually using ionization chambers. *In vivo* measurements have been reported with TLDs (Zoetelief et al., 1996; Berni et al., 2002) and MOSFETs (Peet and Pryor, 1999; Dong et al., 2002) but they are not used routinely. The RL/OSL dosimeter was used in the diagnostic radiology department at Malmö University Hospital to investigate its potential for *in vivo* dosimetry in screening mammography (Aznar et al., 2005a). One advantage of the RL/OSL dosimeter is its high sensitivity: very small doses, such as those observed on the inferior surface of the breast during a mammographic examination, can be measured. This quantity could help determining if some patients are exposed to higher doses than expected because of the specific density of their breasts. For our purposes, the most significant difference with radiotherapy is that the requirement for accuracy is much lower: the goal here is not to determine exactly what dose was delivered at a specific point in a patient, but to prevent potentially healthy women from being exposed to a higher level of radiation that necessary. Another important factor is the size of the dosimeter: *in vivo* dosimetry should not impair the diagnostic outcome of the mammographic examination. As a result, the dosimeter should as small as possible, and should not be confused with a potential malignancy on the mammogram.

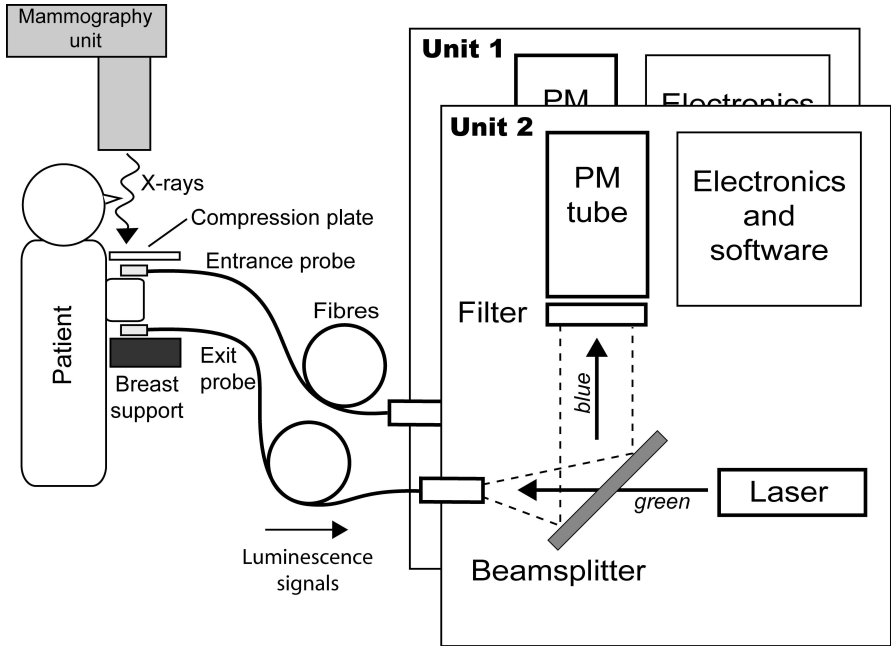

Figure 6.1: Illustration of a mammography measurement set up, showing the principal components and the position of the fibers.

6.1 Dosimetry in mammography

6.1.1 Diagnostic equipment used in these experiments

All the experiments described in this chapter were performed with a mammography unit (type Siemens Mammomat 3000) using a Molybdenum / Molybdenum (Mo/Mo) anode/filter combination. The tube potential of the mammography unit ranged from 23 to 35 kV. The images acquired during the experiments were developed with a screen-film system (type Kodak Min-R 2190/Min-R 2000). Whenever relevant, the signals from the RL/OSL dosimeter were compared to the reading of a flat ionization chamber (type TB23344 from PTW Freiburg, Germany). A polymethylmethacrylate (PMMA) phantom (area: 240 x 150 mm^2) was combined to various thicknesses and was used to simulate the presence of breast tissue. Mammography beams are not very well qualified by the tube potential (in kV) alone: it is considered that the half value layer (HVL) is a better indicator of beam quality. Hence, HVL measurements have been performed for all the beams used in these experiments. Figure 6.1 illustrates the mammography unit as well as several important components.

6.1.2 Quantities measured

In mammography, detectors are often positioned free in air, or at an interface between tissue and air (e.g., on the skin). As a result, charged particle equilibrium is not always presented, and the equality between kerma and absorbed dose (see chapter 2) is not valid.In such conditions, the quantity of interest is the air kerma as opposed to absorbed dose. The risk from radiation for women undergoing mammography examinations is currently described by the average absorbed dose to the glandular tissue. However, this quantity is not directly measurable and must be calculated from beam-related parameters. These parameters include the half-value layer (HVL) of the beam and the entrance surface air kerma (ESAK). The ESAK represents the incident air kerma at the breast surface measured free in air, and without backscatter. The ESAK and the HVL values are usually measured with an ionization chamber and without any patient present. For each patient exposure, the loading of the x-ray tube (expressed in mAs) and compressed breast thickness are recorded and the ESAK value can be calculated for that particular exposure. Published conversion factors (Dance, 1990; Zoetelief et al., 1996; Dance et al., 2000a) are then used to calculate the AGD from the ESAK value (with the assumption that the breast composition is 50% fat and 50% glandular tissue).

If *in vivo* measurements are performed, say with thermoluminescent (TL) dosimeters placed on the superior surface of the breast, then the entrance surface dose (ESD) is measured. The ESD is a measure of the radiation dose absorbed by the skin where the x-ray beam enters the patient. The ESD is then divided by an appropriate backscatter factor (BSF, tabulated as a function of HVL) to obtain the ESAK, and then finally the AGD.

6.2 Basic dosimetry characteristics

6.2.1 Protocol

The output of a mammography unit is characterized by low photon energies and high dose-rates. Typical RL and OSL signals generated by the Siemens mammomat 3000 for 40 and 80 mAs pulses are sketched in figure 6.2.1. Because of the high dose rate and the short exposure times, the RL signal appears as a high, narrow peak. Since the resulting absorbed doses (or air kermas) considered are small, the OSL counts per reading are lower than the RL counts per reading. Hence, counting statistics predict that for an exposure of 40 mAs, the uncertainty is going to be higher for the OSL signal than for the RL signal. This is the reverse of what we usually observe in

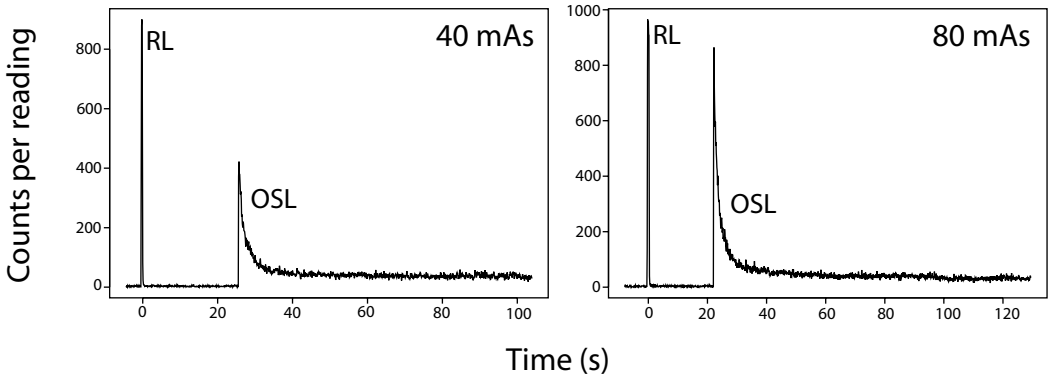

Figure 6.2: Typical RL and OSL signals in mammography for 40mAs (a) and 80 mAs (b).

radiotherapy. As seen previously, because the RL signal is collected during irradiation, it is potentially subject to some stem effect. However, in mammography conditions, the signal generated in the light guide is insignificant compared to the signal coming from the crystal ($< 1\%$) as seen on figure 6.3.

Independent absorbed dose estimates were obtained by integrating either the complete RL signal or OSL signal. For both signals (RL and OSL), some background correction is performed, and the raw signal from each probe is corrected to account for sensitivity differences. Because of the relatively small

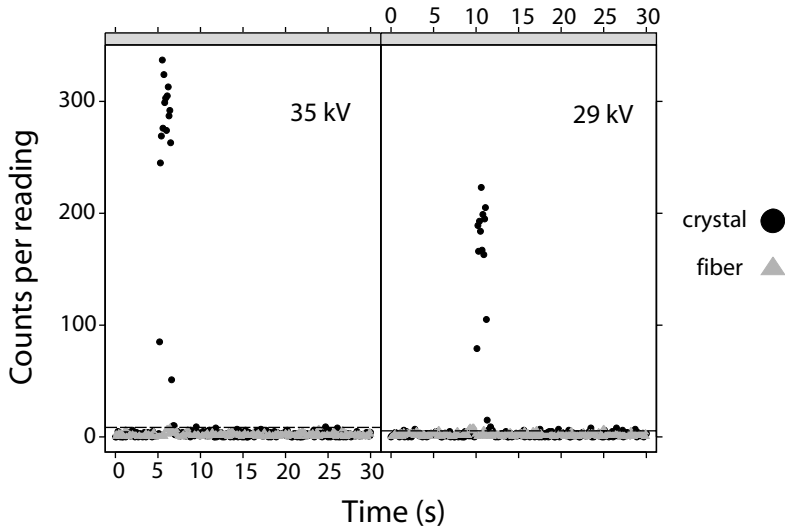

Figure 6.3: Stem effect in mammography conditions. Black symbols represent the RL signal, and grey symbols show the signal coming from the light guide.

absorbed doses in mammography conditions, it is possible to integrate the entire OSL signal in about 100s. As mentioned previously, the RL signal is subject to sensitivity changes with accumulated absorbed dose. As a consequence, for an irradiation at a constant dose rate, the RL signal is going to increase. In the case of mammography however, the resulting doses are too small for any significant changes in RL sensitivity to occur (about 0.2% for an absorbed dose of 10 mGy). Figure 6.4 illustrates this point.

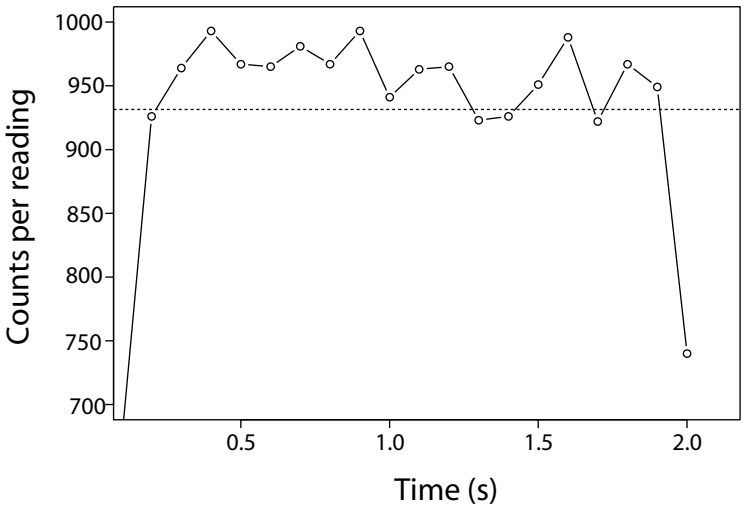

Figure 6.4: RL sensitivity changes. Even for a long (250 mAs) exposure, the increase in RL signal is not noticeable.

6.2.2 Reproducibility and linearity

To test the reproducibility and the linearity of the response of the RL/OSL dosimeter in mammography conditions, the RL/OSL fibers and the ionization chamber were positioned right underneath the compression plate of the mammography unit. No extra build-up or backscatter material was used. Thirteen exposures were made at 29 kV and 40 mAs. RL and OSL data were evaluated for both fibers, and normalized to ionization chamber readings. The results are presented in table 6.1 for an air kerma of 4.5 mGy and indicate a reproducibility of the order of 3%. The reproducibility of the signals is also illustrated in figures 6.5(a) and 6.5(b). The uncertainty on the RL data is dominated by counting statistics, while additional factors seem to increase the uncertainty on the OSL results: these may include some instability in the laser power, for example. The dose-response of the RL/OSL system was also investigated at 29 kV, and figure 6.6 shows that the output

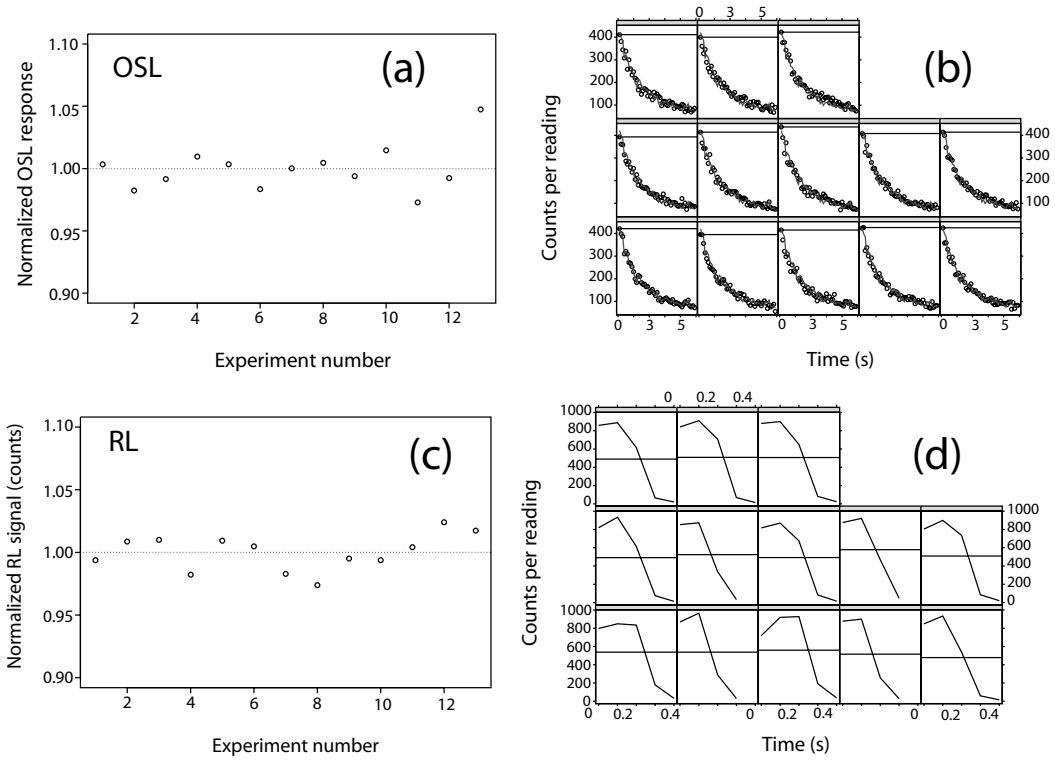

Figure 6.5: Reproducibility of the RL and OSL signals for an air kerma of 4.5 mGy for 13 measurements. (a): integrated OSL signal, (b) first 7 seconds of the OSL signal , (c) integrated RL signal and (d) visualization of the total RL signal.

Table 6.1: Reproducibility of the RL/OSL system (expressed as 1SD of 13 measurements at 29 kV for an air kerma of 4.5 mGy)

Signal	RL (counts/pC)	OSL (counts/pC)
Fiber 48	1.9%	2.5%
Fiber 49	2.5%	2.8%

is linear with dose between 40 and 250 mAs (4.5-30 mGy). The minimum detectable dose, calculated as 3 times the standard deviation of the background is below 50 μGy for both fibers when using the RL signal, and approximately 200 μGy when using the OSL signal.

6.2.3 Energy dependence

Because of the low photon energies used in mammography, the photoelectric effect is the predominant form of interaction. As a result, the energy dependence of Al_2O_3:C is expected to be considerable. The variation in RL and

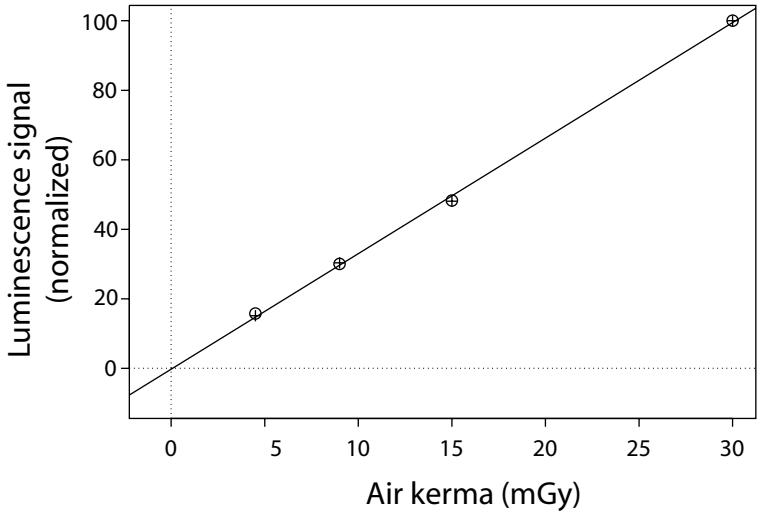

Figure 6.6: Linearity of dose-response for several exposures at 29 kV (R-squared>0.999). Data are normalized to their value at a 250 mAs exposure, corresponding to an air kerma of 30 mGy. RL signal (crosses), OSL signal (circles).

OSL response of Al_2O_3:C as a function of tube potential was investigated using the same experimental set-up as described in section 6.2.2, keeping the tube loading constant at 40 mAs during all measurements. The RL and OSL data were normalized to the simultaneous reading of the ionization chamber (the energy dependence of this ionization chamber was checked at a primary standards laboratory and is of the order of 1% for the range of energies used in the study).

Figure 6.7 shows the obtained results as a function of HVL. The response of the Al_2O_3:C crystal was found to increase by 18% when the tube potential increased from 23 kV to 35 kV, corresponding to HVL 0.296 - 0.412 mm Al.

6.3 Quantities of clinical interest

6.3.1 Backscatter factors

Like TLDs, RL/OSL probes will measure ESD, and backscatter factors will need to be established to convert ESD to ESAK. Backscatter factors for the RL/OSL probes were defined as:

$$\mathrm{BSF} = \frac{S_{phantom}}{S_{air}} \tag{6.1}$$

where $S_{phantom}$ is the signal at a point on the surface of the PMMA phantom and S_{air} is the signal free in air at the same point without the

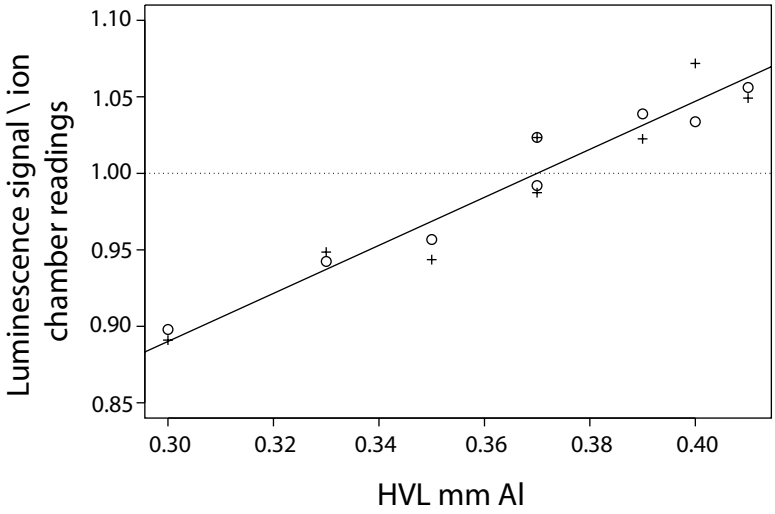

Figure 6.7: Energy dependence of the RL/OSL signals. The data are divided by the ionization chamber readings, and normalized to read unity at 29 kV. RL: crosses, OSL: circles.

phantom. The phantoms used ranged from 1 to 6 cm in thickness. The tube potential was kept at 29 kV, but the tube loading was increased as the phantom thickness increased. The results are presented in table 6.2. The data in table 6.2 suggest that full backscatter is achieved with 1 cm of PMMA. Also, the average backscatter factor is 1.066 ± 0.004 (n=12) for the pooled RL and OSL data (ignoring the differences in uncertainties and assuming that the measurements are independent) where the indicated uncertainty (expressed as 1SD) only includes the observed random variation from measurement to measurement. The observed backscatter factor is slightly lower than the value of 1.084 quoted for TLDs (with PMMA or breast tissue as the scattering material) (Zoetelief et al., 1996). This discrepancy may reflect differences in geometry (Chan and Doi, 1981) or in energy response of the different materials.

6.3.2 Influence of phantom thickness

The sensitivity of the RL/OSL probes is sufficient to measure exit doses (of the order of 0.5 mGy) in typical exposures. In the following experiment, the thickness of the PMMA phantom was varied between 2 and 6 cm, while the tube potential ranged from 23 to 35 kV. Fiber 49 was positioned at the entrance surface of the phantom, while fiber 48 was placed on the exit surface. The ratio "exit RL signal/entrance RL signal" was calculated in each case with correction for the difference in sensitivity of the two probes. As illustrated

Table 6.2: Measurements of backscatter factors (BSF) from a PMMA phantom. Three exposures were performed in each set-up.

Thickness of PMMA (cm)	Tube loading (mAs)	RL BSF	OSL BSF
1	40	1.071	1.084
2	80	1.067	1.046
3	140	1.058	1.047
4	200	1.060	1.065
4.5	200	1.057	1.081
6	200	1.075	1.083
Mean ± 1SD (n=6)		1.064 ± 0.003	1.068 ± 0.008

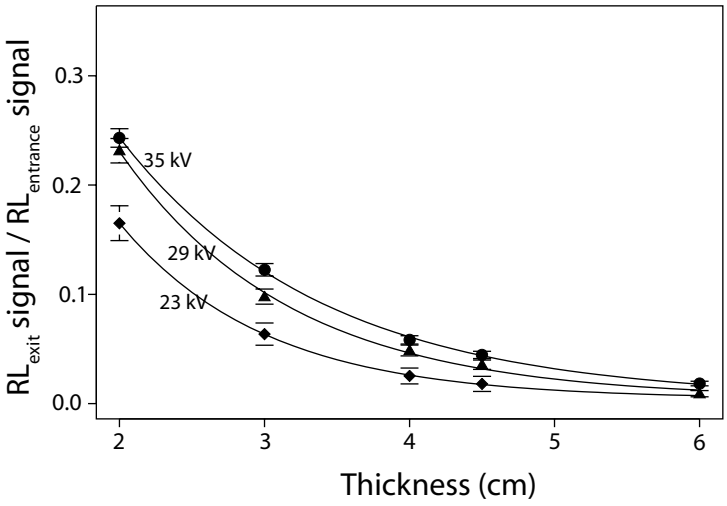

Figure 6.8: Measurements with one probe (fiber 49) at the entrance surface, the other (fiber 48) at the exit surface of a PMMA phantom. The ratios of $RL_{exit}/RL_{entrance}$ are presented for 23 kV (diamonds), 29 kV (triangles) and 35 kV (circles).

in figure 6.8, the exit/entrance RL signal ratio decreases with increasing phantom thickness, and with decreasing tube potential. Uncertainty bars were determined by counting statistics. Only in the most extreme case (6 cm PMMA and 23 kV) was the sensitivity of the exit probe too low to provide a reliable RL signal. The OSL data provide similar results, but with considerably higher uncertainties for low dose points.

6.4 *In vivo* measurements

Before any *in vivo* measurements were performed, images of the probes positioned on several PMMA phantoms were acquired to test whether their presence will degrade the diagnostic quality of the mammograms. Three experienced radiologists evaluated those images, and gave their approval for the use of the probes during patient examination. *In vivo* measurements were scheduled on three women coming to an ordinary screening examination (selected to have different breast sizes and densities). Fiber 49 was attached to the compression paddle in such a way that it was positioned between the compression paddle and the upper part of the breast during the examination. Fiber 48 was positioned on the table of the mammography unit, and was then in contact with the inferior surface of the breast (see figure 6.1). The fibers were positioned so that they would not be superimposed on the mammograms. Cranio-caudal (CC) and medio-lateral oblique (MLO) projections were used. Lead markers were attached to the compression paddle on its upper side in order to get a more precise estimate of the compressed breast thickness for each patient image. Except for these preparations, the standard procedure for mammography screening was followed, including the use of a tube potential of 29 kV, which is used routinely. Each patient received four exposures (two for each breast). RL data were acquired for each individual exposure. However, OSL readings were only performed after each patient's examination was completed. Hence, for each patient, four RL measurements and one OSL measurement (representing the sum of four exposures) were acquired. This protocol was chosen in order to avoid delays due to the longer OSL reading procedure.

Finally, the radiologists evaluated the images from all three examinations to assess the interference of the probes with the diagnostic quality of the image. One radiologist also evaluated the screening images in order to quantify the glandularity of the breast parenchyma.

HVL, ESAK and AGD were evaluated according to the European protocol on dosimetry in mammography (Zoetelief et al., 1996). ESD was evaluated from ESAK using a backscatter factor of 1.084 corresponding to a measured HVL of 0.369 mm Al for the anode/filter combination Mo/Mo and the tube potential of 29 kV. The fibers were positioned in such a way that their shadows did not superimpose on the mammograms. Three radiologists viewed the images and stated that neither the fiber dosimeters nor the lead markers disturbed the reading of the mammograms due to their small sizes and characteristic shapes that could not be confused with structures in the breast, either benign or malignant (see figure 6.9). Single calcifications could have

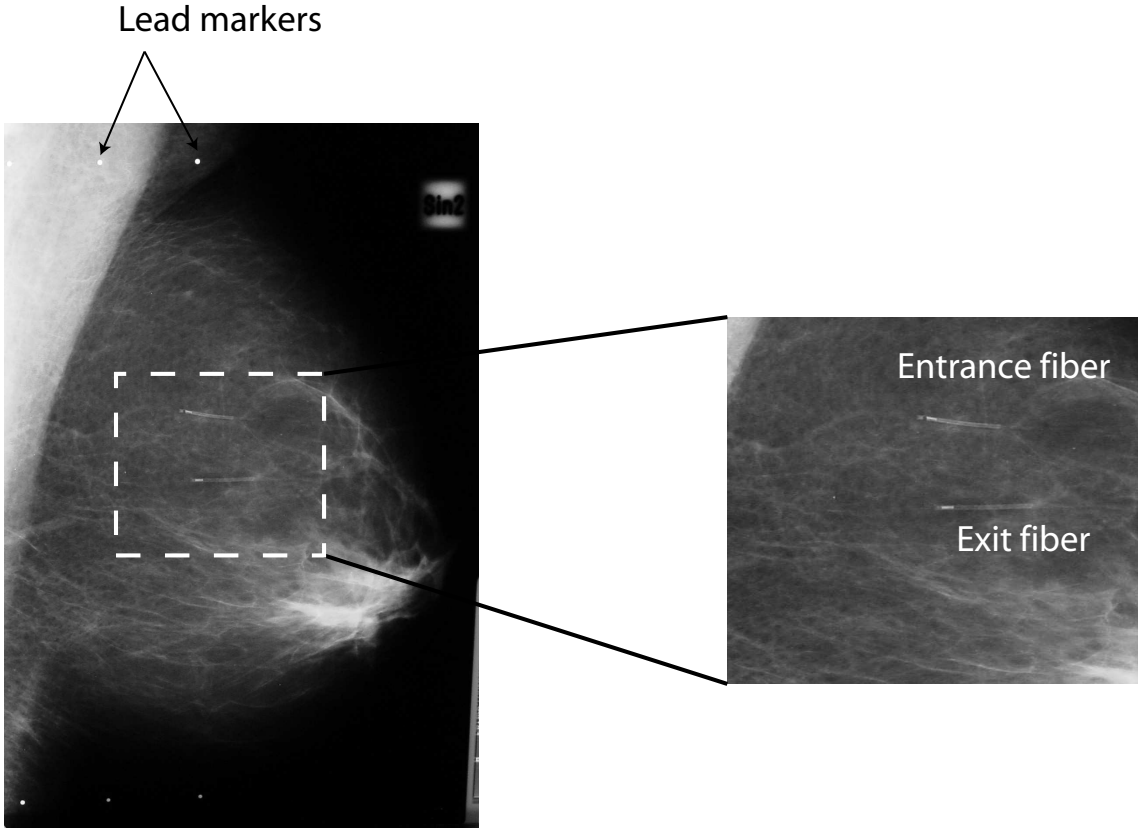

Figure 6.9: Impact of the RL/OSL fibers on a mammogram.

been obscured, but this was not considered to impair significantly on early breast cancer detection.

The estimated compressed breast thickness, ESAK and AGD are presented in table 6.3 together with estimated glandularity and breast parenchymal category, which was found to be the same for each breast of the same woman. Table 6.4 summarizes the results from RL/OSL measurements, compared with the calculated ESD from the ionization chamber measurements. RL and OSL results are expressed as counts, corrected for the different sensitivities of the two probes. For measurements at a fixed kV (here, 29 kV), the sum of the entrance RL signal seems to be a reliable estimator of the entrance surface dose, as the ratio "$RL_{entrance}$/ESD" has a standard deviation of 3%. The exit doses could also be measured *in vivo* during all twelve exposures, as seen from the "RL_{exit}" signal (this signal was at least 4 times higher than the background signal in all cases: one example is presented in figure 6.4). The ratio of exit to entrance doses can be obtained for each individual image

via RL analysis, or for each patient via OSL analysis. These estimates agree within ± 10%.

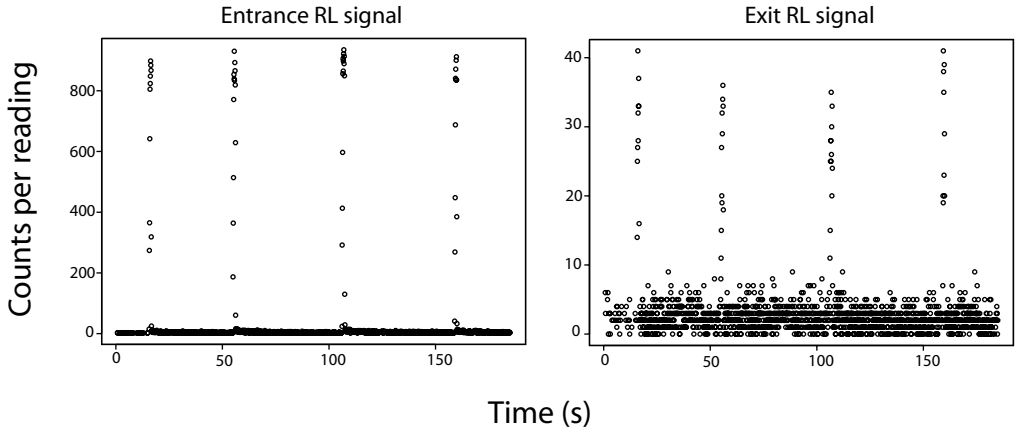

Figure 6.10: RL entrance and exit signals for one patient measurement.

6.4.1 Conclusion from the *in vivo* experiments

The RL/OSL dosimeter is capable of measuring real-time entrance as well as exit absorbed doses and dose rates in mammography. The accuracy of the system is satisfactory for *in vivo* mammography. *In vivo* entrance and exit dose measurements of three women coming to a mammography screening examination showed that the technique can be used for estimation of the ESD and that the disturbances from the dosimeters on the image are acceptable.

After analyzing the experimental work some questions arose related to the design of the probes and how it would influence the response of the RL/OSL dosimetry system, especially in mammography beams. Energy dependence could theoretically be minimized by using smaller crystals and varying the thickness of the light protective material surrounding the crystal. These issues have been investigated with Monte Carlo simulations using both calculated and experimentally determined x-ray spectra in the mammography energy range.

6.5 Probe design and energy dependence: a Monte Carlo study

After analyzing the experimental work some questions arose related to the design of the probes and how it would influence the response of the RL/OSL

Table 6.3: Patient image data and entrance surface air kerma (ESAK) and average glandular dose (AGD) values determined from the ionization chamber measurements. CC: cranio-caudal view; MLO: mediolateral oblique view.

Patient -image number	Category (0-3)	Glandularity (%)	Breast	Project.	Thickness indicator (mm)	Compressed breast thickness (mm)	Tube loading (mAs)	ESAK (mGy)	AGD (mGy)
1-1	3	85	left	CC	50	55.9	93.0	11.1	1.94
1-2			right	CC	44	52.3	72.1	8.5	1.59
1-3			left	MLO	53	56.8	83.5	10.0	1.71
1-4			right	MLO	54	60.5	80.8	9.8	1.56
2-1	2	75	left	CC	28	34.8	29.4	3.2	0.91
2-2			right	CC	26	33.0	28.9	3.1	0.93
2-3			left	MLO	26	34.2	27.5	3.0	0.86
2-4			right	MLO	25	34.2	29.1	3.1	0.91
3-1	1	25	left	CC	65	72.5	99.5	12.6	1.65
3-2			right	CC	66	76.4	126	16.1	2.00
3-3			left	MLO	68	78.5	133	17.2	2.06
3-4			right	MLO	62	70.7	102	12.8	1.72

Table 6.4: Entrance surface dose (ESD) determined for each breast image from the ionization chamber measurements and RL/OSL *in vivo* data. RL and OSL counts have been corrected for sensitivity differences between fiber 48 and fiber 49.

Patient -image number	ESD (mGy)	RL entrance (counts)	RL exit (counts)	OSL entrance (counts)	OSL exit (counts)	RL entrance / ESD per image (counts/mGy)	OSL entrance / ESD per pat. (counts/mGy)	RL exit/ entrance	OSL exit/ entrance
1-1	12	10532	281	10683	281	487	1143	0.027	0.026
1-2	9.2	8084	207			489		0.026	
1-3	10.8	9779	266			503		0.027	
1-4	10.6	9354	173			491		0.018	
2-1	3.5	2945	187	3353	239	473	1090	0.063	0.071
2-2	3.4	2952	205			486		0.069	
2-3	3.2	2955	181			510		0.061	
2-4	3.4	3155	209			514		0.066	
3-1	13.6	12107	286	15875	322	494	1099	0.024	0.020
3-2	17.5	15410	283			489		0.018	
3-3	18.6	17037	307			509		0.018	
3-4	13.9	12571	271			504		0.022	

dosimetry system, especially in mammography beams. Energy dependence could theoretically be minimized by using smaller crystals and varying the thickness of the light protective material surrounding the crystal. These issues have been investigated with Monte Carlo simulations using both calculated and experimentally determined x-ray spectra in the mammography energy range (Aznar et al., 2005b).

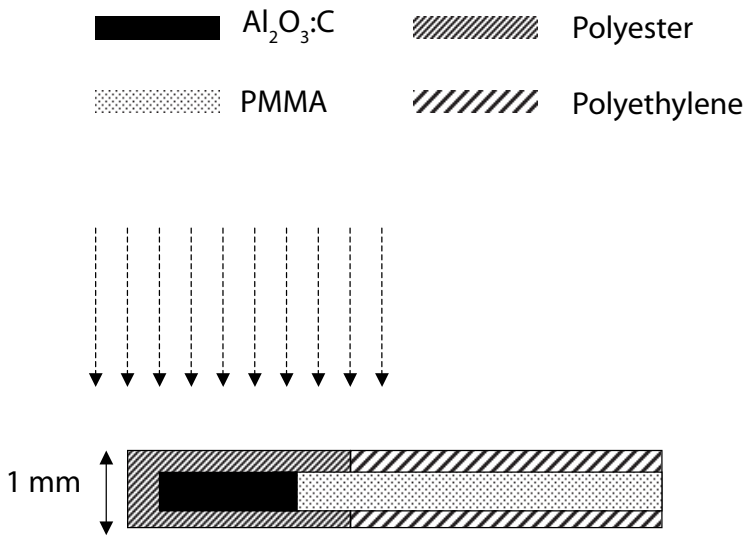

Figure 6.11: Geometry of an RL/OSL probe used in EGSnrc simulations.

Monte Carlo simulations were performed with the code EGSnrc (Kawrakov and Rogers, 2000). The user code DOSRZnrc was used to calculate the absorbed dose to the Al_2O_3:C crystal per unit photon fluence. The material data files for EGSnrc were prepared with the pre-processor PEGS4 using updated XCOM cross sections (Berger et al., 1999), (Hobeila and Seuntjens, 2002). The parameters were chosen in order to offer accurate simulations of particle transport at low energies. The photon and electron cut-off energies were both set to 1 keV, and Rayleigh scattering, spin effects, bound Compton scattering, and Bremsstrahlung production were turned on. The calculations were performed with 10^9 histories, which yielded a standard uncertainty of 0.1% when simulating the Al_2O_3:C crystal and 0.3-0.8% when the kerma in the equivalent volumes of air, free in air was calculated.

The exact composition of the Araldite coating of the crystals was not available, so Araldite was assimilated to a type of polyester (called "mylar") in the Monte Carlo simulations. In order to study the energy dependence of the detector signal as a function of detector size and thickness of light-protective material, Monte Carlo simulations were performed for three different detector

diameters (0.30, 0.48 (actual size), and 0.80 mm). These calculations were performed with an Al_2O_3:C crystal without any polyester coating. The effect from varying the polyester coating was studied for three different thicknesses (0, 0.24 (actual thickness), and 0.76 mm). The simulated geometry is shown in figure 6.11 and it may be noted that no backscatter material was used in the Monte Carlo simulations, which is due to the inherent demands on cylindrical symmetry in the code DOSRZnrc. The experimental results are the ones discussed in section 6.2.3 were obtained with only the breast support at a distance of 45 mm behind the detector. It has been assumed that this geometry generated an insignificant amount of scattered radiation to the detector, particularly since the breast support was equipped with a grid but no screen-film cassette.

6.5.1 Spectral data

Two different types of spectral data were used in the Monte Carlo simulations; i) Calculated data obtained from the "Catalogue of diagnostic x-ray spectra and other data" published by the Institute of Physics and Engineering in Medicine (IPEM, 1997), and ii) Measured spectral data, previously obtained at Sahlgrenska University Hospital in Göteborg using a Compton scattering spectrometer (Spectro-X, RTI Electronics) and a mammography unit of the same type as the one used for the RL/OSL measurements (Siemens Mammomat 3000).

Measured spectral data and RL/OSL measurements were all obtained with the Mo/Mo anode/filter combination. Using the IPEM computer program, two spectra were processed for 25 kV and 31 kV with a molybdenum target, an anode angle of 10 degrees. The following attenuating materials were included: 0.03 mm of molybdenum, 1 mm of beryllium, 500 mm of air and 1.93 mm of PMMA corresponding to the thickness of the breast compression plate used during the RL/OSL measurements. The half value layer (HVL) of the resulting beam, as obtained with the IPEM program, was 0.30 mm of Al for 25 kV (mean energy 16.0 keV), and 0.36 mm of Al for 31 kV (mean energy 17.0 keV). Measured spectral data were directly available for 25 kV. However, to be able to match the spectrum at the higher tube voltage used in the RL/OSL measurements, 31 kV was obtained via interpolation between 30 kV and 32 kV. The error introduced by this procedure is expected to be insignificant considering the observed shapes of the spectra obtained for the two surrounding tube voltages. The mean energy for the measured 25 kV and 31 kV spectra were 16.1 keV and 17.1 keV, respectively. The HVL, related to the measured spectral data, was obtained without the compression plate (Thilander Klang, 1997). For 25 kV, a value of 0.284 mm Al was

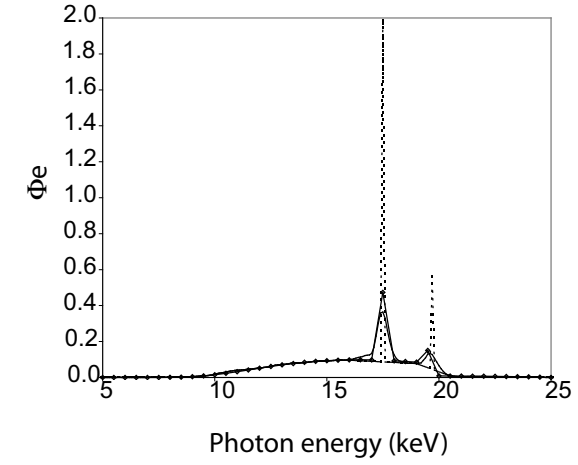

(a) spectra

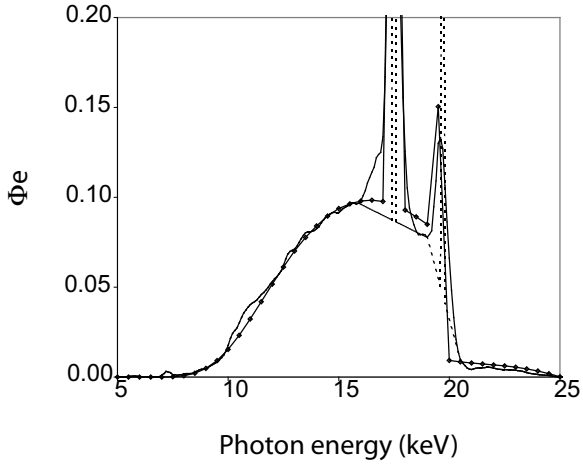

(b) spectra detail

Figure 6.12: Spectra used in EGSnrc. The energy fluence normalized to the area under the distribution, Φe, is plotted versus photon energy. Solid line with symbols: IPEM data, solid line: measured data, dotted line: modified measured data.

obtained. Data were not available for 31 kV, but interpolation between 28 kV and 32 kV yields 0.344 mm Al for this tube potential. For comparison, modified spectral data were also included in the study. These spectra have a more narrow energy distribution around the peak values, and are further described in a previous published work (Dance et al., 2000b). The HVL values corresponding to the modified spectra were, 0.288 mm Al and 0.355 mm Al, respectively. The three different spectral distributions are compared for 25 kV in figure 6.12(a), where all results have been normalized to the area under each distribution. It may be noted that the measured data were obtained

with a finer energy resolution than the data obtained from IPEM (0.1 keV vs. 0.5 keV).

6.5.2 Results

The absorbed dose to the Al_2O_3:C crystal (Dc) and the air kerma at the corresponding position free in air (Kair) free in air was calculated with EGSnrc for the two beam qualities described above, using the dimensions of the real detector system (see figure 6.11). The obtained ratio Dc/Kair was compared with the experiments from section 6.2.3. The Monte Carlo determined increase in response from 25 kV to 31 kV was found to be 5.6% using the IPEM calculated spectra, and 7.3% using both the unmodified and the modified measured spectra (combined uncertainty of the Monte Carlo calculated data = 1%, 1SD). The result obtained can be compared with the experimental value of 9% . The reproducibility of the RL/OSL being 2-3% (1SD), the calculated and experimental values of the energy dependence agree within the combined standard uncertainties of the two methods.

The diameter of the Al_2O_3:C crystal was varied between 0.30 mm and 0.80 mm, keeping the length constant at 2 mm. These calculations were performed with a "naked" crystal, i.e. without any polyester coating. The results are presented in table 6.5 for the three types of spectral data used. The standard uncertainty of the Monte Carlo calculated ratio of between the absorbed dose to the crystal and the air kerma free in air in an equivalent volume (Dc/Kair) ranged between 0.5% for the largest crystal and 1.0% for the smallest.

The coating of light-protective material surrounding the crystal was varied between 0 and 0.76 mm, keeping the diameter of the crystal and its length at constant values (0.24 mm and 2 mm, respectively). The obtained results are given in table 6.6. The standard uncertainty of the Monte Carlo calculated ratio between the absorbed dose to the crystal and the air kerma free in air in an equivalent volume (Dc/Kair) was 0.7%.

6.5.3 Discussion

The energy dependence determined from Monte Carlo simulations with EGSnrc (5.6% with the IPEM calculated spectra, 7.3% with the unmodified and modified spectra) agrees with the previously determined experimental result (9%) considering the uncertainties in calculated and measured values. The combined standard uncertainty of the Monte Carlo calculated results were 1.0% (1 SD) in all three cases. The standard uncertainty of the experimental value is estimated to be around 4% based on the reproducibility of the RL/OSL

Table 6.5: Ratios of Monte Carlo calculated values of absorbed dose crystal and air kerma for three various diameters (ø). Two beam qualities and three different spectral distributions were included in the comparison. The thickness of light-protective material around the crystal was set to 0 mm. The standard uncertainty of calculated ratios was 0.3% for the largest crystal, 0.5% for the middle-sized crystal and 0.8% for the smallest. *meas* refers to the measured spectra and *modif* to the modified measured spectra. *Incr* represents the percentage increase in Dc/Dair from exposure in a 25kV beam to exposure in a 31 kV beam.

Tube kV	Dc/Dair 0.30 mm ø			Dc/Dair 0.48 mm ø			Dc/Dair 0.80 mm ø		
spectra	IPEM	meas	modif	IPEM	meas	modif	IPEM	meas	modif
25 kV	2.74	2.79	2.78	2.41	2.41	2.40	1.96	1.97	1.97
31 kV	2.83	2.87	2.87	2.53	2.57	2.56	2.13	2.17	2.17
Incr. (%)	3.3	2.9	3.2	5.0	6.6	6.7	8.7	10.2	10.2

Table 6.6: Ratios of Monte Carlo calculated values of absorbed dose to the crystal and air kerma free in air for three various thicknesses of the light protective material surrounding the crystal. Two beam qualities and three different spectral distributions were included in the comparison. The diameter of the crystal was set to 0.48 mm. The standard uncertainty of calculated ratios was 0.5%. *meas* refers to the measured spectra and *modif* to the modified measured spectra. *Incr* represents the percentage increase in Dc/Dair from exposure in a 25kV beam to exposure in a 31 kV beam.

Tube kV	Dc-Dair 0 mm			Dc-Dair 0.24 mm			Dc-Dair 0.76 mm		
spectra	IPEM	meas	modif	IPEM	meas	modif	IPEM	meas	modif
25 kV	2.41	2.41	2.40	2.33	2.33	2.32	2.18	2.18	2.17
31 kV	2.53	2.57	2.56	2.46	2.50	2.49	2.33	2.37	2.37
Incr. (%)	5.0	6.6	6.7	5.6	7.3	7.3	6.9	8.7	9.2

system and the uncertainty in air kerma determined with the ionization chamber. The obtained results encourage the concept of using EGSnrc and the adopted simulated geometry for further studies of the present detector system in mammography. The results of the Monte Carlo simulations indicate that a minor improvement of the energy dependence could be achieved by reducing the thickness of the light-protective material from the thickness used at present (0.24 mm). However, some thickness will always be required due to the need for light protection of the crystal, and the potential improvement is less than 1% according to the obtained results. A larger reduction of the energy dependence at photon beam qualities used in mammography could

be achieved by reducing the size of the crystal. The effect when reducing the diameter from 0.48 mm to 0.30 mm was 3% on average for the three spectra used. the observed differences when using the different spectra are within the uncertainties of the Monte Carlo results. However, it must be considered that a reduction in size is followed by a decrease in sensitivity and a reasonable compromise has to be found. The small differences in tables 6.5 and 6.6 between the results obtained using IPEM and measured data, respectively, are caused by both small differences the three spectra, including differences in the energy resolution (see figure 6.12(a)). The latter gives a slight effect on the Monte Carlo sampling procedure. However, considering the uncertainty of the Monte Carlo calculated results, 0.1% for Dc and 0.4-1.0% for Kair (detector size 0.80 to 0.30 mm), the observed differences are insignificant.

6.6 Conclusion

The experiments presented in this chapter show the considerable potential of the RL/OSL dosimetry system in mammography. Because of their small size, the RL/OSL probes can be positioned on the breast during the mammography examination without interfering with the diagnostic outcome. RL/OSL signals can be used to obtain a reliable estimate of the entrance surface dose to the breast. The high sensitivity of the RL/OSL probes enable to measure absorbed doses on the exit (inferior) surface of the breast.Exit dose information would help radiologists to determine whether some women are exposed to higher doses as a result of mammography examinations because of the nature of their breasts (size, density, etc.). The main concern of using Al_2O_3:C in mammography is the energy dependence of the material, and Monte Carlo calculations show that this parameter can be minimized by reducing slightly the size of the crystal. In conclusion, RL/OSL optical fiber dosimetry is a very promising technique for *in vivo* measurements in mammography.

7 Conclusion

This thesis summarizes the application of a combined radioluminescence (RL) and optically stimulated luminescence (OSL) dosimetry system developed at Risø National Laboratory in the period 2001-2005 in close collaboration with Malmö University Hospital and Copenhagen University Hospital. This research has particularly focused on the application of this system as an *in vivo* dosimeter in radiation therapy and in mammography. The results presented in this work show the considerable potential of RL/OSL optical-fiber dosimetry using carbon-doped aluminum oxide (Al_2O_3:C) as a detector.

One of the main advantages of the Al_2O_3:C RL/OSL dosimetry system compared to existing dosimeters is the availability of two relatively independent signals: the radioluminescence signal, obtained in real-time during the irradiation, and the optically stimulated luminescence signal, acquired after the treatment or radiographic examination. The RL signal is subject to two phenomena, namely the "sensitization" of the detector and the "stem effect" from the optical fiber. Both phenomena and their implications have been discussed in detail in this thesis. Because of the difficulties involved in analyzing the RL signal to obtain a reliable absorbed dose estimate, the OSL signal was given primary focus in the early stages of this project. Later on, however, some special attention was paid to the RL signal and resulted in the development of two methods to correct the RL response. One, based on dose-reference curve, corrected for the sensitization phenomenon and enables real-time assessment of the dose rate delivered to the Al_2O_3:C crystal. The other approach is a temporal gating method, which discriminates between the true RL signal from the Al_2O_3:C crystal and the signal generated in the connecting optical fiber. These two analytic tools have shown to be invaluable as they permit reliable dose rate and absorbed dose estimates in real-time through the RL signal. The advantages in radiation therapy include a field-by-field dose estimate in IMRT measurements. Other potential applications of the RL signal would be in brachytherapy, where the accumulated dose and instantaneous dose rate could be used as monitoring tools.

The precision and accuracy of the RL/OSL dosimetry system make it particularly attractive for *in vivo* dosimetry in radiation therapy. Three IMRT patient measurements have been performed, which suggest that OSL estimates can predict the absorbed dose delivered to the target volume within 2%. Phantom measurements show the same potential for the RL system, and indicate that accuracy can be improved by carefully selecting the RL/OSL fiber. Several sources of variability have been identified. Some of them suggest that reliable dose assessments must be obtained according to a specific protocol (e.g., it is recommended to let the system warm up). Other sources of variability will necessitate further investigation, and possibly some minor mechanical modifications of the dosimetry system (e.g., optical coupling between the fiber and the reader).

It should be noted, however, that an acceptance of the RL/OSL dosimetry system as a clinical tool in *in vivo* radiation therapy dosimetry depends on more than its overall accuracy. As was already mentioned in the introduction of this thesis, dosimetry systems must be affordable, as well as easy to calibrate and use. Many dosimetry systems (MOSFETs, diamonds) are used only marginally today as they can not easily compete with the existing systems (diodes and TLDs) in terms of costs and time investment. The RL/OSL dosimetry system, if commercialized, will necessitate a primary investment from a clinical institution to acquire the optical and electronic equipment. However, the Al_2O_3:C fibers will be relatively cheap, making the overall system financially competitive in the long run. In fact, the cost of Al_2O_3:C is so low that the RL/OSL fibers may be designed as a disposable component of the system, thereby eliminating any concern about sterilization. As far as user-friendliness and calibration are concerned, the RL/OSL dosimetry system would benefit from additional work to compete with silicon diodes. Mainly, the laser bleaching time should be reduced and the stability of the system should be improved so that monthly calibrations are sufficient. Though this will take additional work, there are no fundamental obstacles to such improvements.

As far as *in vivo* dosimetry in mammography is concerned, the advantages of the RL/OSL dosimetry system over existing systems are clear: the high-sensitivity and fast readings of the RL/OSL system, as well as the unobtrusive appearance of the detectors on the mammogram, make it a very attractive alternative to TLDs. Additional information in the form of exit doses could also provide a new light on radiation protection issues in mammography.

Other interesting applications of the RL/OSL system in diagnostic radiology and radiation medicine are foreseen include fluoroscopic examinations, dosimetry during special CT-scanning procedures or *in vivo* dosimetry in nuclear medicine (for imaging and treatment purposes).

Bibliography

Akselrod, M., Kortov, V., Kravetsky, D., and Gotlib, V. (1990). Highly sensitive thermoluminescent anion-defect alpha Al_2O_3:C single crystal detectors. *Radiation Protection Dosimetry*, 33:119–122.

Akselrod, M., Larsen, N., Whitley, V., and McKeever, S. (1998). Thermal quenching of F-center luminescence in Al_2O_3:C. *Applied Physics*, 84:3364–73.

Alecu, R. and Alecu, M. (1999). In vivo rectal dose measurements with diodes to avoid misadministrations during intracavitary high dose brachytherapy for carcinoma of the cervix. *Medical Physics*, 26(5):768–770.

Andersen, C., Aznar, M., Bøtter-Jensen, L., Back, S., Mattsson, S., and Medin, J. (2003a). Development of optical fibre luminescent techniques for real-time *in vivo* dosimetry in radiotherapy. *Standards and code of practice in medical radiation dosimetry*, 2:353–360.

Andersen, C., Bøtter-Jensen, L., and Murray, A. (2003b). A mini x-ray generator as an alternative to a 90sr/90y beta source in luminescence dating. *Radiation Measurements*, 37(4-5):557–561.

Andersen, C., Marckmann, C., Aznar, M., Bøtter-Jensen, L., Kjær-Kristoffersen, F., and Medin, J. (2005). An algorithm for real-time in vivo dose-rate measurements using the radioluminescence signal from Al_2O_3:C. *Radiation Protection Dosimetry, In Press.*

Aznar, M., Andersen, C., Bøtter-Jensen, L., Back, S., Mattsson, S., Kjaer-Kristoffersen, F., and J, M. (2004). Real-time optical-fibre luminescence dosimetry for radiotherapy. *Physics in Medicine and Biology*, 49:1655–1669.

Aznar, M., Hemdal, B., Medin, J., Marckmann, C., Andersen, C., Bøtter-Jensen, L., Andersson, I., and Mattsson, S. (2005a). In vivo absorbed

dose measurements in mammography using a new real-time luminescence technique. *British Journal of Radiology*, 78:328–334.

Aznar, M., Medin, J., Hemdal, B., Thilander-Klang, A., Bøtter-Jensen, L., and Mattsson, S. (2005b). A Monte Carlo study of the energy dependence of Al_2O_3:C crystals for real-time in vivo dosimetry in mammography. *Radiation Protection Dosimetry, In Press.*

Aznar, M., Nathan, R., Murray, A., and Bøtter-Jensen, L. (2003). Determination of differential dose rates in a mixed beta and gamma field using shielded Al_2O_3:C: results of Monte Carlo modelling. *Radiation Measurements*, 37(4-5):329–334.

Beddar, A., Law, S., Suchowerska, N., and Mackie, T. (2003). Plastic scintillation dosimetry: optimization of light collection efficiency. *Physics in Medicine and Biology*, 48:1141–1152.

Beddar, A., Mackie, T., and Attix, F. (1992a). Cerenkov light generated in optical fibres and other light pipes irradiated by electron beams. *Physics in Medicine and Biology*, 37:925–935.

Beddar, A., Mackie, T., and Attix, F. (1992b). Water-equivalent plastic scintillation detectors for high energy beam dosimetry: I physical characteristics and theoretical considerations. *Physics in Medicine and Biology*, 37:1883–1900.

Beddar, A., Mackie, T., and Attix, F. (1992c). Water-equivalent plastic scintillation detectors for high energy beam dosimetry: II properties and measurements. *Physics in Medicine and Biology*, 37:1901–1913.

Beddar, A., Suchowerska, N., and Law, S. (2004). Plastic scintillation dosimetry for radiation therapy: minimizing capture of Cerenkov radiation noise. *Physics in Medicine and Biology*, 49:783–790.

BEIR, V. (1991). Health effects of exposure to low levels of ionizing radiation. Technical report, National Research Council, National Academy Press, Washington DC.

Berger, M., Hubbell, J., Seltzer, S., Coursey, J., and Zucker, D. (1999). XCOM: photon cross section database (version 1.2). Technical report, National Institute of Standards and Technology, Gaithesburg MD.

Berni, D., Gori, C., Lazzari, B., Mazzochi, S., Rossi, F., and Zatelli, G. (2002). Use of TLD in evaluating diagnostic reference levels for some

radiological examinations. *Radiation Protection Dosimetry*, 101(1-4):411–413.

Bjork, P., Knoos, T., and Nilsson, P. (2000). Comparative dosimetry of diode and diamond detectors in electron beams for intraoperative radiation therapy. *Medical Physics*, 27(11):2580–2588.

Bøtter-Jensen, L. (1995). Retrospective radiation dose reconstruction using optically stimulated luminescence on natural materials. *International Workshop on scientific bases for decision making after a radioactive contamination of an urban environment (IAEA TECDOC, Rio de Janeiro and Goiania, Brazil.*

Bøtter-Jensen, L., Agersnap Larsen, N., Markey, B., and McKeever, S. (1997). Al_2O_3:C as a sensitive OSL dosemeter for rapid assessment of environmental photon count rates. *Radiation Measurements*, 27:295–298.

Bucciolini, M., Buonamici, F., Mazzochi, S., De Angelis, C., Onori, S., and Cirrone, G. (2003). Diamond detector versus silicon diode and ion chamber in photon beams of different energy and field size. *Medical Physics*, 30(8):2149–2154.

Buckley, L., Kawrakow, I., and Rogers, D. (2004a). CSnrc: correlated sampling Monte Carlo calculations using EGSnrc. *Medical Physics*, 31(12):3425–3435.

Buckley, L., Rogers, D., Aznar, M., and J, M. (2004b). Monte Carlo calculated dose to Al_2O_3 per unit dose to water in photon beams compared to osl response per unit dose to water. presented at the AAPM annual meeting, Pittsburgh PA, July 2004.

Burlin, T. (1966). A general cavity theory of ionisation. *British Journal of Radiology*, 39:727–734.

Burlin, T. and Chan, F. (1969). The effect of the wall on the Fricke dosimeter. *Int. J. Appl. Radiat. Isot.*, 20:767–775.

Butson, M., Rozenfeld, A., Mathur, J., Carolan, M., Wong, T., and Metcalfe, P. (1996). A new radiotherapy surface dose detector: the MOSFET. *Medical Physics*, 23(5):655–658.

Butson, M., Yu, P., Cheung, T., and Metcalfe, P. (2003). Radiochromic film for medical radiation dosimetry. *Material Science and Engineering*, 41:61–120.

Chan, H. and Doi, K. (1981). Monte Carlo simulation studies of backscatter factors in mammography. *Radiology*, 139:195–199.

Cheung, T., Butson, M., and Yu, P. (2004). Effects of temperature variation on MOSFET dosimetry. *Physics in Medicine and Biology*, 49:N191–N196.

Chuang, C., Verhey, L., and Xia, P. (2002). Investigation of the use of MOSFET for clinical IMRT dosimetric verification. *Medical Physics*, 29(6):1109–1115.

Ciocca, M., Orecchia, R., Garibaldi, C., Rondi, E., Luini, A., Gatti, G., Intra, M., Veronesi, P., Lazzari, R., Tosi, G., and Veronesi, U. (2003). In vivo dosimetry using radiochromic films during intraoperative electron beam radiation therapy in early-stage breast cancer. *Radiotherapy and Oncology*, 69:285–289.

Clift, M., Sutton, R., and Webbs, D. (2000). Dealing with Cerenkov radiation generated in organic scintillator dosimeters by Bremsstrahlung beams. *Physics in Medicine and Biology*, 45:1165–1182.

Dance, D. (1990). Monte Carlo calculation of conversion factors for the estimation of mean glandular breast dose. *Physics in Medicine and Biology*, 35:1211–1219.

Dance, D., Skinner, C., Young, K., Beckett, J., and Kotre, C. (2000a). Additional factors for the estimation of mean glandular breast dose using the UK mammography dosimetry protocol. *Physics in Medicine and Biology*, 45:3225–3240.

Dance, D., Thilander Klang, A., Sandborg, M., Skinner, C., Castellano Smith, I., and Alm Carlsson, G. (2000b). Influence of anode/filter material and tube potential on contrast, signal-to-noise ratio and average absorbed dose in mammography: a Monte Carlo study. *British Journal of Radiology*, 73:1056–1067.

de Boer, S., Beddar, A., and Rawlinson, J. (1993). Optical filtering and spectral measurements of radiation-induced light in plastic scintillation dosimetry. *Physics in Medicine and Biology*, 38:945–958.

Dong, S., Chu, T., Lee, J., Lan, G., Wu, T., Yeh, Y., and Hwang, J. (2002). Estimation of mean glandular dose from monitoring breast entrance skin kerma using a high sensitivity metal oxide semiconductor field effect transistor (MOSFET) dosimeter system in mammography. *Applied Radiation and Isotopes*, 57:791–799.

Dutreix, A. (1984). When and how can we improve precision in radiotherapy? *Radiotherapy and Oncology*, 2:275–292.

Erfurt, G. and Krbetschek, M. (2002). A radioluminescence study of spectral and dose characteristics of common luminophors. *Radiation Protection Dosimetry*, 100(1-4):403–406.

Erfurt, G., Krbetschek, M., Trautman, T., and Stolz, W. (2000). Radioluminescence (RL) behaviour of Al_2O_3:C - potential for dosimetric applications. *Radiation Measurements*, 32:735–739.

Essers, M. and Mijnheer, B. (1999). In vivo dosimetry during external photon beam radiotherapy. *Int J Radiat Oncol Biol Phys*, 43(2):245–259.

Feldman, A., Edwards, F., and Hendee, W. (2001). Point/counterpoint: the routine use of personal patient dosimeters is of little use in detecting therapeutic misadministrations. *Medical Physics*, 28(3):295–297.

Fiorino, C., Corletto, D., Mangili, P., Broggi, S., Bonin, A., Cattaneo, G., Parisi, R., Rosso, A., Signorotto, P., Villa, E., and Calandrino, R. (2000). Quality assurance by systematic in vivo dosimetry: results on a large cohort of patients. *Radiotherapy and Oncology*, 56:85–95.

Gaza, R., McKeever, S., Akselrod, M., Akselrod, A., Underwood, T., Yoder, C., Andersen, C., Aznar, M., Marckmann, C., and Bøtter-Jensen, L. (2004). A fiber-dosimetry method based on OSL from Al_2O_3:C for radiotherapy applications. *Radiation Measurements*, 38(4-6):809–812.

Haraldsson, P., Knoos, T., Nystrom, H., and Engstrom, P. (2003). Monte Carlo study of TLD measurements in air cavities. *Physics in Medicine and Biology*, 48:N253–N259.

Heukelom, S., Lanson, J., and Mijnheer, B. (1991). Comparison of entrance and exit measurements using ionization chambers and silicon diodes. *Physics in Medicine and Biology*, 36:47–59.

Heydarian, M., Hoban, P., Beckham, W., Borchardt, I., and Beddoe, A. (1993). Evaluation of a PTW diamond detector for electron beam measurements. *Physics in Medicine and Biology*, 38:1035–1042.

Heydarian, M., Hoban, P., and Beddoe, A. (1996). A comparison of dosimetry techniques in stereotactic radiosurgery. *Physics in Medicine and Biology*, 41:93–110.

Higgins, P., Alaei, P., Gerbi, B., and Dusenbery, K. (2003). In vivo diode dosimetry for routine quality assurance in IMRT. *Medical Physics*, 30(12):3118–3123.

Hoban, P., Heydarian, M., Beckham, W., and Beddoe, A. (1994). Dose rate dependence of a PTW diamond detector in the dosimetry of a 6 MV photon beam. *Physics in Medicine and Biology*, 39(1219-1229).

Hobeila, F. and Seuntjens, J. (2002). Implementation of NIST X-COM-based photoelectric cross-sections in EGSnrc. *Medical Physics*, 29:1353.

Huntley, D., Godfrey-Smith, D., and Thewalt, M. (1985). Optical dating of sediments. *Nature*, 313:105–107.

Huston, A., Justus, A., Falkenstein, P., Miller, R., Ning, H., and Altemus, R. (2002). Optically stimulated luminescent glass optical fiber dosemeter. *Radiation Protection Dosimetry*, 101(1-4):23–6.

Huston, A., Justus, B., Falkenstein, P., Miller, R., Ning, H., and Altemus, R. (2001). Remote optical fiber dosimetry. *Nucl Instrum Methods B*, 184:55–67.

IAEA (2001). Investigation of an accidental exposure of radiotherapy patients in Panama, report of a team of experts. IAEA report, International Atomic Energy Agency. 26 May - 1 June 2001.

ICRP (2000). Prevention of accidents to patients undergoing radiotherapy (icrp publication 86). Ann of ICRP 30 (3), 1-70.

ICRU (1976). Determination of absorbed dose in a patient irradiated by beams of x or gamma rays in radiotherapy procedures. ICRU report 24, Bethesda, maryland.

ICRU (1998). Fundamental quantities and units for ionizing radiation. ICRU report 86, Bethesda, maryland.

IPEM (1997). *Catalogue of diagnostic x-ray spectra and other data*. The institute of physics and engineering in medicine (IPEM), York, UK, report no 78 edition.

Janssens, A., Eggermont, G., Jacobs, R., and Thielens, G. (1974). Spectrum perturbation and energy deposition models for stopping power ratio calculations in general cavity theory. *Physics in Medicine and Biology*, 19:619–630.

Jeraj, R., Keall, P., and Siebers, J. (2002). The effect of dose calculation accuracy on inverse treatment planning. *Physics in Medicine and Biology*, 47:391–407.

Johns, H. and Cunningham, J. (1983). *The Physics of Radiology*. Charles C Thomas, Springfield, Illinois, USA, fourth edition.

Jordan, K. (1996). Evaluation of ruby as a fluorescent sensor for optical fiber-based radiation dosimetry. *Proceedings of Fluorescence Detection IV*, SPIE 2705:170–178.

Jornet, N., Carrasco, P., Jurado, D., Ruiz, A., Eudaldo, T., and Ribas, M. (2004). Comparison study of MOSFET detectors and diodes for entrance in vivo dosimetry in 18 MV x-ray beams. *Medical Physics*, 31(9):2534–2542.

Jornet, N., Ribas, M., and Eudaldo, T. (2000). In vivo dosimetry: Intercomparison between p-type based and n-type based diodes for the 16-25 MV energy range. *Medical Physics*, 27(6):1287–1293.

Jursinic, P. (2001). Implementation of an in vivo diode dosimetry program and changes in diode characteristics over a 4-year clinical history. *Medical Physics*, 28(8):1718–1726.

Justus, B., Falkenstein, P., Huston, A., Plazas, M., Ning, H., and Miller, R. (2004). Gated fiber-optic-coupled detector for in vivo real-time radiation dosimetry. *Applied Optics*, 43(8):1663–8.

Kalef-Ezra, J., Boziari, A., Litsas, J., Tsekeris, P., and Koligliatis, T. (2002). Thermoluminescence dosimetry for quality assurance in radiation therapy. *Radiation Protection Dosimetry*, 101(1-4):403–405.

Kawrakov, I. and Rogers, D. (2000). The EGSnrc code system: Monte Carlo simulation of electron and photon transport. Technical report PIRS-701, National Research Council of Canada, Ottawa, Canada.

Khan, F. (1992). *The physics of radiation therapy*. Williams and Wilkins, Baltimore, Maryland, USA, second edition edition.

Kim, S., Akpati, H., Kielbasa, J., Li, J., Liu, C., Amdur, R., and Palta, J. (2004). Evaluation of intrafraction patient movement for cns and head and neck imrt. *Medical Physics*, 31(3):500–506.

Knoos, T., Ahnesjo, A., Nilsson, P., and Weber, L. (1995). Limitations of a pencil beam algorithm approach to photon dose calculations in lung tissue. *Physics in Medicine and Biology*, 40:1411–1420.

Kron, T., Rosenfeld, A., Lerch, M., and Bazley, S. (2002). Measurements in radiotherapy beams using on-line MOSFET detectors. *Radiation Protection Dosimetry*, 101(1-4):445–448.

Laub, W., Kaulich, T., and F, N. (1999). A diamond detector in the dosimetry of high energy electron and photon beams. *Physics in Medicine and Biology*, 44:2183–2192.

Laub, W. and Wong, T. (2003). The volume effect of detectors in the dosimetry of small fields used in IMRT. *Medical Physics*, 30(3):341–347.

Loncol, T., Greffe, J., Vynckier, S., and Scalliet, P. (1996). Entrance and exit dose measurements with semicondutors and thermoluminescent dosemeters: a comparison of methods and in vivo results. *Radiotherapy and Oncology*, 41:179–187.

Marckmann, C., Aznar, M., Andersen, C., and Bøtter-Jensen, L. (2005). Influence of the stem effect on radioluminescence signals from optical fiber Al_2O_3:C dosemeters. *Radiation Protection Dosimetry, In Press.*

Marre, D. and Marinello, G. (2004). Comparison of p-type commercial electron diodes for in vivo dosimetry. *Medical Physics*, 31(1):50–56.

McKeever, S., Akselrod, M., and Markey, B. (1996). Pulsed optically stimulated luminescence dosimetry using alpha-Al_2O_3:C. *Radiation Protection Dosimetry*, 65:267–272.

Meiler, R. and Podgorsak, M. (1997). Characterization of the response of commercial diode detectors used for in vivo dosimetry. *Medical Dosimetry*, 22(1):31–37.

Mijnheer, B., Battermann, J., and Wambersie, A. (1987). What degree of accuracy is required and can be achieved in photon and neutrom therapy. *Radiotherapy and Oncology*, 8:237–252.

Miljanic, S. and Ranogajec-Komor, M. (1996). Application of cavity theory to the response of various TLDs to Co60 gammas degraded in water. *Physics in Medicine and Biology*, 42:1335–1349.

Mobit, P. (1996). *Monte Carlo and experimental studies of dose measurements in radiotherapy beams with LiF-TLDs and other solid state dosimeters*. PhD thesis, University of London, Physics Department, Institute of Cancer Research, Sutton, UK.

NACP (1980). Nordic association of clinical physics: Procedures in external radiation therapy dosimetry with electron and photon beams with maximum energy between 1 and 50 mev. *Acta Radiol Oncol*, 19:55–79.

Nam, T., Keddy, R., and Burns, R. (1987). Synthetic diamonds as in vivo detectors. *Medical Physics*, 14(4):596–601.

Noel, A., Aletti, P., and Malissard, L. (1995). Detection of errors in individual patients in radiotherapy by systematic in vivo dosimetry. *Radiotherapy and Oncology*, 34:144–151.

Paliwal, B. and Almond, P. (1976). Electron attenuation characteristics of LiF. *Health Physics*, 31:151–153.

Peet, D. and Pryor, M. (1999). Evaluation of a MOSFET radiation sensor for the measurement of entrance surface dose in diagnostic radiology. *British Journal of Radiology*, 72:562–568.

Polf, J., McKeever, S., Akselrod, M., and Holmstrom, S. (2002). A real-time, fibre optic dosimetry system using Al_2O_3 fibres. *Radiation Protection Dosimetry*, 100:301–304.

Ramani, R., Russel, S., and O'Brien, P. (1997). Clinical dosimetry using MOSFETs. *Int. J. Radiat. Oncol. Biol. Phys.*, 37:954–964.

Ramasehan, R., Kohli, K., Zhang, T., Lam, T., Norlinger, B., Hallil, A., and Islam, M. (2004). Performance characteristics of a microMOSFET as an in vivo dosimeter in radiation therapy. *Physics in Medicine and Biology*, 49:4031–4048.

Rikner, G. and Grusell, E. (1987). Patient dose measurements in photon fields by means of silicon semiconductor detectors. *Medical Physics*, 14(5):870–873.

Rosenfeld, A. (2002). MOSFET dosimetry on modern radiation oncology modalities. *Radiation Protection Dosimetry*, 101(1-4):393–398.

Rowbottom, C. and Jaffray, D. (2004). Characteristics and performance of a micro-MOSFET: an imageable dosimeter for image-guided radiotherapy. *Medical Physics*, 31(3):609–615.

Roy, O., Magne, S., Gaucher, J., Albert, L., Dusseau, L., Bessiere, J., and Ferdinand, P. (1997). All optical fiber sensor based on optically stimulated luminescence for radiation detection. *12th International Conference on Optical Fiber Sensors*.

Saini, A. and Zhu, T. (2004). Dose rate and SSD dependence of commercially available diode detectors. *Medical Physics*, 31(4):914–924.

Scalchi, P. and Francescon, P. (1998). Calibration of a MOSFET detection system for 6-mv in vivo dosimetry. *Int J Radiat Oncol Biol Phys*, 40(4):987–993.

Soubra, M., Cygler, J., and Mackay, G. (1994). Evaluation of a dual bias MOSFET detector as a radiation dosimeter. *Medical Physics*, 21:567–572.

SSI (2002). Regulations and general advice on diagnostic standard doses and reference levels within medical x-ray diagnostics. Technical Report SSI FS-2002:2, Swedish Radiation Protection Authority, Stockholm. in Swedish.

TG40 (1994). Comprehensive QA for radiation oncology: report of AAPM radiation therapy committee task group 40. *Medical Physics*, 21:581–618.

TG58 (2001). Clinical use of electronic portal imaging: report of AAPM radiation therapy committee task group 58. *Medical Physics*, 5:712–737.

TG69 (2005). Radiographic film for megavoltage beam dosimetry. Report of the American Association of Physicists in Medicine (AAPM), Task Group 69: IN PROGRESS.

Thilander Klang, A. (1997). *Diagnostic quality and absorbed dose in mammography: influence of x-ray spectra and breast anatomy.* PhD thesis, University of Goteborg. ISBN 91-628-2499-6.

Van Dam, J. and Marinello, G. (1994). Methods for in vivo dosimetry in external radiotherapy. Technical report, European society for therapeutic radiology and oncology (ESTRO).

Van Esch, A., Bohsung, J., Sorvari, P., Tenhunen, M., Paiusco, M., Iori, M., Engström, P., Nyström, H., and Huyskens, D. (2002). Acceptance and quality control (qc) procedures for the clinical implementation of intensity modulated radiotherapy (imrt) using inverse planning and the sliding window technique: experience from five radiotherapy departments. *Radiotherapy and Oncology*, 65(1):53–70.

Wilkins, D., Li, X., Cygler, J., and L, G. (1997). The effect of dose rate dependence of p-type silicon detectors on linac relative dosimetry. *Medical Physics*, 24(6):879–881.

Yukihara, E., Whitley, V., Polf, J., Klein, D., McKeever, S., Akselrod, A., and Akselrod, M. (2003). The effects of deep trap population on the thermoluminescence of Al_2O_3:C. *Radiation Measurements*, 37:627–638.

Zoetelief, J., Fitzgerald, M., Leitz, W., and Säbel, M. (1996). *European protocol on dosimetry in mammography.* EUR 16263.

Risø's research is aimed at solving concrete problems in the society.

Research targets are set through continuous dialogue with business, the political system and researchers.

The effects of our research are sustainable energy supply and new technology for the health sector.